REPORT DOCUMENTATION PAGE

Form Approved OMB NO. 0704-0188

1. REPORT DATE (DD-MM-YYYY)	2. REPORT TYPE	3. DATES COVERED (From - To)
01-05-2009	Final Report	1-Oct-2004 - 30-Nov-2008

4. TITLE AND SUBTITLE
DARPA Helicopter Quieting Program W911NF0410424
University of Maryland, College Park & Stanford University

5a. CONTRACT NUMBER
W911NF-04-1-0424

5b. GRANT NUMBER

5c. PROGRAM ELEMENT NUMBER
7G10T1

6. AUTHORS
James Baeder, Shreyas Ananthan, Jaina Sitaraman, Gianluca Iaccarino, Seonghyeon Hahn, Gaurav Gopalan, Fredric H. Schmitz, Cal Sargent

5d. PROJECT NUMBER

5e. TASK NUMBER

5f. WORK UNIT NUMBER

7. PERFORMING ORGANIZATION NAMES AND ADDRESSES
University of Maryland - College Park
Office of Research Administration & Advancement
University of Maryland, College Park
College Park, MD 20742 -5141

8. PERFORMING ORGANIZATION REPORT NUMBER

9. SPONSORING/MONITORING AGENCY NAME(S) AND ADDRESS(ES)
U.S. Army Research Office
P.O. Box 12211
Research Triangle Park, NC 27709-2211

10. SPONSOR/MONITOR'S ACRONYM(S)
ARO

11. SPONSOR/MONITOR'S REPORT NUMBER(S)
43538-EG-DRP.1

12. DISTRIBUTION AVAILIBILITY STATEMENT
Approved for public release; Distribution Unlimited

13. SUPPLEMENTARY NOTES
The views, opinions and/or findings contained in this report are those of the author(s) and should not contrued as an official Department of the Army position, policy or decision, unless so designated by other documentation.

14. ABSTRACT
A computational framework for coupled aeroelastic analysis of helicopter rotors was developed, tested and successfully validated as part of the HUSH program. The Python-based framework allows the combination of solvers of different disciplines for analysis of different rotorcraft problems in both serial and parallel computing environments. In addition, the framework standardized code interfaces such that multiple codes which have similar functionality can be substituted with ease thereby increasing the spectrum of veri?cation and validation.

15. SUBJECT TERMS
Helicopter Quieting HUSH CFD QSAM-PRIME

16. SECURITY CLASSIFICATION OF:			17. LIMITATION OF ABSTRACT	15. NUMBER OF PAGES	19a. NAME OF RESPONSIBLE PERSON
a. REPORT	b. ABSTRACT	c. THIS PAGE			James Baeder
U	U	U	SAR		19b. TELEPHONE NUMBER 301-405-1107

Report Title

DARPA Helicopter Quieting Program W911NF0410424
University of Maryland, College Park & Stanford University

ABSTRACT

A computational framework for coupled aeroelastic analysis of helicopter rotors was developed, tested and successfully validated as part of the HUSH program. The Python-based framework allows the combination of solvers of different disciplines for analysis of different rotorcraft problems in both serial and parallel computing environments. In addition, the framework standardized code interfaces such that multiple codes which have similar functionality can be substituted with ease thereby increasing the spectrum of veri?cation and validation. The HUSH framework was successfully applied and evaluated for rotorcraft systems that encompass articulated, bearingless and hingless hub con?gurations. The results obtained from the computations show good agreement with measurements (?ight test data as well as controlled experiments) where available. The predictions also showed improved accuracy over the existing comprehensive analysis technology that relied on lifting line based aerodynamics. The studies demonstrate maturity of the CFD codes and the capability of the coupled ?uid-structure simulations to accurately predict the airloads, structural bending moments, the overall performance and acoustics under a wide range of ?ight conditions. Overall, the CFD/CSD coupled framework is consistently shown to improve the state-of-the-art in simulations of rotorcraft aeromechanics.

List of papers submitted or published that acknowledge ARO support during this reporting period. List the papers, including journal references, in the following categories:

(a) Papers published in peer-reviewed journals (N/A for none)

Number of Papers published in peer-reviewed journals: 0.00

(b) Papers published in non-peer-reviewed journals or in conference proceedings (N/A for none)

Number of Papers published in non peer-reviewed journals: 0.00

(c) Presentations

S. Nagarajan and S. Lele, "Sound Generation by Unsteady Airfoil Motions: A Study Using Direct Computation and Acoustic Analogy," 11th AIAA/CEAS Aeroacoustics Conference, AIAA Paper 2005-2915, Monterey, CA, May 2005.

Ananthan, S. and Baeder, J., “Prediction and Validation of Loads on Bearingless Rotors Using a Coupled CFD- CSD Methodology,” 64th Annual Forum and Technology Display of the American Helicopter Society International, Montreal, Cananda, April 29–May 1 2008.

Ananthan, S., Baeder, J., Sitaraman, J., Hahn, S., and Iaccarino, G., "Hybrid Unsteady Simulation of Helicopters", 26th AIAA Applied Aerodynamics Conference, Honolulu, Hawaii, Aug. 18-21, 2008, AIAA-2008-7339.

Number of Presentations: 3.00

Non Peer-Reviewed Conference Proceeding publications (other than abstracts):

Number of Non Peer-Reviewed Conference Proceeding publications (other than abstracts): 0

Peer-Reviewed Conference Proceeding publications (other than abstracts):

Number of Peer-Reviewed Conference Proceeding publications (other than abstracts): 0

(d) Manuscripts

Number of Manuscripts: 0.00

Number of Inventions:

Graduate Students

NAME	PERCENT_SUPPORTED
Eric Shroeder	0.20
Vinod Lakshminarayan	0.50
Asitav Mishra	0.20
Ayan Sengupta	0.20
Steve Repsher	0.20
Mohammad Shoeybi	0.20
QiQi Wang	0.20
Seongim Choi	0.20
Ayodeji Ojofeitimi	0.20
Laura McInnis	0.20
Seongwon Kang	0.20
FTE Equivalent:	**2.50**
Total Number:	**11**

Names of Post Doctorates

NAME	PERCENT_SUPPORTED
Anubhav Datta	0.50
Karthik Duraisamy	0.50
Gaurav Gopalan	0.50
Jayanarayan Sitaraman	0.50
Shreyas Ananthan	0.50
Seonghyeon Hahn	1.00
Daniel Bodony	0.25
Gianluca Iaccarino	0.25
Nagarajan Santhanam	0.25
Xiaohua Wu	0.25
FTE Equivalent:	**4.50**
Total Number:	**10**

Names of Faculty Supported

NAME	PERCENT_SUPPORTED	National Academy Member
James Baeder	0.30	No
Inderjit Chopra	0.05	No
Frederic Schmitz	0.10	No
Juan Alonso	0.05	No
Sanjiva Lele	0.10	No
Charbel Farhat	0.05	No
Parviz Moin	0.05	Yes
Gianluca Iaccarino	0.10	No
FTE Equivalent:	**0.80**	
Total Number:	**8**	

Names of Under Graduate students supported

NAME	PERCENT SUPPORTED
FTE Equivalent:	
Total Number:	

Student Metrics

This section only applies to graduating undergraduates supported by this agreement in this reporting period

The number of undergraduates funded by this agreement who graduated during this period:	0.00
The number of undergraduates funded by this agreement who graduated during this period with a degree in science, mathematics, engineering, or technology fields:	0.00
The number of undergraduates funded by your agreement who graduated during this period and will continue to pursue a graduate or Ph.D. degree in science, mathematics, engineering, or technology fields:	0.00
Number of graduating undergraduates who achieved a 3.5 GPA to 4.0 (4.0 max scale):	0.00
Number of graduating undergraduates funded by a DoD funded Center of Excellence grant for Education, Research and Engineering:	0.00
The number of undergraduates funded by your agreement who graduated during this period and intend to work for the Department of Defense	0.00
The number of undergraduates funded by your agreement who graduated during this period and will receive scholarships or fellowships for further studies in science, mathematics, engineering or technology fields:	0.00

Names of Personnel receiving masters degrees

NAME	
Mohammnad Sheybi	
Daniel Berkenstock	
Total Number:	**2**

Names of personnel receiving PHDs

NAME	
Seongim Choi	
Total Number:	**1**

Names of other research staff

NAME	PERCENT SUPPORTED	
Steve Jones	0.10	No
Cindy Fulce-Paradan	0.05	No
Dan Bodony	0.10	No
Annie Jensen	0.10	No
FTE Equivalent:	**0.35**	
Total Number:	**4**	

Sub Contractors (DD882)

Inventions (DD882)

DARPA Helicopter Quieting Program W911NF0410424

University of Maryland, College Park & Stanford University

Final Report (presented as AIAA-2008-7339)

1 Introduction

Reliable prediction of the highly complex aerodynamic operating enviroment of rotorcraft is difficult even for steady forward flight conditions. The difficulty arises from the necessity of capturing a combination of physical phenomena that include transonic and compressibility effects on the advancing blade, dynamic stall on the retreating blades and the interaction of the rotor blades with the returning vortex wake. Moreover the problem is highly aeroelastic with strong fluid structure coupling and demands a true multi-physics simulation. Despite various advances in individual disciplines, confident prediction of the rotorcraft aeromechanics and acoustics still remains a significant challenge to the rotorcraft community, and hinders the development of efficient, quieter rotors.

Traditional aerodynamic models used in comprehensive rotorcraft simulations are commonly based on lifting line theory and incorporate simple empirical models to simulate the blade unsteady effects, and to account for the influence of the rotor wake. These models are strictly valid only in the flight regimes where the experimental data used to derive the empirical models were obtained. Thus, these models are severely limited in their capability to predict the wide range of aerodynamic effects encountered by the rotor blade. Designing and conducting reliable experiments for a wide range of flight conditions, especially maneuvers, is a very costly enterprise and may even be impossible. Numerical simulations provide a more cost-effective way of analyzing rotor aerodynamics. However, the development and analysis of a comprehensive rotor structural and aerodynamic model is not without its challenges. The primary challenge arises from the strong fluid-structure interaction that needs to be adequately modeled in the simulations. A full continuum dynamics treatment of the rotor structural and aerodynamic interaction is impractical.[1] A modular approach where partitioned domains interact via a common interface is preferable. This allows the individual solvers to use the most efficient, domain-specific solution technique in solving the governing equations.

Recent research has shown that a high-fidelity computational fluid dynamics (CFD) analysis is necessary to capture all the aerodynamic phenomena which are critical to the accurate prediction of the blade structural dynamics and other mechanical loads.[2, 3, 4, 2, 5] Traditionally, research in the different disciplines of rotorcraft aeromechanics has been conducted with very little interaction between the disciplines. The limitation of such a research approach is that even the most advanced models of a given discipline, e.g., comprehensive structural or flight dynamics codes, concentrate on a very limited aspect of the rotorcraft problem and use simplistic models for modeling the other aspects. In the last decade, significant achievements have been demonstrated in simulating the rotors in steady flight as a coupled aeroelastic problem using CFD and comprehensive structural dynamics (CSD) models, thus combining the strengths of the different disciplines.[6, 7]. The details of the coupling algorithm and its implementation are discussed briefly in the following subsections.

1.1 The Aeromechanic Coupling Problem

The aeroelastic coupling problem for rotor aeromechanics can be modeled using two different approaches: 1. tight coupling, and 2. loose coupling. In a tight coupling approach,[5, 8] the airloads predictions from CFD, the blade structural deformations predicted by CSD, and the rotor control settings are exchanged essentially at every timestep. In a loose coupling approach, the airloads and structural deformation data are exchanged between the two codes once every rotor revolution. Both approaches have advantages and disadvantages. The loose coupling approach is limited to steady, periodic flight conditions, while the tight coupling is more general and is necessary for simulating maneuvering flight conditions. Tight coupling, however, is computationally more intensive when compared to the loose coupling approach,[9] because several rotor revolutions may be required to obtain a converged trim solution and periodic structural dynamic response. This is especially true of soft in-plane rotors where the low damping in lag mode leads to extended periods of transients in the numerical solution. Since the focus of this study is mainly the analysis of steady, periodic flight

conditions the loose coupling strategy is adopted. The loose coupling methodology utilized in the present work follows the delta method proposed by Tung et al.[10].

Unlike their fixed wing counterparts, rotor blades operate in close proximity to the wakes shed and trailed off the blade surfaces even after several rotor revolutions, depending on the flight condition. Therefore, adequate resolution of the rotor wake structure is essential for predicting the blade loading. Capturing the wake structure using CFD requires very fine grid resolution in the regions of high vorticity to mitigate the effects of numerical dissipation. Capability of adaptive mesh refinement is critical to track vorticity and ensure adequate mesh resolutions in the appropriate regions without incurring severe computational penalty. An alternative to the wake capturing approach is the wake-coupling approach where the near-field wake is captured using CFD while the effects of the far-field wake are approximated using Lagrangian vorticity based models.[4, 2] This can significantly reduce the computational costs involved in coupled simulations with only a moderate reduction in the modeling fidelity. It is, therefore, prudent to evaluate the capabilities of the wake-coupling approaches in comparison to wake-capturing methodology and determine the domain of validity of these approximate approaches.

1.2 Challenges in Implementing a Coupled Simulation Framework

The coupling methodologies that were utilized in the past were somewhat limited in scope in expanding the areas of application. The primary complexity encountered in any multi-physics problem is the method and sequence of data exchange between the codes modeling the different disciplines. From a code development perspective it is important that the codes be independent and modular solvers which can be easily integrated with minimal effort. The advantage of such an approach is that the development and optimization of individual solvers and addition of new and updated modules to the framework can be achieved without a massive rewrite of all the participating codes. This enables the use of existing well-tested and validated codebases without building the functionality into a new monolithic code. In addition, a modular approach allows researchers to combine different existing codes for either solving new problems or evaluating different models without much development overhead. The most popular approaches explored to date in interfacing the different physics models are: 1. file I/O [5], 2. Server based with intermediate/driver codes[11, 12], and 3. Python-based approach with dynamic loading.[13, 14] In the file I/O approach the data transfer between the different models is achieved by reading and writing the data to files on the disk. This approach can incur a performance penalty depending on the amount of data that needs to be written to and read from the disks. The server based approach is quite efficient in this respect but does involve a sizeable amount of code intervention in the participating methodology. In contrast the python-based framework allows the participating solvers to reference each other's data without a significant performance overhead.

The choice of Python over compiled languages like Java, or other scripting languages, like Perl or MATLAB^{TM}, was motivated by several reasons. Python is freely available and works on almost all computational platforms used by the scientific community. Python's interpreter can be a very useful tool for debugging, prototype testing and development as well as for visualization purposes. Python has full support for object-oriented programming allowing for data encapsulation and standardization. Python has a rich set of scientific and numerical libraries (NumPy, SciPy, matplotlib) as well as a comprehensive set of general purpose libraries thereby minimizing the amount of code necessary to perform various tasks. Python bindings to C, C++ and Fortran 77/90 codes can be generated using SWIG and f2py libraries. While SWIG can generate bindings for Perl or Ruby, there is no equivalent for f2py in the other scripting languages. Libraries such as pyMPI or mympi allow python-based frameworks to be deployed in a parallel computing framework. The aforementioned capabilities make Python an ideal candidate for wrapping individual solvers in a combined computational framework and is used in the present study.

Traditional attempts at coupling domain specific solvers mostly relied on the development of a one-to-one coupling interface between the different solvers – see Fig. 1. This approach has several disadvantages: 1. introduction of new solvers will require some rewrite for all the participating solvers to introduce a coupling interface for the new solver, 2. it requires the exposure of the internal data structure of the solvers breaking data-encapsulation, 3. there is usually no standardized programming interface available that can be used to generate the driver script. Such a design is unsuitable for rapid development and testing of driver routines, as well as incorporation of new solvers.

For a framework to be truly modular, generic and extensible, it needs to provide a standardized coupling interface that the solvers can hook into – see Fig. 2. The participating solvers then only need to implement an interface to the

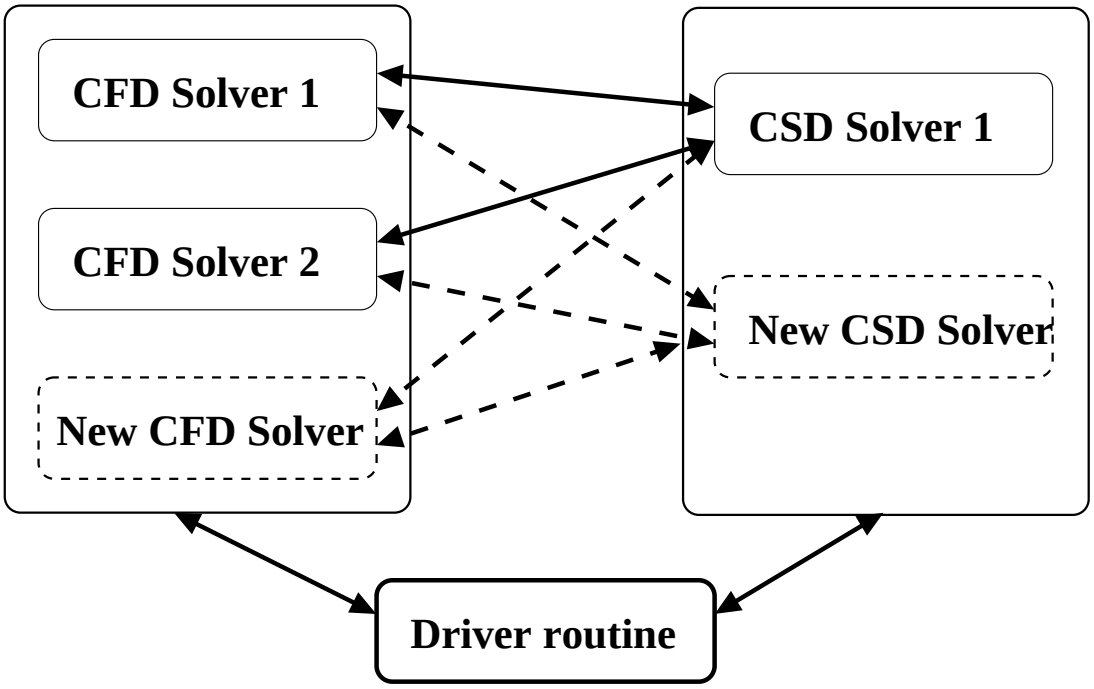

Figure 1: Traditional coupling methodology using one-to-one interfaces between domain specific solvers.

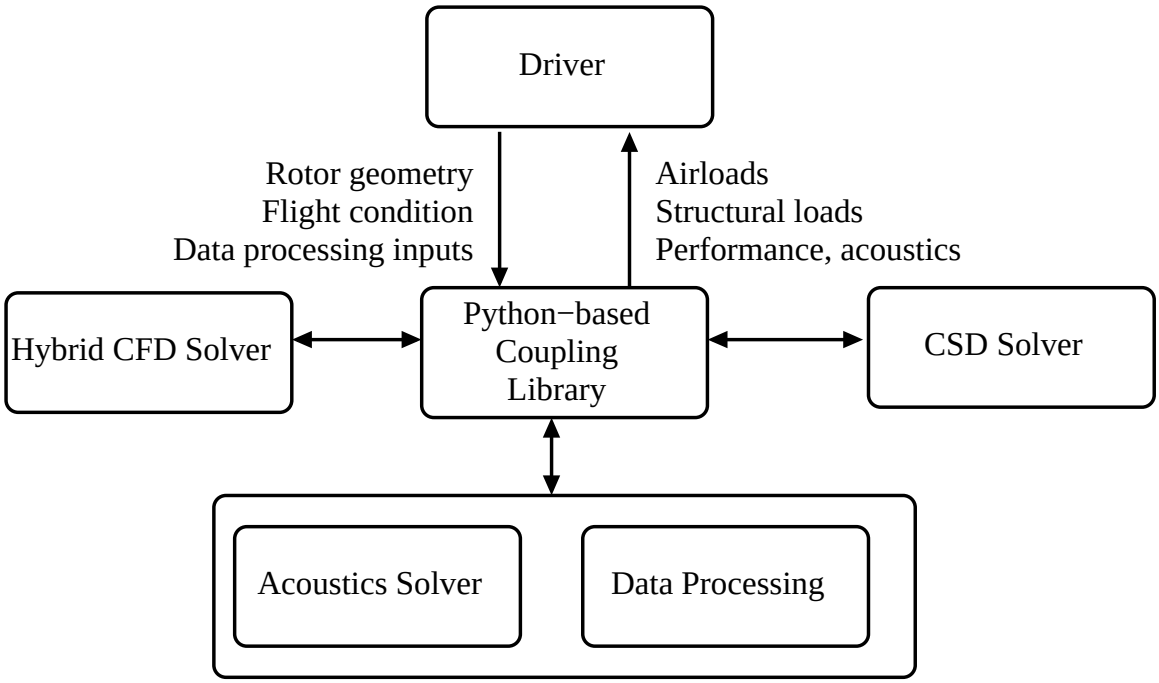

Figure 2: Schematic of the HUSH coupling framework. The central coupling library provides a standard interface for the participating solvers, the auxiliary modules, and the end-user scripts.

Table 1: Summary of the rotor configurations and flight conditions analyzed for the Helicopter Quieting Program.

Flight condition	C_T/σ	μ	Other
UH-60A rotor			
C8534	0.08	0.368	
C9017	0.1325	0.237	
C9310	0.0795	0.359	
C9121	0.0696	0.204	
C9505	0.0746	0.259	
DNW rotor			
1310	0.0872	0.3014	$\alpha_s = -4.49^\circ$
HART II rotor			
Baseline	0.0594	0.1508	$\alpha_s = 4.5^\circ$
Minimum noise	0.0601	0.1505	HHC inputs
Minimum vibration	0.0602	0.1505	HHC inputs
MDART & SMART rotor			
Baseline	0.08	0.3	$\alpha_s = -9.1^\circ$
Case 1	0.08	0.3	$\alpha_s = -9.1^\circ$, $\theta_{TEF} = 2^\circ \sin(5\psi + 90)$
Case 2	0.08	0.3	$\alpha_s = -9.1^\circ$, $\theta_{TEF} = 2^\circ \sin(3\psi + 60)$
Case 3	0.07	0.38	$\alpha_s = -9.1^\circ$, $\theta_{TEF} = 1^\circ \sin(5\psi_b + 180)$
Case 4	0.075	0.2	$\alpha_s = +1.5^\circ$, $\theta_{TEF} = 2^\circ \sin(2\psi_b + 240) + ^\circ \sin(5\psi_b + 330)$

coupling library and can automatically exchange data with other solvers already incorporated into the framework. A generic coupling interface is not restricted to coupling just CSD and CFD solvers but also opens up the possibility of the development of other helper libraries such as grid generation routines, data processing and visualization modules. This enables the developers to quickly enhance the feature-set of the framework without a rewrite of the proven, validated solver code. Another advantage of a generic coupling interface is that the end-user can generate driver scripts without have to worry about the implementation details of an individual solver as the coupling library abstracts away the finer details of the solver implementation. Thus, codes for solving different problems can be developed and tested quickly. The Hybrid Unsteady Simulation of Helicopters (HUSH) framework is such a multi-physics simulation infrastructure of rotorcraft aeromechanics that combines the advanced simulation capabilities for aerodynamics, structural dynamics, vehicle trim and aeroacoustics in an efficient and modular manner. The framework supports swapping of different physics packages with relative ease enabling a rigorous validation and verification process as well as calibration of code reliability.

The objective of the paper is to summarize the development, evaluation, and validation of the HUSH computational framework for the analysis of a variety of helicopter rotors operating in steady, periodic flight conditions, developed as part of DARPA's Helicopter Quieting Program (HQP). In addition to demonstrating the maturity of coupled simulation tools, the goals of HQP also involved rigorous validation of the computational codes under a wide range of flight conditions and rotor configurations. Airloads, structural bending moments, rotor noise and performance characteristics were all validated extensively with available experimental data. UH-60A, HART-II, DNW rotor, MDART and SMART rotor configurations were analyzed using this computation framework. The results were extensively validated with the measurements from the UH-60A Airloads Program[15], the DNW rotor test,[16, 17] the HART-II test,[18] and the MDART experiments[19, 20]. Table 1 provides a concise summary of the flight conditions and rotor configurations that were studied during the course of this program.

The University of Maryland Advanced Rotorcraft Code[21] (UMARC) and Rotor Comprehensive Analysis System (RCAS) code are used for structural dynamics modeling and vehicle trim. Two different CFD solvers University of Maryland Transonic Unsteady Reynolds-averaged Navier Stokes (UMTURNS)[22] and Stanford University multi-block (SUmb)[23] are used interchageably as near body solvers and utilized in the context of the wake-coupling approach. The Maryland Free Wake (MFW)[24] and Parallel Wake Analysis Module (PWAM)[25] are used for wake modeling in this approach. For the wake-capturing approach the near-body methodology was combined with different off-body solvers: Overset TURNS (OVERTURNS)[26] and SUmb+CDP[27]. A domain connectivity package CHIMPS[13] was utilized for performing overset grid interpolation between the near and off-body solvers. Finally the acoustic computations are performed as a postprocessing step using the ACUM code [25]. The different codes, their functionality and role in the computation framework are summarized concisely in Table 2.

Table 2: Summary of the codes available in the HUSH computational framework. Explanations of the acronyms can be found in Sec. 2.2.2— 2.2.5

Function	**Code**	**Code**
CFD near-body solver	SUmb[23]	UMTURNS[22]
CFD off-body solver	CDP[28]	OVERTURNS[26]
CSD and trim	UMARC[21]	RCAS[29]
Wake Analysis	MFW[24]	PWAM[25]
Acoustics	ACUM[25]	
Grid connectivity	CHIMPS[13]	

2 Methodology

The HUSH framework is built using independent domain-specific solvers, each dealing with a different physical aspect of the problem. The modules used in the framework can run independently of the other components, or can be run via a Python script interface to facilitate data exchange between the solvers in a coupled simulation. While the CSD and CFD solvers form the heart of the framework, there are several other modules required for pre- and post-processing of the data. For example, the grid generation utilities are part of the framework and are usually run as a pre-processing step before performing the aeroelastic coupling. Similarly, the acoustic module is used as a post-processing step where the CFD solution from the blade surfaces is processed to obtain the acoustic pressure histories at the desired locations. The framework is generic enough to incorporate additional modules with minimal modifications to the participating solvers allowing researchers to enhance the computational framework with ease.

2.1 Aeroelastic Coupling Metholodology

The coupled aeroelastic analysis adopts a *loose-coupling* of the CFD-CSD models[10, 3, 30, 7]. The approach involves the following steps:

1. Comprehensive structural analysis provides baseline blade deformations, trim control angles, and preliminary airloads (lifting line approach).
2. The blade deformations and trim control angles are used as inputs by the CFD model to predict more accurate airloads over the blades.
3. The differences between the airloads computed by CFD and the lifting line approach in CSD model are the *delta* airloads. These delta airloads are imposed as a correction to the lifting line airloads in the CSD computations during the next iteration. A new trim state is obtained which is then fed back into the CFD model to obtain a new airloads prediction.
4. The above CFD-CSD coupling iterations are performed until the *delta* loads converge at all radial and azimuthal locations on the rotor. At this point, the converged lifting line airloads within the CSD analysis is the same as the airloads predicted by the CFD model.

2.2 Structural Dynamics and Trim

The University of Maryland Advanced Rotorcraft Code (UMARC)[21] was primarily used for the structural analysis. The rotor blades are modeled as second-order nonlinear isotropic Euler-Bernoulli beams. The blades undergo coupled flap, lag, torsion and axial degrees of motion. A lifting-line model provides the aerodynamic response sensitivities to blade deformations. The sectional blade lift, drag and moment coefficients were obtained using table lookup. The Maryland Free-Wake model[24] was used to obtain the inflow at the rotor plane. A Weissinger-L nearwake model[31] is used along with Leishman-Beddoes two-dimensional unsteady aerodynamic model.[32] Both free-flight propulsive trim and wind-tunnel trim algorithms are available within the structural analysis. The blade was modeled using 20 finite elements for

all the rotor configurations shown in Table 1. In the case of the bearingless rotor, four elements were used to model the flexbeam and three were used to model the torquetube. The HUSH framework also supports another rotor aeromechanics code, the Rotor Comprehensive Analysis System (RCAS)[29] which is developed and maintained by the US Army.

2.3 CFD methodology for Wake-Coupling

As mentioned previously, two different CFD solvers, UMTURNS and SUmb, are used interchangeably within the computational framework. UMTURNS is an unsteady RANS solver that uses a second-order backward difference method using Lower-Upper Symmetric Gauss Seidel (LUSGS)[33] for time integration. Newton sub-iterations are used to remove factorization errors and recover time accuracy for unsteady computations[34]. The inviscid fluxes are computed using an upwind scheme that uses Roe's flux differencing with MUSCL type limiting. The viscous fluxes are computed using second-order central differencing. Either Baldwin-Lomax or Spalart-Allmaras[35] turbulence model is utilized for RANS closure.

Stanford University multi-block (SUmb)[23] is a multi-block, massively scalable parallel (both in CPU and memory), structured flow solver. It uses a cell-centered finite volume discretization for the viscous and inviscid fluxes. An implicit second order backwards in time discretization is used for integration in time. Convergence acceleration is accomplished by using a non-linear multi-grid which uses an m-stage Runge-Kutta as the smoother in the dual time. RANS closure is achieved using either a one, two or four equation turbulence model which are solved segregated from the mean flow and uses DD-ADI as the smoother in dual time.

In both solvers, only one rotor blade is modeled when using the wake coupling approach to minimize the computational costs. The induced velocity contributions from the far-wake trailed off from the rotor blades in the flowfield is computed at each grid point using a free wake methodology — currently HUSH supports MFW (Maryland Free-Wake model[24]) and PWAM (Parallel Wake Analysis Module[25]) — and incorporated into the solution using the field velocity approach[36]. The elastic deformations are accounted for in the flow solution by deforming the blade mesh to conform to the blade structural surface. Note that this step requires recomputation of the grid and time metrics at every physical timestep.

A body conforming C-O mesh is constructed around the rotor blades, thus ensuring a better definition of the blade tips — see Fig. 3. Typically the computational mesh uses 129 points in the wraparound direction, of which 97 points are on the blade surface, 65 points are in the normal direction, and 65 points are in the spanwise direction. The spacing of the grid points near the blade surface in the normal direction is approximately 10^{-5} chords which is required for the viscous calculations. Refined meshes with twice the resolution in spanwise and chordwise directions have also been used in some computations for sensitivity studies.

2.4 CFD methodology for Wake-Capturing

Both the wake capturing solvers employ an overset mesh strategy to capture the near-body/off-body flow features. OVERTURNS is essentially an overset version of the UMTURNS solver described above. The off-body mesh is solved using the same algorithm and discretization as the near-body solver. The domain connectivity procedure required for achieving appropriate overset grid interpolation resides internal to the code in this case.

The other alternative that HUSH supports is the use of a combination of two different codes, SUmb [23] and CDP [28] for wake-capturing. In this approach, the near-body flow is solved using SUmb, while the off-body flow is captured using (CDP) code. The CDP code (acronym for the late Charles David Pierce, one of the developers of the code) is developed at the Center for Turbulence research at the Stanford University. CDP was originally an incompressible LES code which was developed for combustor applications. The code was modified to support a RANS capability to be combatible for rotor wake simulations. Note that the LES type low diffusion algorithms for discretizing fluid fluxes are retained in the RANS approach and would provide benefits in minimizing the numerical dissipation and subsequent unphysical diffusion of vorticity in rotor wakes. CDP is also a massively parallel flow solver that uses a fully unstructured collocated grid approach to facilitate grid adaption in regions of high gradients.

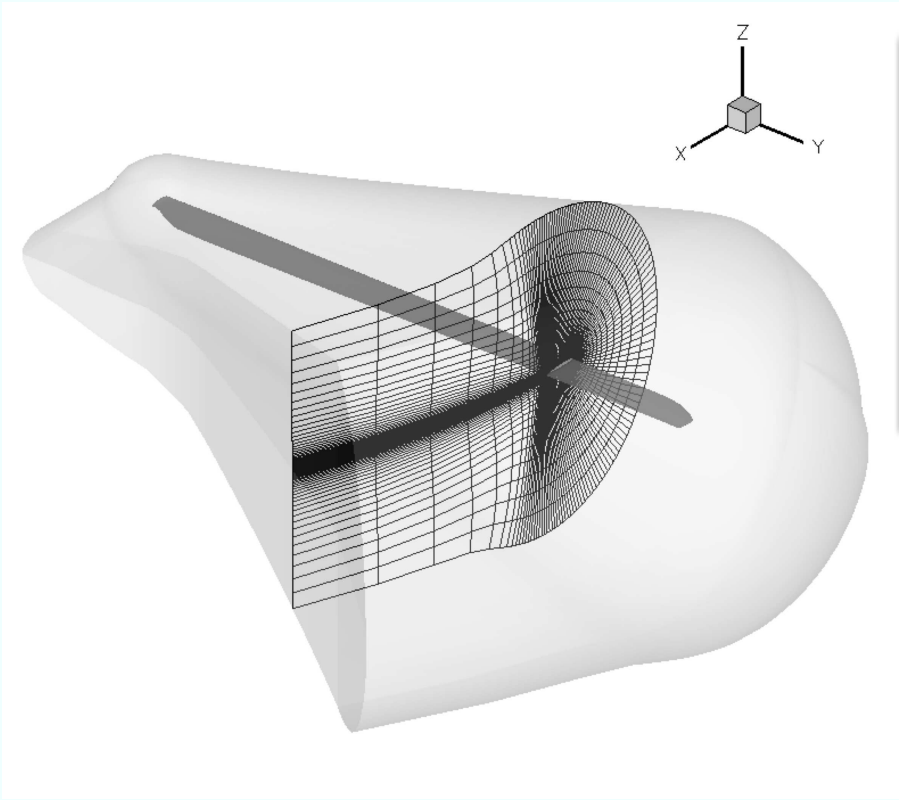

Figure 3: Figure showing the C-O mesh used for near-body flow computations.

The near-body solvers use the same body conforming C-O mesh used for the wake-coupling approaches. The entire rotor aerodynamic system is modeled by embedding the blade mesh in a cylindrical off-body mesh — see Fig. 4. The off-body mesh uses grid stretching to maintain clustering in regions of high vorticity, i.e., the root and tip vortex regions in the wake.

2.5 Acoustic Model

The rotor noise characteristics are calculated by solving the Ffowcs Williams-Hawkins (FW-H) equations.[37] Farassat's Formulation-1A[38, 39] is used to solve the FW-H equations. The acoustic solver (ACUM[25]) implements both on-surface and off-surface computations for acoustics.

For the on-surface solution, the deformed blade surface geometry along with flow variables on the surface obtained from CFD are used to solve the FW-H equations. For calculating the off-surface acoustics, the flow quantities at a chosen off-body surface are extracted from the CFD solution and input to the acoustics solver.

2.6 Python Coupling Framework

The coupling between the different solvers is achieved using Python scripts — see Fig. 2. Each solver provides a Python class interface which interacts with the FORTRAN modules using Fortran to Python Interface generator (F2PY). Parallelized execution of the code is achieved using pyMPI. The Python NumPy library is used for general array manipulation and data exchange between the solvers. While UMARC is used for the structural model in most of the analyses, the framework is generic enough to incorporate an alternate structural solver.

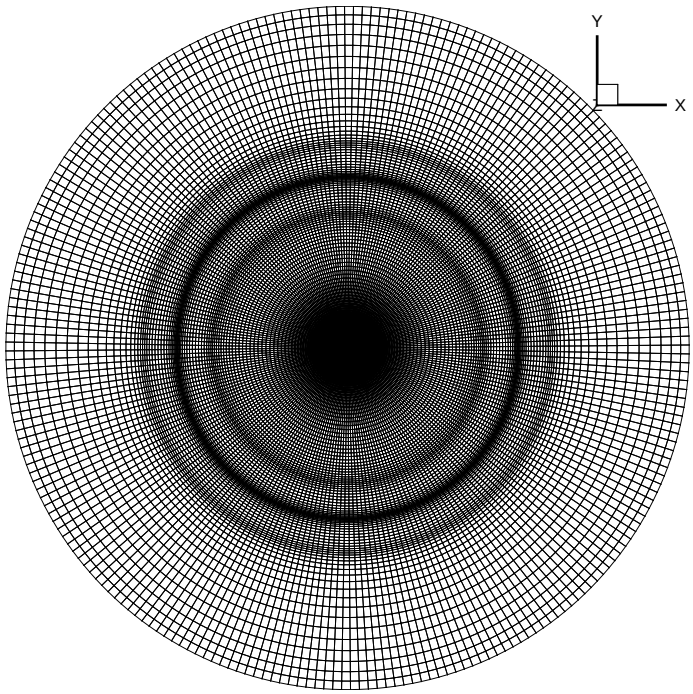

(a) Off-surface mesh

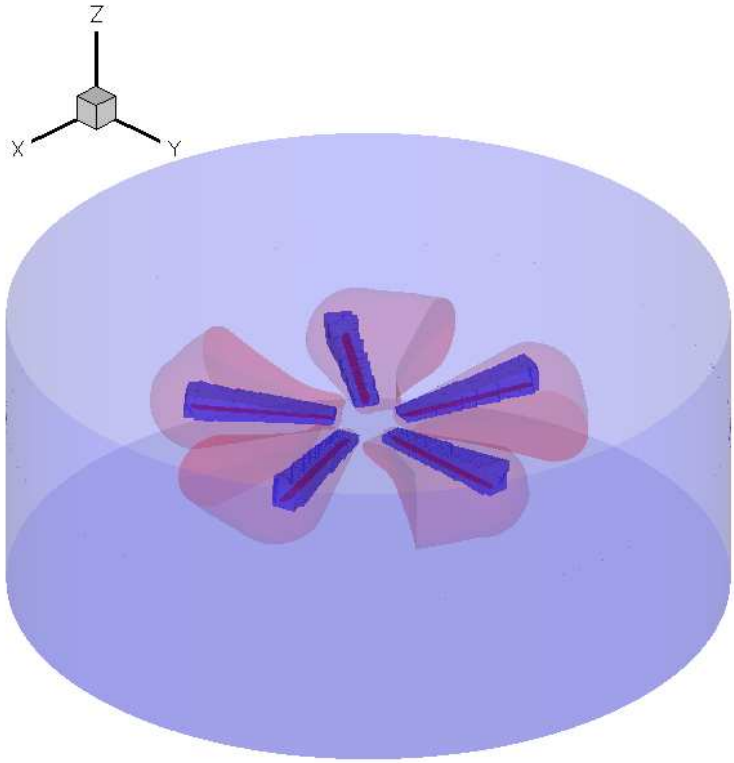

(b) Mesh system

Figure 4: Schematic showing the computational mesh system for the wake-capturing CFD analysis for the 5-bladed MDART rotor. (a) Top view of the cylindrical off-surface mesh, (b) near-body and off-body mesh system for wake capturing analysis, blue surfaces: off-body mesh boundaries, red surfaces: near-body mesh boundaries.

	Flight test	Wake-capturing SUmb+CDP+UMARC	Wake-coupling SUmb+PWAM+UMARC
Thrust (lb)	17287	17055 (-1.34%)	17292 ($\approx 0.00\%$)
Torque (lb-ft)	49000	48071 (-1.90%)	47878 (-2.29%)
Roll moment (lb-ft)	6884	6850 (-0.49%)	6892 ($+0.11\%$)
Pitch moment (lb-ft)	2583	2385 (-7.66%)	2464 (-4.60%)

Table 3: Comparison of the computed performance parameters with measured test data for the UH-60A C8534 flight condition. The numbers in parenthesis show the percentage error in predictions compared to the flight test data.

3 Results and Discussion

As mentioned previously, a comprehensive validation of the simulation framework was undertaken as part of the Helicopter Quieting Program. A wide gamut of flight conditions were analyzed for five different rotor configurations — see Table 1. Only representative results from each rotor configuration are presented in the following sections.

3.1 UH-60A Rotor Computations

As part of the NASA-Army UH-60A Airloads Program[15], extensive flight tests of a highly-instrumented UH-60A aircraft was conducted during 1993-1994. This extensive database contains data obtained from pressure transducers, strain gauges and accelerometers for over 900 flight conditions. The database is ideal for investigating the capabilities and deficiencies of coupled simulation tools. Five different flight conditions were analyzed using wake-coupling and wake-capturing methodologies. Results from two key steady flight conditions denoted by flight counters C8534 and C9017 are presented here. For the wake-coupling analysis SUmb with PWAM was used along with UMARC, and SUmb+CDP was used as the CFD solver for the wake-capturing analysis. The important physical characteristics and the operating flight conditions for these two cases are described in the following subsections along with the key results obtained from simulations.

3.1.1 C8534 — High-Speed, High-Vibration Flight

C8534 is a high-speed flight condition with a nominal weight coefficient $C_w/\sigma = 0.08$, an advance ratio $\mu = 0.368$, and a forward shaft-tilt angle $\alpha = -7.61^\circ$. Traditional rotor aeromechanics analyses failed to capture two key phenomena for this flight condition: 1. prediction of negative lift phase on the advancing side in high-speed flight, and 2. underprediction of pitch link load.[40] Figures 5 and 6 show the time histories of the normal force and pitching moment obtained using the comprehensive aeromechanic code UMARC (with inbuilt lifting line aerodynamics); notice the phasing of the negative lift peak outboard of $67\%R$. Furthermore, analysis is unable to capture the peak-to-peak values of airloads and moments near the rotor tip, where compressible effects strongly influence the blade aerodynamics.

Table 3 shows a comparison of the CFD-based computed performance parameters with measured data for this steady, high-speed flight condition. The computed values show good agreement with the test data for the integrated performance parameters.

Figures 7-9 show the time-histories of the non-dimensional, blade sectional normal force, pitching moment and chord force for the UH-60A rotor in this flight condition. The solid green line represents the results from the wake-capturing simulations, and the solid red line denotes the wake-coupling results. The flight test data is represented by the blue line. Compared to the baseline UMARC predictions (Fig. 5), the coupled CFD-CSD analysis shows a marked improvement in the prediction of the negative lift phase in the advancing side. Predictions from the coupled analyses show better agreement with measured flight test data for the pitching moment time histories (compare Fig. 8 with Fig. 6). The peak-to-peak normal forces and pitching moments are better resolved at the blade tips. This is because the CFD analysis is capable of resolving the compressibility effects accurately in the advancing side of the rotor disk. However, when

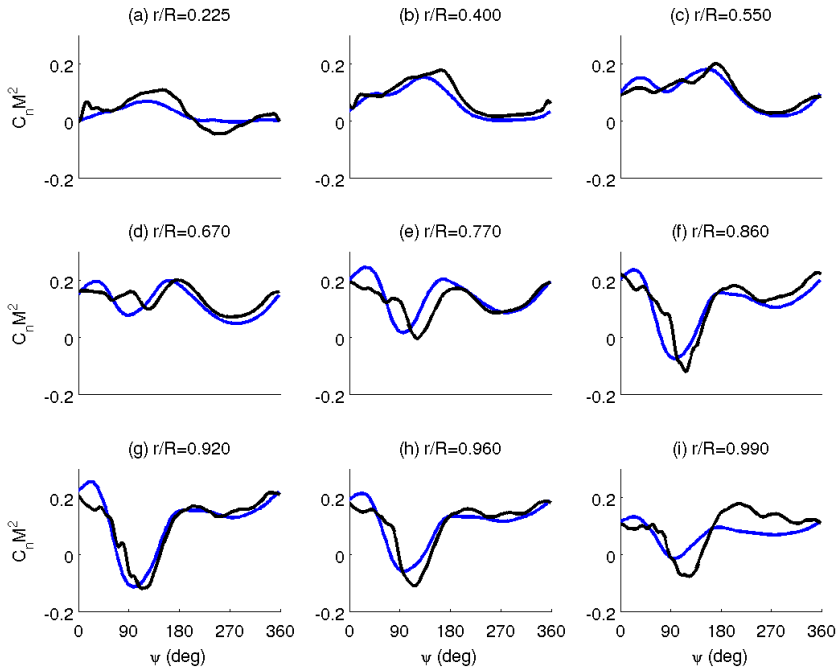

Figure 5: Time histories of the non-dimensional normal force at different blade sections for the UH-60A rotor C8534. Black: flight test data, blue: UMARC with lifting line aerodynamics.

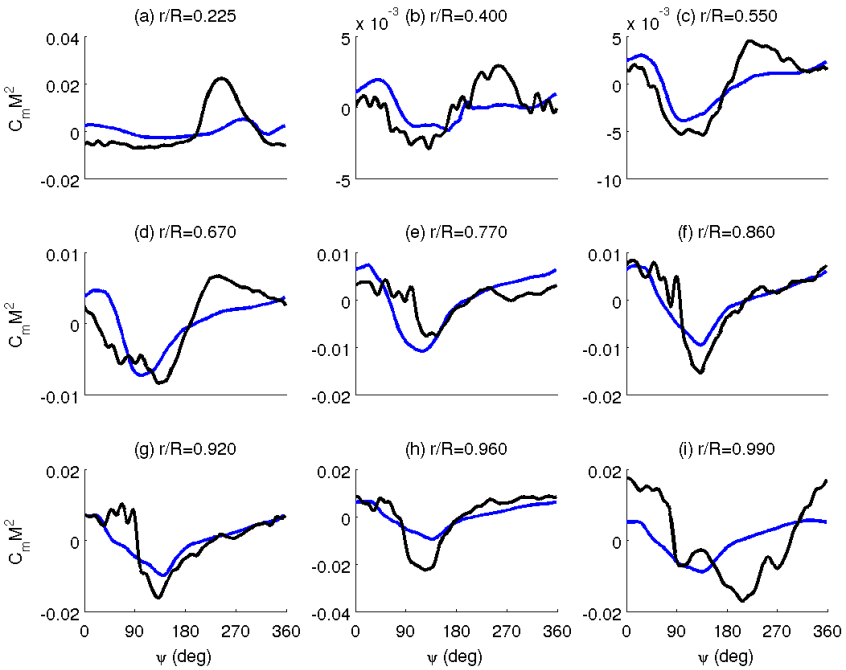

Figure 6: Time histories of the non-dimensional pitching moment (mean removed) at different blade sections for the UH-60A rotor C8534. Black: flight test data, blue: UMARC with lifting line aerodynamics.

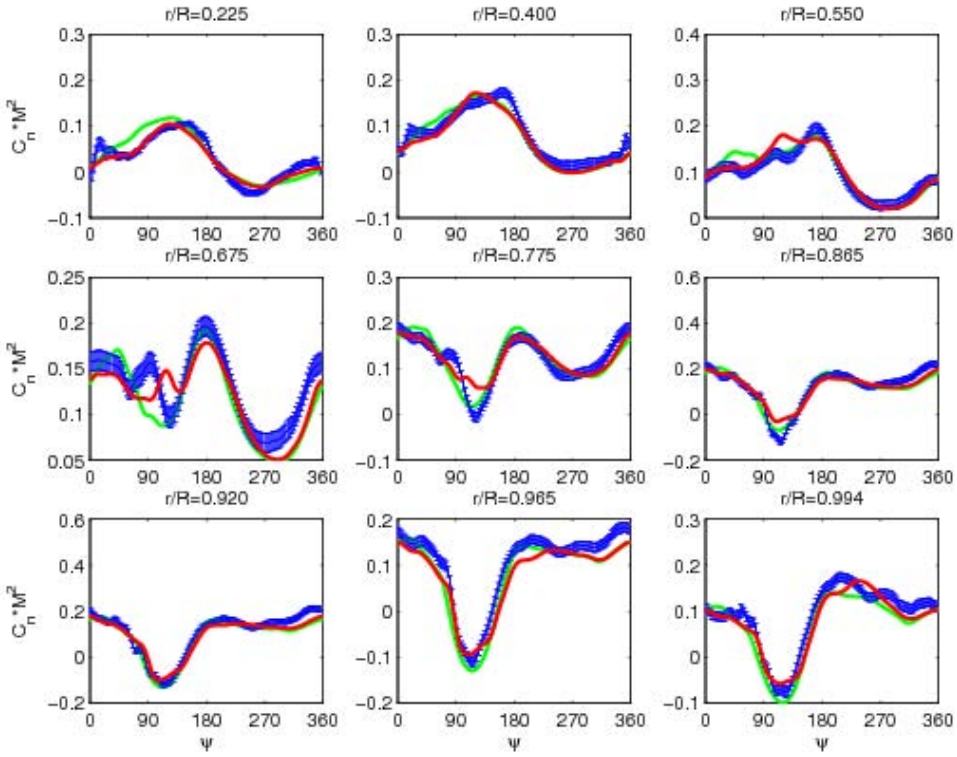

Figure 7: Time histories of the non-dimensional normal force at various blade sections for the UH-60A rotor c8534. Blue: flight test data, green: SUmb+CDP+UMARC, red: SUmb+UMARC.

compared to the test data there is an underprediction of the chordwise forces at the outer sections of the rotor blade especially near the advancing side of the rotor disk. The importance of a CFD-based aerodynamic solution is highlighted by the improvements seen in the prediction of the higher harmonics of the normal force distribution shown in Fig. 10. Both the wake-coupling (green lines) and the wake-capturing (red lines) solutions show a huge improvement in the phasing and magnitude of the higher harmonic airloads compared to the traditional lifting line aerodynamic solutions (black lines). The improvements in the aerodynamic predictions were also shown to improve the hub loads, especially the pitch link loads.[30]

To better understand the differences in the predictions and test data, the distribution of the pressure coefficients at different blade sections are analyzed. Figures 11 and 12 show the distribution of the chordwise non-dimensional pressure coefficient at sections $0.775R$ and $0.965R$ respectively at four azimuthal positions of the rotor blade. The solid lines show the results from wake-capturing methodology, and the dashed lines show the results from the wake-coupling methodology. The blue lines show the test data with experimental error bars. The predicted pressure distributions show favorable comparison with experimental data. The leading edge suction peaks are resolved quite accurately at all azimuths. During the advancing blade phase there is formation of a moving shock on the lower surface of the blade which is captured quite accurately by both the simulation approaches. The pressure distribution at 77% radial station shows poorer agreement compared to the 96% station. It must be noted that, in the test aircraft, a trim tab was present between 70-80% stations. The exact configuration of the trim tab is unknown and was, therefore, not modeled in the coupled simulations, which may be one of the reasons for the discrepancy at the 77% span station.

3.1.2 C9017 — High Altitude, High Thrust

C9017 is a high altitude flight condition with a nominal weight coefficient of $C_T/\sigma = 0.1325$, an advance ratio of $\mu = 0.237$. This flight condition is characterized by dynamic stall events on the retreating side and predicting these stall events poses a considerable challenge to most aerodynamic analyses. Two types of simulations were performed to study this stall flight case: 1. the wake-capturing CFD simulation (SUmb+CDP) with the motions prescribed from a separate CFD-CSD coupling simulation[3], and 2. a fully coupled, wake-capturing simulation (SUmb+CDP+UMARC).

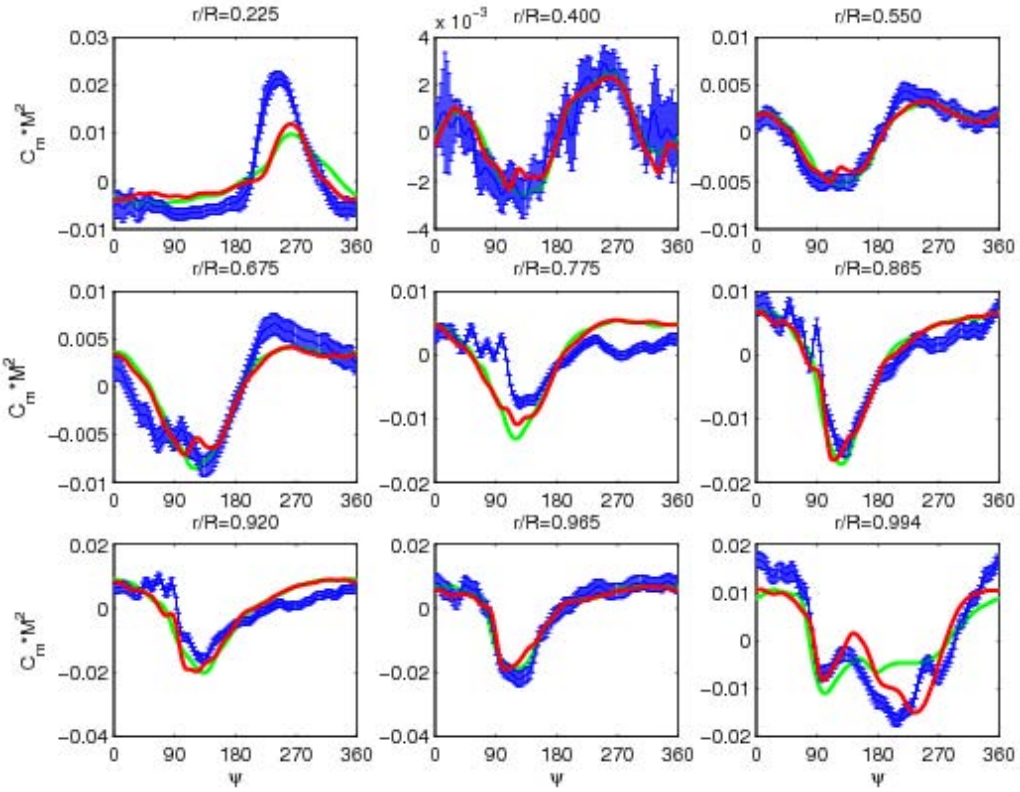

Figure 8: Time histories of the non-dimensional pitching moments (mean-removed) at various blade sections for the UH-60A rotor c8534. Blue: flight test data, green: SUmb+CDP+UMARC, red: SUmb+UMARC.

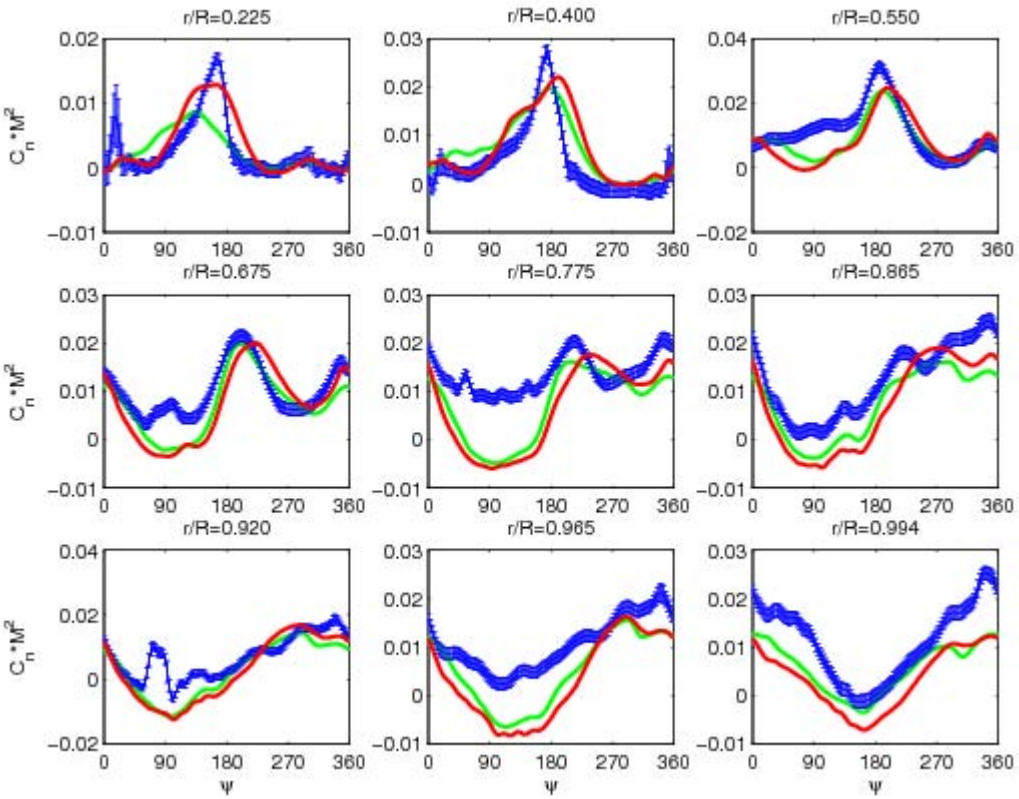

Figure 9: Time histories of the non-dimensional chordwise force (mean-removed) at various blade sections for the UH-60A rotor c8534. Blue: flight test data, green: SUmb+CDP+UMARC, red: SUmb+UMARC.

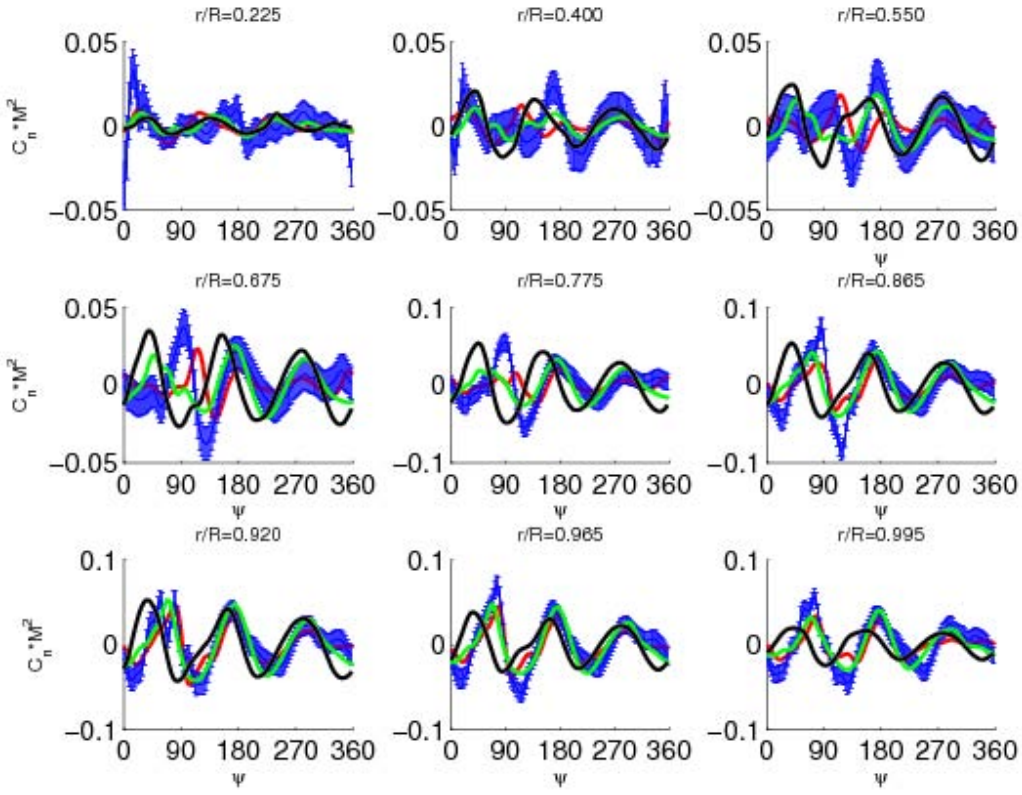

Figure 10: Time histories of the higher harmonics (3-20/rev) of the sectional blade normal forces for the UH-60A rotor (C8534). Blue: flight test data, green: SUmb+PWAM+UMARC, red: SUmb+CDP+UMARC, black: UMARC lifting-line aerodynamics.

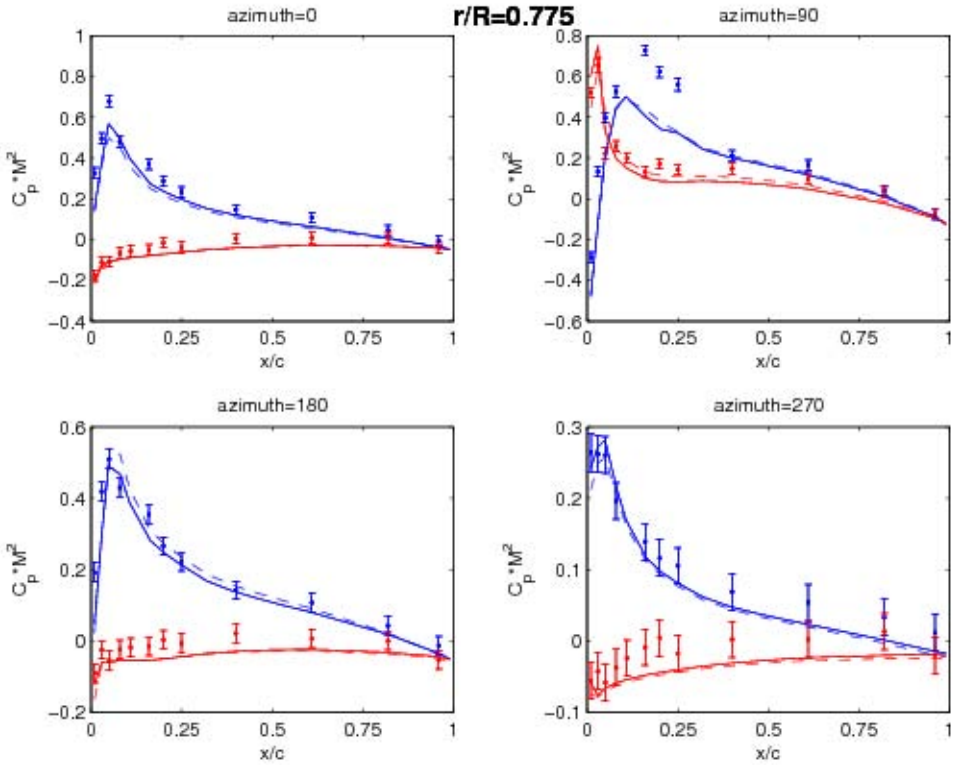

Figure 11: Chordwise distribution of the pressure coefficient results from the wake-coupling and the wake-capturing simulations at $r/R = 0.775$ for flight C8534. Blue: flight test data with error bars, solid red: wake-capturing, dashed red: wake-coupling.

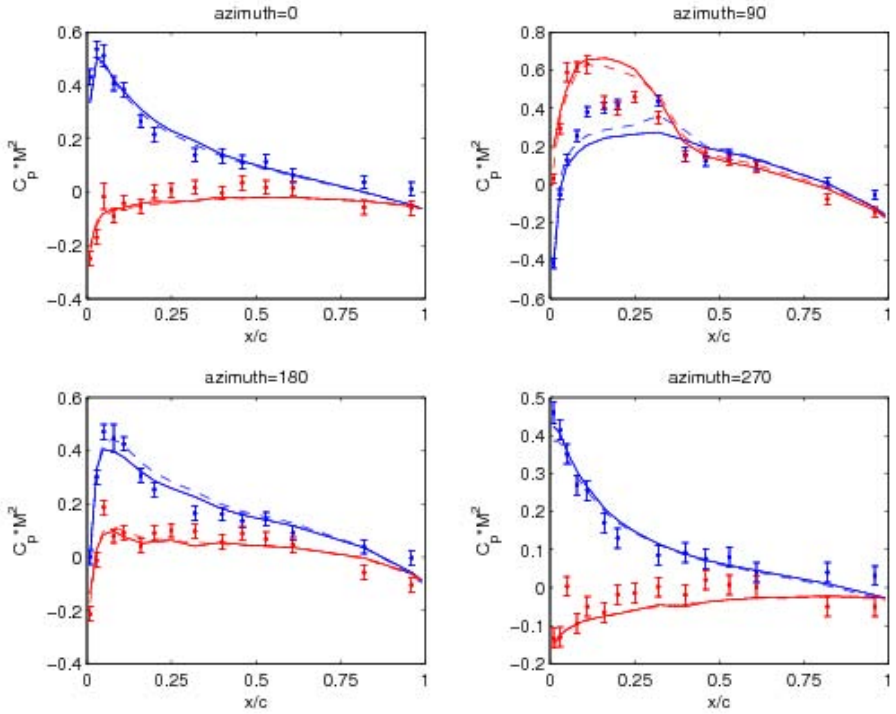

Figure 12: Chordwise distribution of the pressure coefficient predictions from the wake-coupling and wake-capturing analyses at $r/R = 0.965$ in comparison with flight test data for C8534. Blue: flight test data with error bars, solid red: wake-capturing (SUmb+CDP+UMARC), and dashed red: wake-coupling (SUmb+PWAM+UMARC).

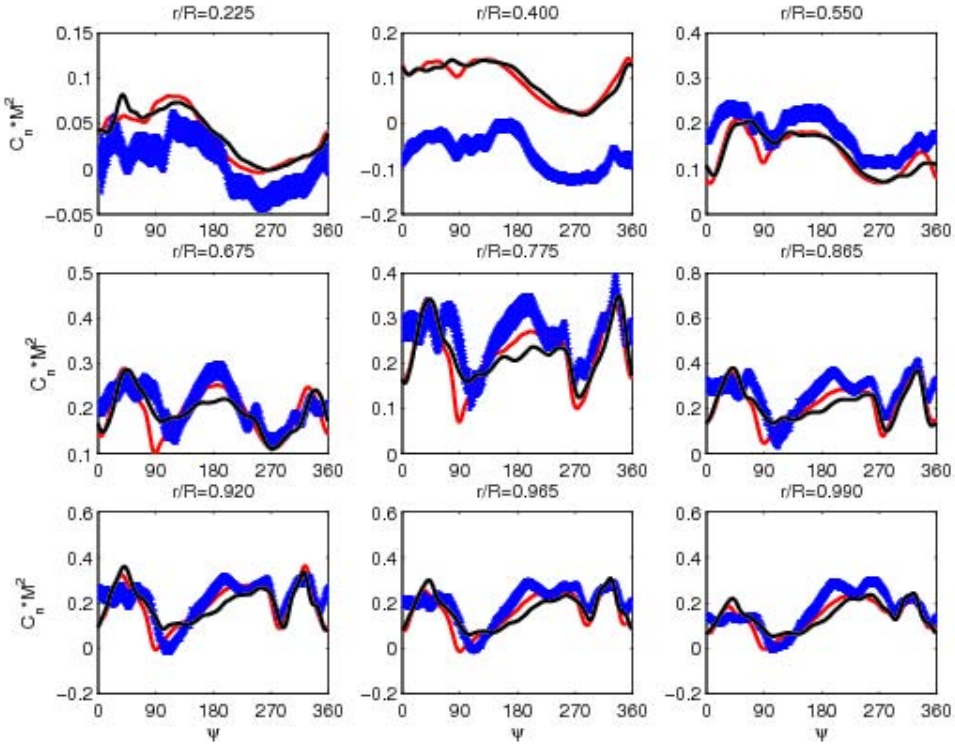

Figure 13: Time-histories of the non-dimensional, sectional normal force distributions for flight C9017. Blue: flight test data, red: coupled wake-capturing simulation, black: wake-capturing solution with prescribed motions.

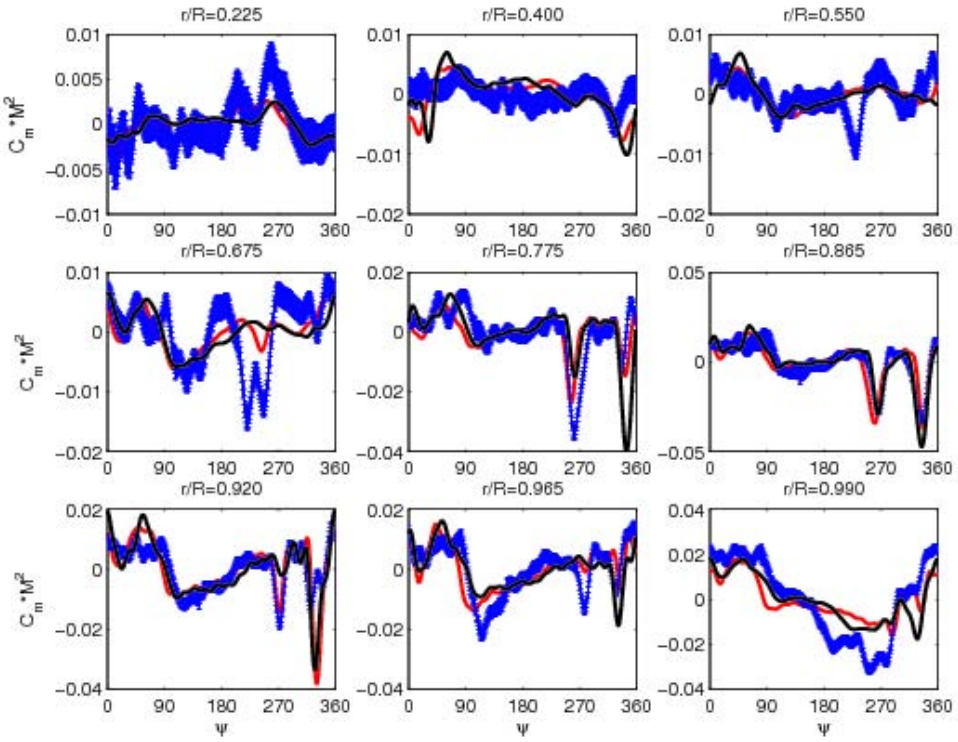

Figure 14: Time-histories of the non-dimensional, sectional pitching moment distributions (mean removed) for flight C9017. Blue: flight test data, red: coupled wake-capturing simulation, black: wake-capturing solution with prescribed motions.

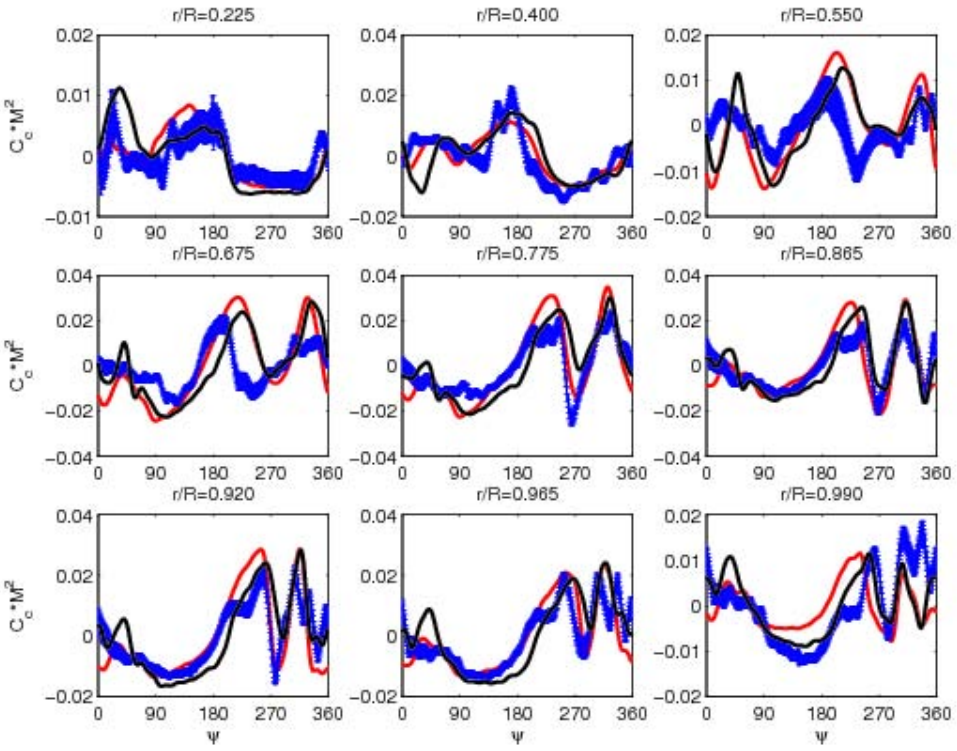

Figure 15: Time-histories of the non-dimensional, sectional chord force distributions (mean removed) for flight C9017. Blue: flight test data, red: coupled wake-capturing simulation, black: wake-capturing solution with prescribed motions.

Table 4: Details of the microphone locations used in the DNW rotor test.

Microphone	x/R	y/R	z/R	ψ^a	ζ^b
1	-3.00	0.00	0.00	-0	0
2	-2.60	1.50	0.00	-30	0
3	-2.60	-1.50	0.00	30	0
4	-2.90	0.00	-0.78	-0	-15
5	-2.51	1.45	-0.78	-30	-15
6	-2.51	-1.45	-0.78	30	-15
7	-2.72	0.00	-1.27	-0	-25
8	-2.35	1.36	-1.27	-30	-25
9	-2.35	-1.36	-1.27	30	-25

[a] Angle with respect to the freestream direction. +-ve: port, −-ve: starboard
[b] Vertical angle from the plane of the rotor disk.

Table 5: Comparison of the computed performance parameters for the DNW 1310 rotor with experimental measurements. The numbers in parentheses show the percentage error in predicitons.

	Experiments	Wake-capturing SUmb+CDP+UMARC	Wake-coupling SUmb+PWAM+UMARC
Thrust (lb)	576.3	579.6 (0.6%)	577.9 (0.3%)
H force (lb)	-10.22	-4.9 (−52.1%)	-4.0 (−60.9%)
Y force (lb)	-25.23	-27.71 (9.8%)	-22.61 (−10.4%)
Lift (lb)	575.27	578.19 (0.5%)	575.80 (0.1%)
Propulsive force (lb)	36.13	50.35 (39.4%)	49.32 (36.5%)
Torque (lb-ft)	166.9	164.8 (−1.3%)	172.6 (−3.4%)
Roll moment (lb-ft)	8.29	7.13 (−14.0%)	6.13 (−26.1%)
Pitch moment (lb-ft)	-23.97	-27.97 (−16.7%)	-23.64 (−1.4%)

Figures 13–15 show the time histories of the spanwise normal force, pitching moments, and chord force respectively. The trends in the airloads distribution are captured well by both analyses. There is some discrepancy in the mean value of the normal lift distribution near the $40\%R$ radial section. The flight test data appears to suggest a large spanwise discontinuity at 40%R which is most probably a manifestation of steady offsets present in the flight test data. The pitching moment variations at the outboard sections of the blade are characterized by two distinct stall events. These stall events are highly aero-elastic in nature. The first stall event is caused by an increase in angle of attack induced by pitch control variations. The large nose-down pitching moment impulse produced by the first stall event causes and elastic torsional response (dominantly 5/rev) which leads to flow reattachment and stall recovery of the pitching moments. In a few degrees of azimuthal travel the elastic response becomes out of phase with the pitch control variation causing the blade to stall again. Both the blade stall events are captured by the coupled simulation although not resolved accurately in magnitude and phase. There is a slight underprediction of the magnitude of the first stall at certain blade sections (see sections $r/R = 0.675$ and $r/R = 0.775$ in Fig. 14), and the simulations miss the moment stall event at $r/R = 0.965$. However, the overall predictions from the coupled analysis is very good, and provides confidence in the structural model being used for the simulations.

3.2 Model DNW rotor Test

A model rotor was tested at the Duits-Nederlandse Windtunnel (DNW) in 1989.[16, 17] The tests included comprehensive acoustics data for nine microphone locations — see Table 4. The microphones were located on a hemisphere of radius $3R$ from the center of the rotor hub below the plane of rotor disk. Three microphones (Mics 1–3) were located in-plane, and the rest were located out of plane of the rotor 15° below the rotor plane. Three microphones were located directly upstream of the rotor, and three each at 30° to the freestream direction on the starboard and port respectively. The analysis was performed with both wake-capturing and wake-coupling CFD solutions coupled with UMARC in forward flight condition with an advance ratio of $\mu = 0.3014$ and a forward shaft tilt angle of $\alpha_s = -4.49°$.

Table 5 shows the computed performance values from the two simulations in comparison to the experimental measurements. The predictions of the rotor thrust and torque are satisfactory. The predictions of the rotor horizontal force

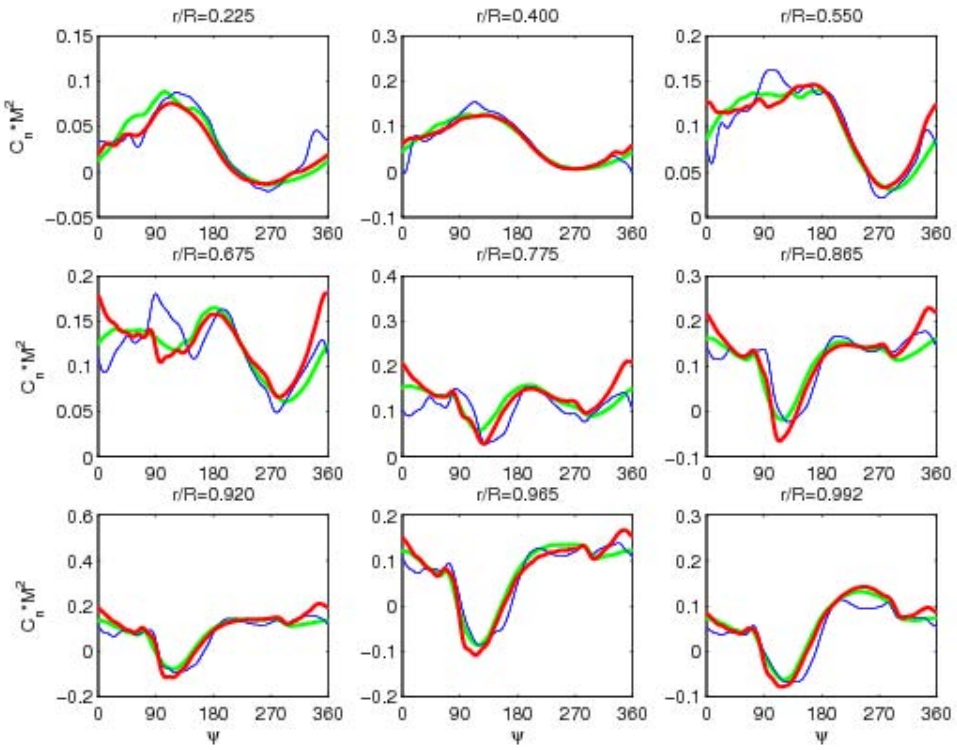

Figure 16: Time-histories of the non-dimensional, sectional normal force distributions for flight DNW1310. Blue: flight test data, red: coupled wake-capturing simulation, black: wake-capturing solution with prescribed motions.

shows about 60% underprediction when compared with experimental data. The horizontal force underprediction is reflected in the under-prediction of the propulsive force as well. However, the magnitude of the underprediction is only about 5 lb. The rotor mast and mounts used in the wind-tunnel are not modeled in the simulations and may account for this discrepancy.

Figures 16–18 show the time-histories of the normal force, pitching moment, and chordwise force at various radial sections of the rotor blade for the DNW1310 rotor. The two simulations show good agreement with experimental measurements for the normal force and pitching moment time histories. There are some differences in the chordwise force distribution near the tip of the rotor blade. Similar behavior was observed for the UH-60A C8534 flight condition also — see Fig. 9. The discrepancies in the chord forces could explain the differences observed in the predicted horizontal force values when compared to experiments (Table 5).

Figure 19 shows the time-histories of the total acoustic pressure at the nine microphone locations (see Table 4). Results from the on-surface computations for both the wake-capturing and wake-coupling analyses are shown (using green and magenta lines respectively). In addition, the results from the off-surface acoustics using the CFD solution from the wake-capturing analysis are shown with the red lines. The blue lines show the experimental data. All three calculations capture the essential trends in the acoustic time histories. However, the on-surface acoustics does not resolve the fluctuations in acoustic pressure before the negative pulse. These fluctuations arise from the quadrupole terms in the FW-H equation, and these terms are not captured by the on-surface acoustics but are better resolved in the off-surface calculations.

The predictive capabilities of the on-surface and off-surface methodologies are better understood by analyzing the acoustic time histories of the in-plane microphones shown in Fig. 20. The on-surface results fail to capture the fluctuations in front of the negative pulse completely – see Fig. 20(a), while the off-surface calculations capture the qualitative nature of the quadrupole noise observed in the experimental data. The improved prediction from the off-surface acoustic methodology is illustrated more clearly in Figs. 20(d)—(f) where the spectral variation of the noise data is presented. The off-surface acoustic calculations show much improved agreement of the noise content with the experimental data.

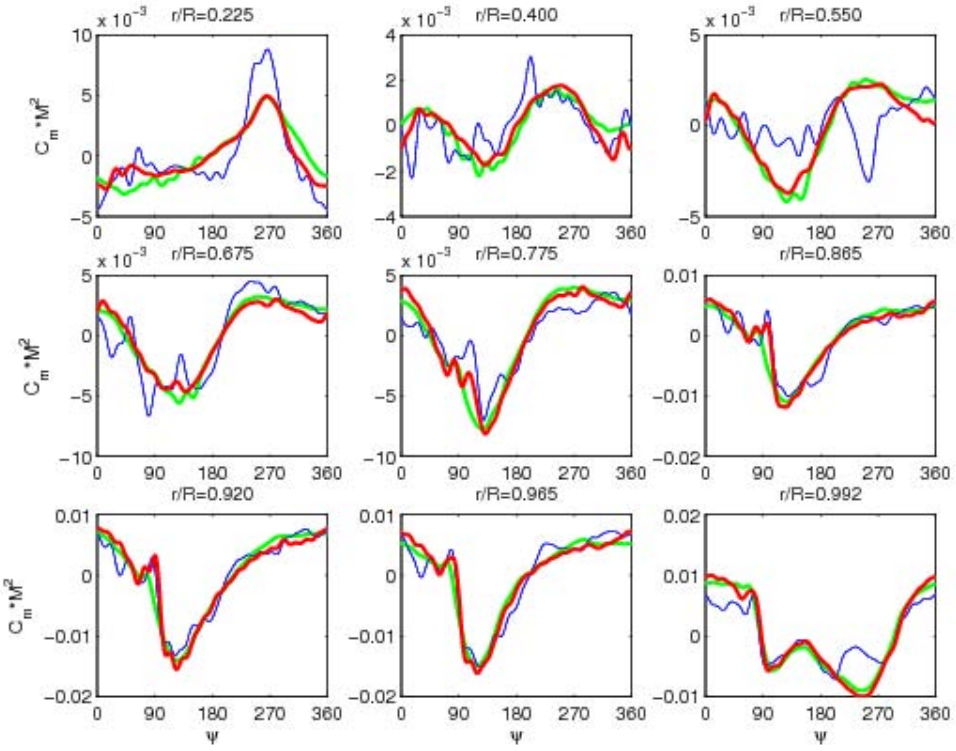

Figure 17: Time-histories of the non-dimensional, sectional pitching moment distributions (mean removed) for flight DNW1310. Blue: flight test data, red: coupled wake-capturing simulation, black: wake-capturing solution with prescribed motions.

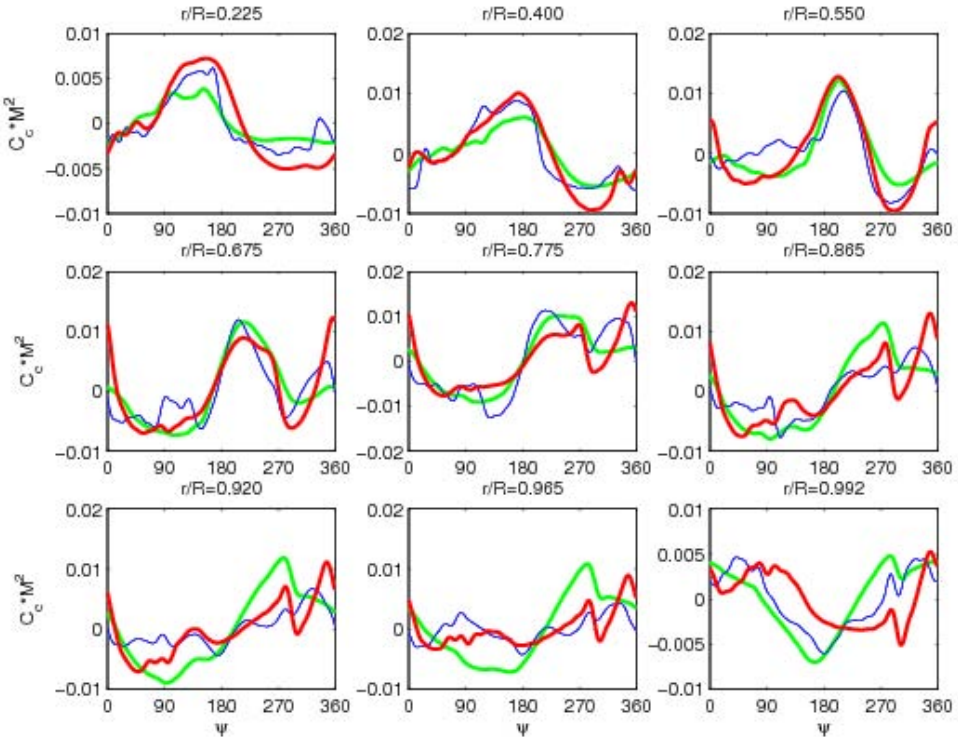

Figure 18: Time-histories of the non-dimensional, sectional chord force distributions (mean removed) for flight DNW1310. Blue: flight test data, red: coupled wake-capturing simulation, black: wake-capturing solution with prescribed motions.

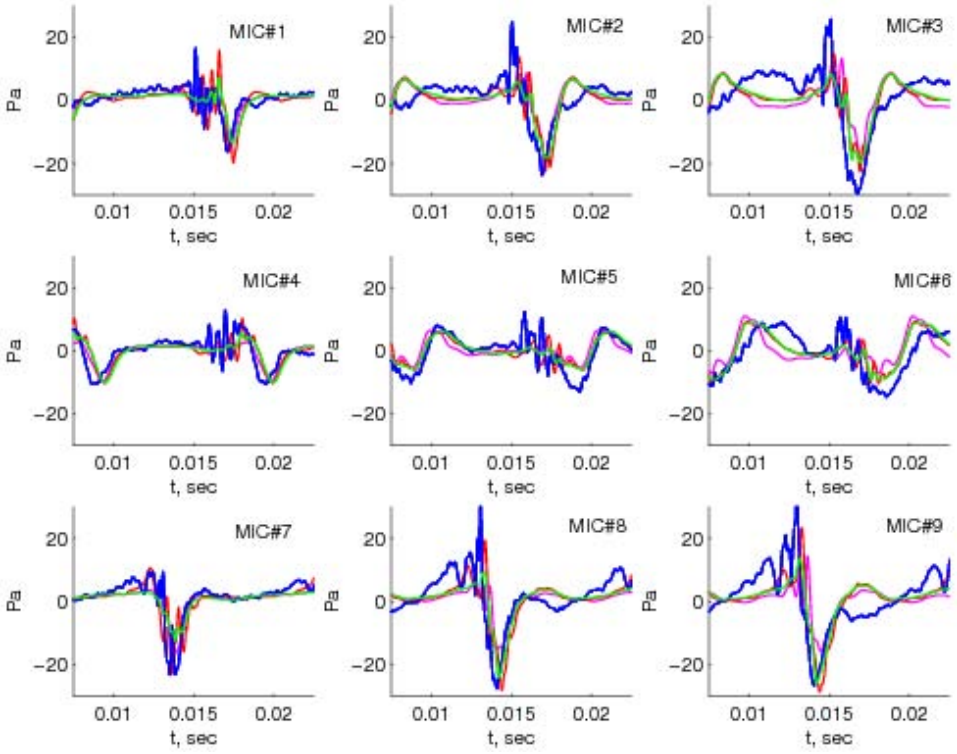

Figure 19: Comparison of the time histories of the total acoustic pressure at the nine microphone locations for the DNW 1310 rotor predicted by the coupled analyses using on-surface and off-surface acoustics. Blue: experimental measurements, red: SUmb+CDP+UMARC (off-surface acoustics), green: SUmb+CDP+UMARC (on-surface acoustics), magenta: SUmb+PWAM+UMARC (on-surface acoustics).

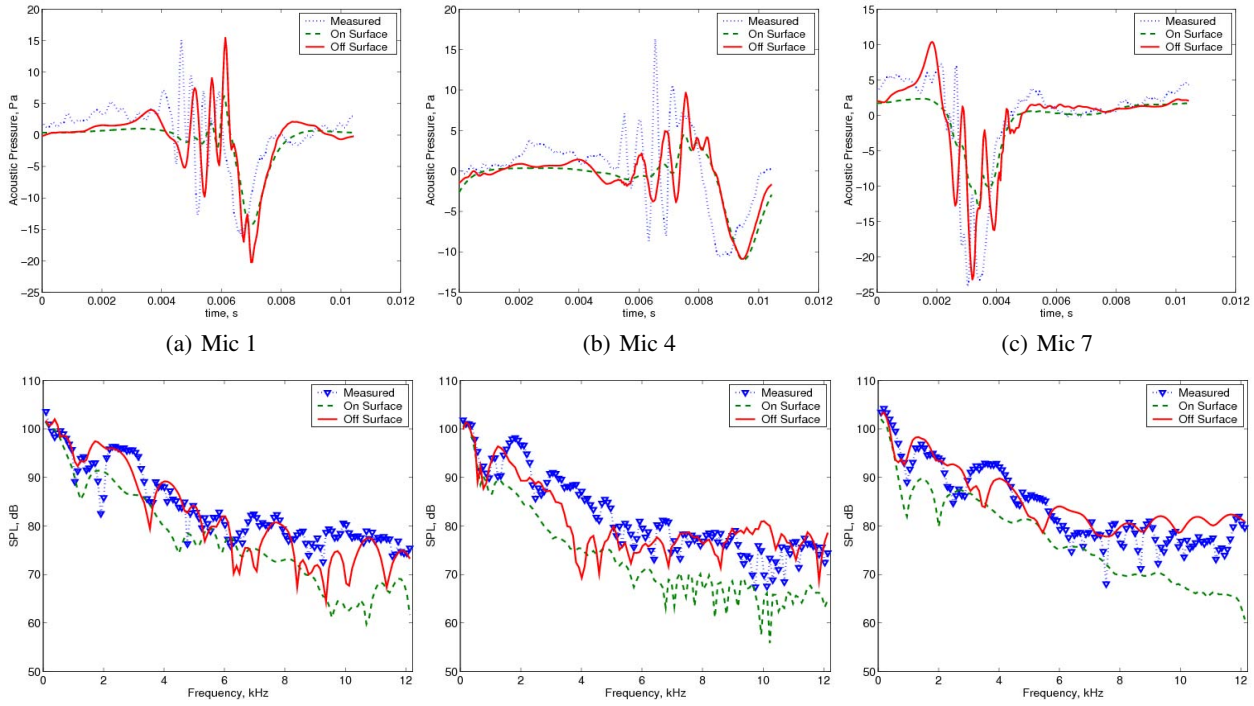

(a) Mic 1 (b) Mic 4 (c) Mic 7

(d) Mic 1 (e) Mic 4 (f) Mic 7

Figure 20: Comparison of the on-surface and off-surface time history predictions of the total acoustic pressure at in-plane microphones 1, 4, and 7 for the DNW 1310 test rotor. (a)–(c): acoustic pressure time history, (d)—(f) Sound pressure levels vs. frequency.

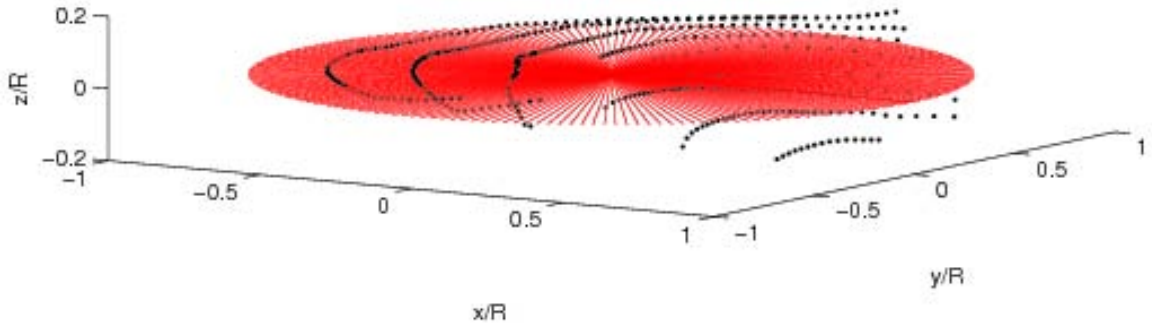

(a) Isometric view

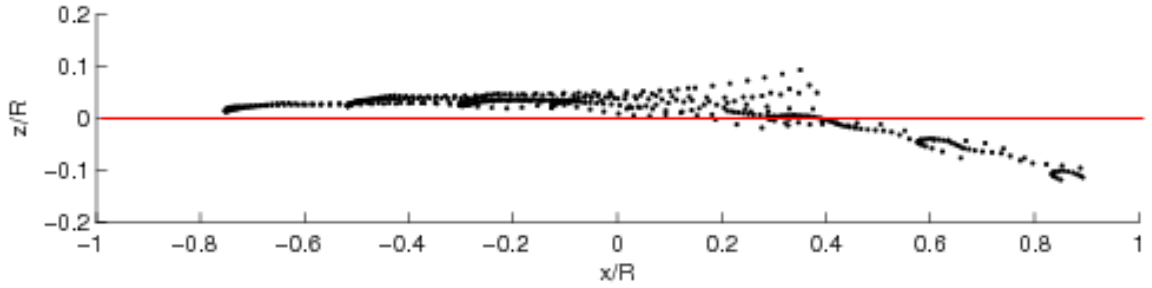

(b) Side view

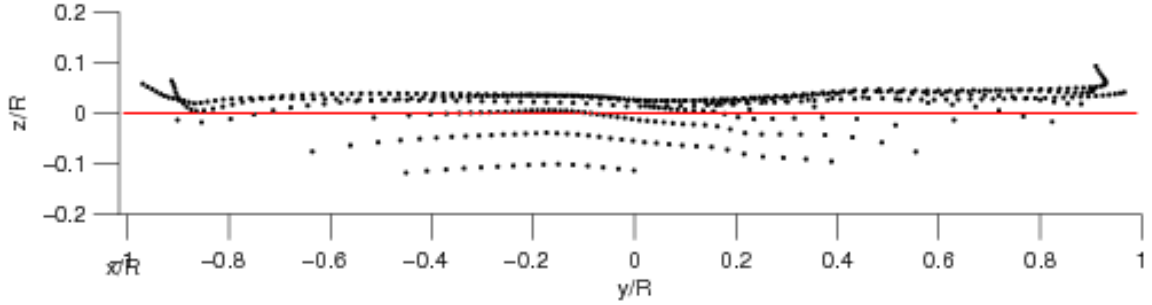

(c) Rear view

Figure 21: Plots showing the loci of the blade-vortex interactions for the HART-II baseline flight condition.

3.3 HART-II Rotor computations

The Higher harmonic control Aeroacoustics Rotor Test (HART-II) was a joint effort by DLR, ONERA, NASA Langley, and AFDD to conduct a comprehensive test on a 40%-geometrically and aeroelastically scaled model of a bearingless BO-105 main rotor.[18] The experiment was conducted in an open-jet anechoic test section, with the objective of improving the basic understanding of the rotor blade-vortex interaction (BVI) with and without higher harmonic pitch control (HHC) on rotor noise and vibration. Comprehensive acoustic data is available for rotor acoustics, blade surface pressures and blade deformations which can be used to validate the coupled analyses. Results from three flight conditions: 1. baseline, 2. minimum vibration, and 3. minimum noise are available. The last two cases use HHC to control vibration or noise. Detailed analysis has been performed previously for the three cases using UMARC and UMTURNS within the HUSH framework.[25] Only the results from the wake-coupling scheme (SUmb+PWAM) for the baseline low-speed transition flight condition with an advance ratio $\mu = 0.1508$ and a shaft-tilt angle $\alpha_s = 4.5^\circ$ are shown here.

At this flight condition, the wake vortices cut through the rotor plane (see Fig. 21) and cause strong blade-vortex interactions (BVIs) which are the main source of rotor noise and its directivity. Figure 22 shows the time-histories of the non-dimensional normal force distribution and its first derivative at $r/R = 0.87$. The first subplot shows the normal force distribution during the entire rotor revolution, the second subplot shows the contribution of the higher harmonics

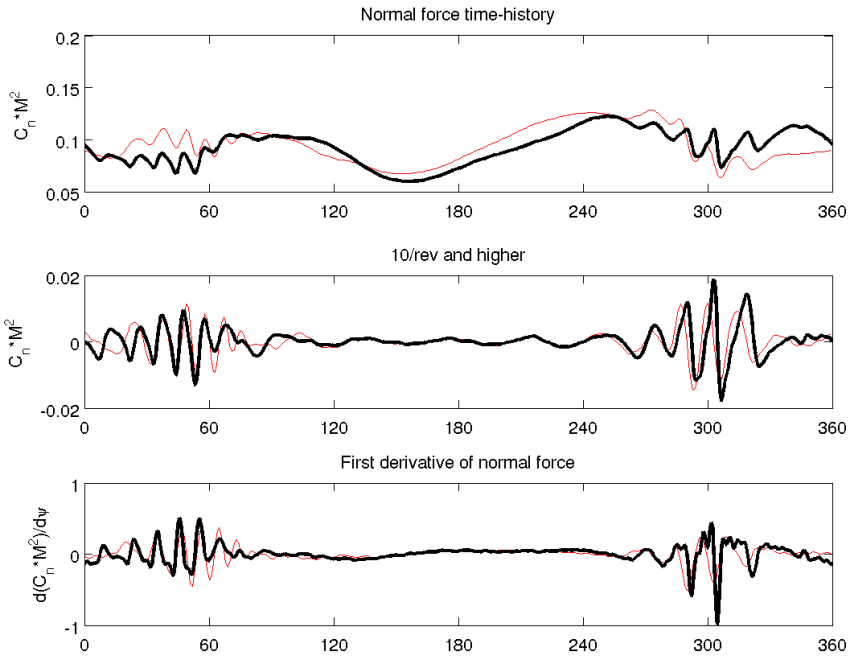

Figure 22: Time-history of the non-dimensional normal force and its derivative at $r/R = 0.87$ for the coupled analyses in comparison to measured experimental values. Black: Measurements, Red: SUmb+PWAM+UMARC coupled analysis

($\geq 10/rev$), and the third subplot shows the first derivative of the normal force. The derivatives and the higher harmonics were obtained using a spectral analysis of the force history. Notice that the time-histories of the higher harmonics of the normal force and the derivative of lift show good agreement with experimental measurements. This provides confidence in the capability of the wake modeling to capture BVIs.

Figure 23 shows the contours of the overall sound pressure levels (SPL), the BVISPL (6-35 blade passage frequencies), and the low SPL (1-5 blade passage frequenices for the HART-II rotor at this flight condition. The BVI SPL shows excellent agreement compared to the experiments. Previous research using wake-capturing methodology showed a 5dB under prediction in the BVISPL.[41] This gives further confidence in the capability of the wake modeling used in the present analysis. However, the low SPL, and therefore the OASPL, results do not show good agreement with the experiments. This is because of a discrepancy in the lower harmonics of the normal force distribution — see Fig. 22. There is some ambiguity in the pitch link stiffness which affects torsional frequency and elastic torsional response which is the key contributor to phase of lower harmonic lift and pitching moment.

3.4 MDART Rotor computations

The McDonnell Douglas Advanced Rotor Technology (MDART) rotor is a five-bladed, soft-inplane bearingless rotor and is essentially a pre-production version of the MD900 rotor used in the joint NASA-McDonnell Douglas MDART test program[19]. The baseline flight condition chosen was a high-speed forward flight condition ($\mu = 0.3$) with forward shaft tilt angle $\alpha_s = -9.1^\circ$, and operating thrust condition $C_T/\sigma = 0.08$. This case was analyzed extensively by exercising all the different CFD codes available in the framework. Comprehensive comparisons between the predictive capabilities of the baseline lifting line analysis, wake-coupling and wake capturing analysis were performed.[42] Only structural flap, chord and torsion bending moment data are available from the experiments, so only comparisons of predictions for these loads are shown here.

Figures 24-26 show the flap, chord, and torsion bending moment predictions from different analyses in comparison to the experimental measurements. The mean values have been removed from both the predictions and the experiments in those plots. In the plots, the black circles are the measured values from experiments, the red lines are the predictions by

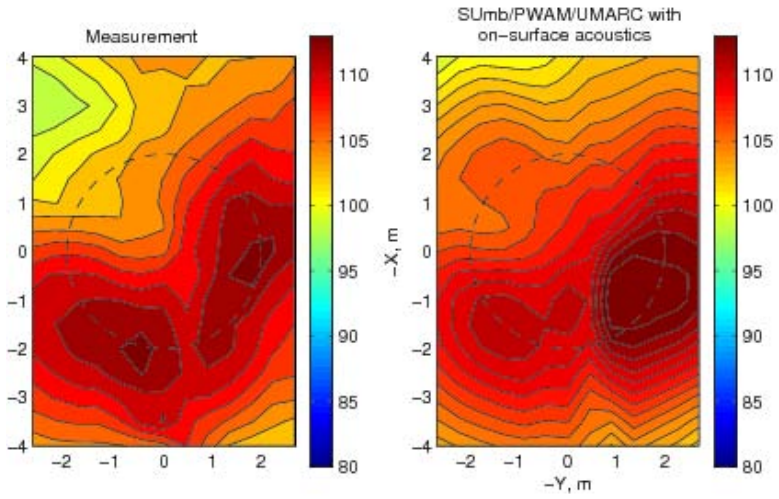

(a) Overall SPL

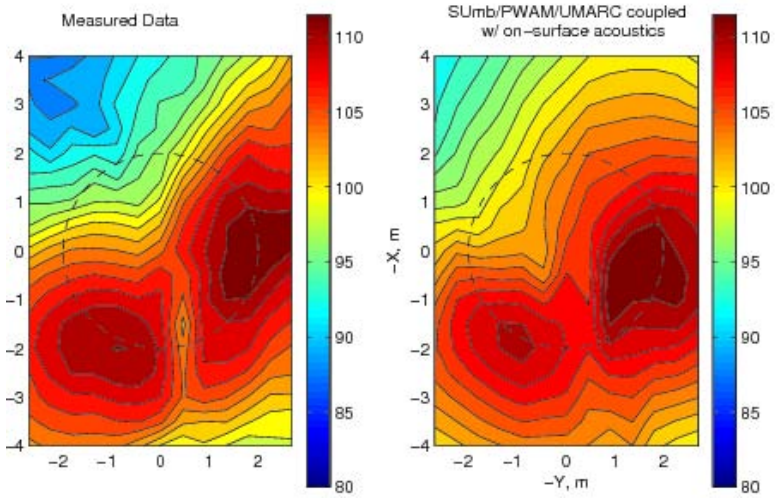

(b) BVI SPL

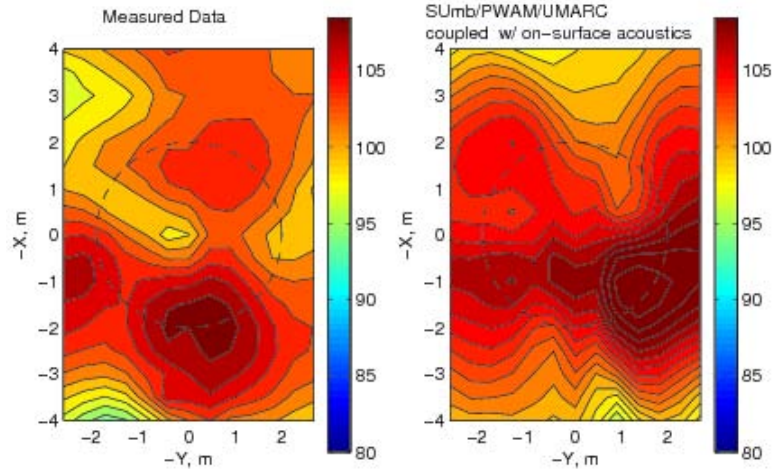

(c) Low SPL

Figure 23: Contours of the sound pressure levels for the HART-II baseline flight condition. (a) Aggregating all blade passage frequencies, (b) Aggregating 6-35 blade passage frequencies, (c) aggregating 1-5 blade passage frequencies.

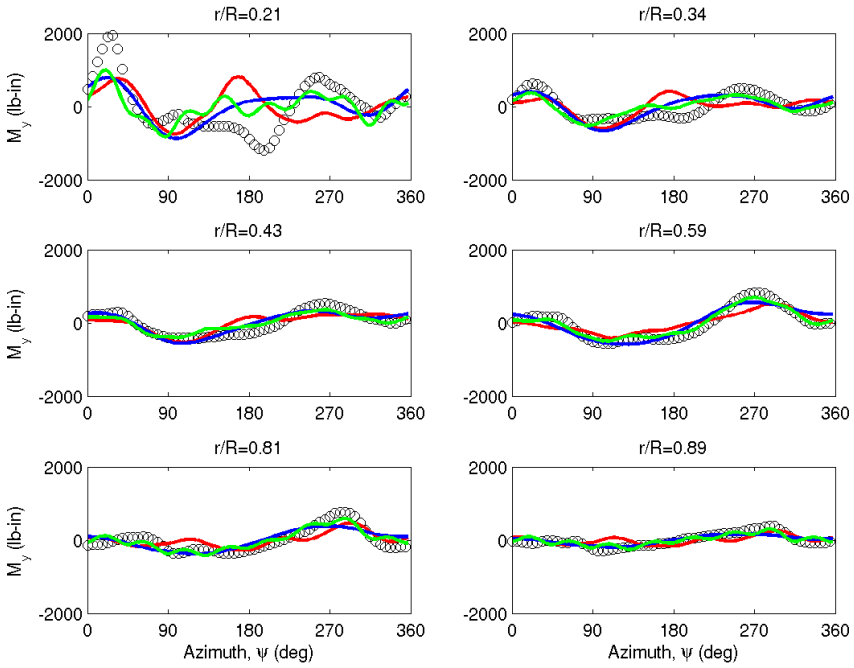

Figure 24: Time histories of the flap bending moments at various blade sections for the MDART rotor. $C_T/\sigma = 0.08, \mu = 0.3, \alpha = -9.1^\circ$. Black: experiments, red: UMARC lifting-line analysis, blue: SUmb+UMARC, green: OVERTURNS+UMARC.

the UMARC lifting-line analysis, the blue lines are the results from the wake-coupling analysis, and the green lines are the results from the wake-capturing analysis. UMARC with lifting line model is capable of capturing the overall trends in the loads in the mid-span sections. However, the agreement is poor towards the tip and the root sections. At the tip the chordwise bending moment predictions do not seem to capture the right phase. The peak-to-peak values for the torsion moments are underpredicted by the standalone UMARC calculations. Compared to the standalone UMARC predictions, both the coupled analyses are able to capture the flap bending moments more accurately at all spanwise sections. The predictions at the mid-span locations are extremely encouraging. Both CFD/CSD methodologies also predict the peak-to-peak values in the torsion moments better than the standalone UMARC case. However, the prediction of the chord bending moments are poor compared to the standalone UMARC predictions. This needs further investigation to better understand why the lifting line aerodynamics performs better than coupled CFD-CSD analyses.

3.5 SMART Rotor with Trailing-Edge Flaps (TEF)

The smart material actuated rotor (SMART) is geometrically similar to the MDART rotor presented in the previous section. Each blade has a single trailing edge flap (TEF) spanning approximately 18% of the rotor radius outboard of the rotor blade. The flight conditions chosen for the SMART rotor are the same as the MDART baseline, an advance ratio $\mu = 0.3$, a forward shaft-tilt angle $\alpha_s = -9.1^\circ$, and $C_T/\sigma = 0.08$. However, a flap deflection schedule $\theta_{TEF}(\psi_b) = 2^\circ \sin(3\psi_b + 60)$ was applied to study the effect on trailing edge flaps on rotor performance and noise. In the present analysis, the CFD solver modeled the flap as an integrated flap, i.e., the effect of the gaps between the flap and the blade were neglected. The flap deflections were modeled by deforming the near-body grid in the vicinity of the trailing edge flap to conform to the blade geometry and flap orientation near the surface of the blade. Appropriate decay parameters were applied to gradually diminish the effect of flap deflection on the grid in regions far away from the flap. The results are compared to the baseline UMARC lifting line solution where appropriate. Detailed analysis of the structural bending moment data was performed previously.[42] No experimental data is publicly available for this rotor at this time, so only a preliminary analysis of this rotor is presented here.

Figure 27 shows the azimuthal variations of the normal force at various spanwise sections of the rotor blade for the

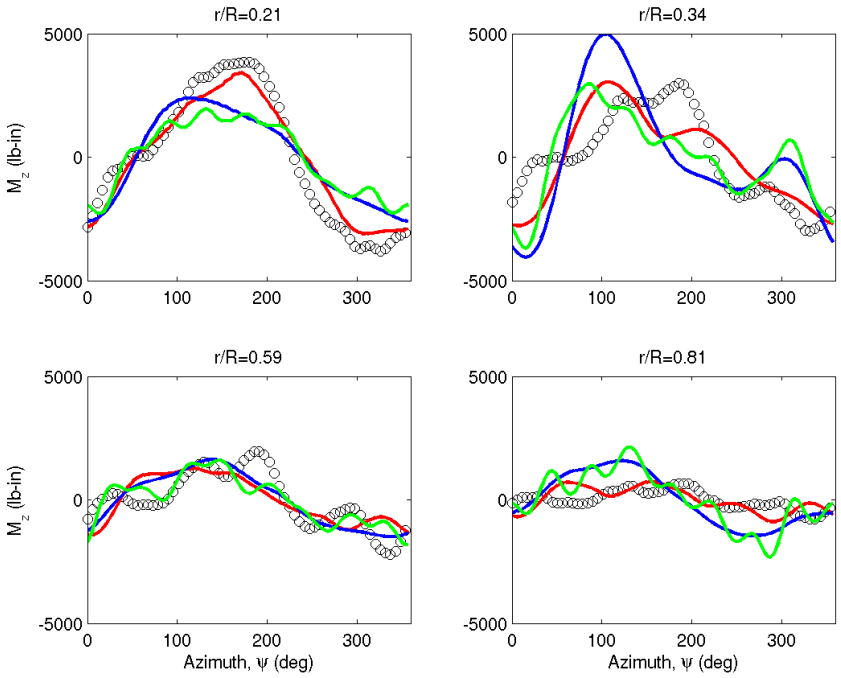

Figure 25: Time histories of the chord bending moments at various blade sections for the MDART rotor. $C_T/\sigma = 0.08, \mu = 0.3, \alpha = -9.1^\circ$. Black: experiments, red: UMARC lifting-line analysis, blue: SUmb+UMARC, green: OVERTURNS+UMARC.

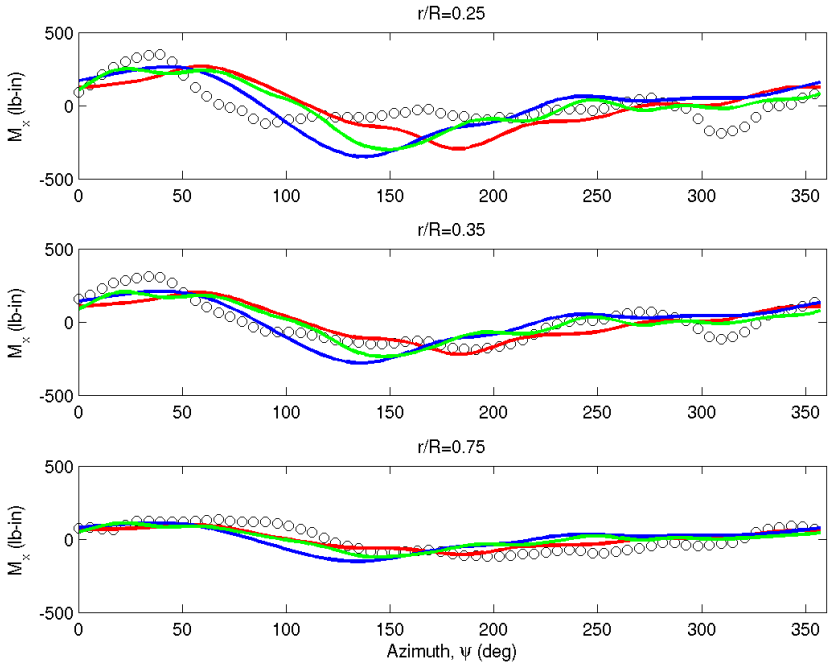

Figure 26: Time histories of the torsion moments at various blade sections for the MDART rotor. $C_T/\sigma = 0.08, \mu = 0.3, \alpha = -9.1^\circ$. Black: experiments, red: UMARC lifting-line analysis, blue: SUmb+UMARC, green: OVERTURNS+UMARC.

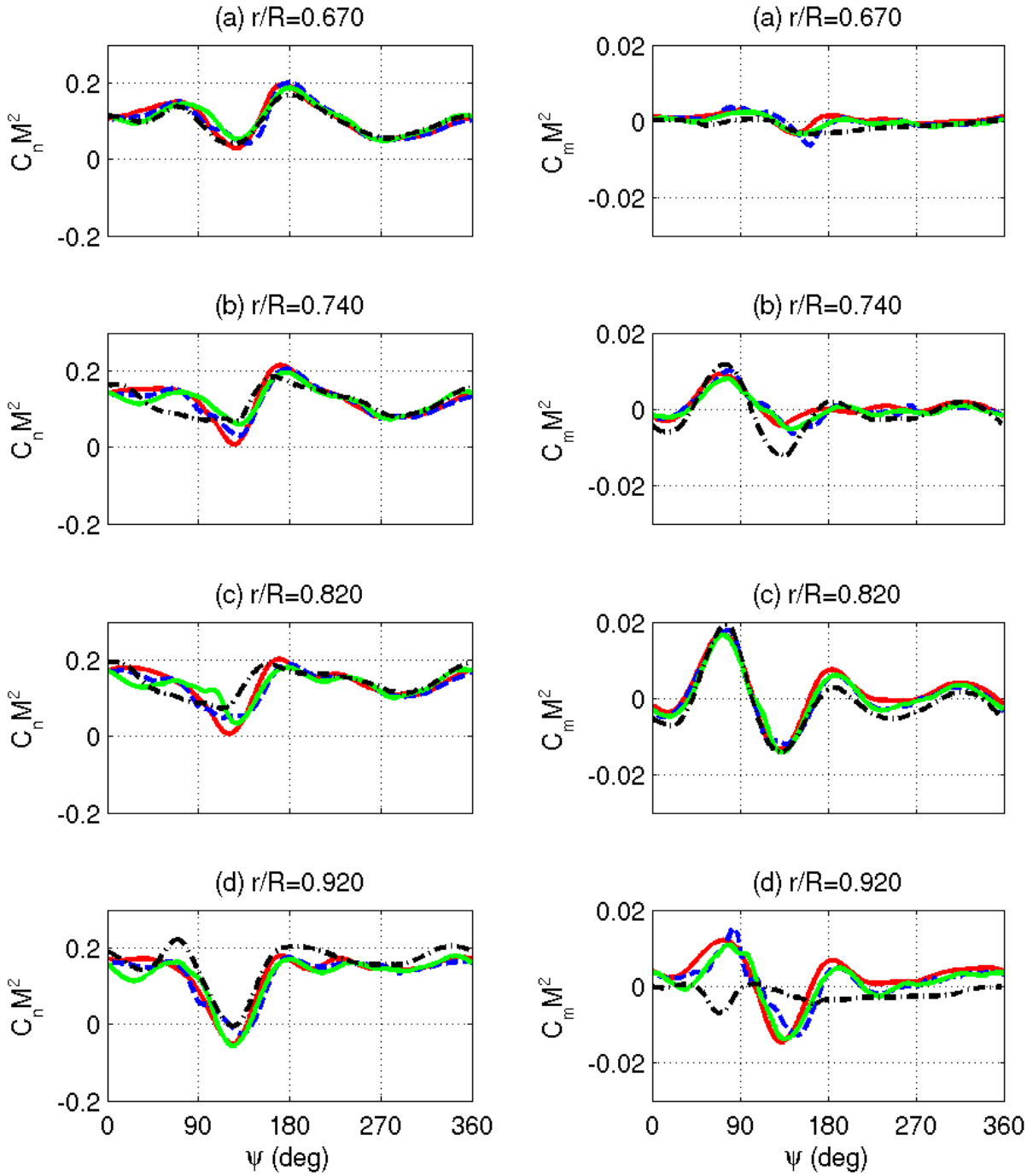

(a) Normal force

(b) Pitching moment

Figure 27: Comparison of the non-dimensional sectional normal force and pitching moment time histories using the wake-coupling approaches for the SMART rotor. solid red: SUmb, dashed blue: UMTURNS, solid green: OVERTURNS, dash-dot black: UMARC lifting-line analysis.

SMART rotor using the wake coupling approaches and with the wake-capturing methodology using OVERTURNS for this flight condition. The trailing edge flap spans from 73.8%R to 91.6%R, the stations shown are located just inboard and outboard of the edges of the trailing edge flap. The loading histories of the two wake coupling approaches are nearly identical in the four radial sections shown, and show no major differences when compared with the OVERTURNS solution. There are slight differences in comparison to the baseline UMARC lifting line analysis. However, the variations in the loading seem to be dominated mostly by the $3/rev$ trailing edge flap excitation. A distinct 3/rev variation is seen in the pitching moment response, especially at the $r = 0.82R$ section. In comparison to the normal force predictions, larger differences are seen between the UMARC lifting-line predictions and the wake coupling analyses in sections outboard of the trailing edge flap region. The solutions from SUmb and the OVERTURNS wake capturing approach are almost identical. CFD predictions seem to indicate the presence of 3-D effects on the blade aerodynamics because of trailing edge flaps which are not seen in the lifting-line predictions.

While the azimuthal variations do not show significant differences between the baseline lifting-line approach and the wake coupling approaches, especially for the normal force distributions, the spanwise variations of the normal forces offer a greater insight into the fundamental differences between the lifting-line, and the CFD-based approaches — see Fig. 28. Unlike the azimuthal distributions, the wake capturing and the wake coupling approaches show slight differences in the normal force predictions. Notice the localized, discontinuous effect of the trailing edge flap along the span. This is because of the 2-D assumptions used to model the blade sections in the UMARC aerodynamic model. The flap aerodynamic effects are accounted only for the sections which contain the flap. It is observed that unlike the UMARC predictions the coupled CFD-CSD predictions do not show the discrete jump at the trailing edge flap end sections. This is because of the full 3-D modeling of the flow field around the flap in the CFD simulations.

4 Summary and Conclusions

A computational framework for coupled aeroelastic analysis of helicopter rotors was developed, tested and successfully validated as part of the HUSH program. The Python-based framework allows the combination of solvers of different disciplines for analysis of different rotorcraft problems in both serial and parallel computing environments. In addition, the framework standardized code interfaces such that multiple codes which have similar functionality can be substituted with ease thereby increasing the spectrum of verification and validation.

The HUSH framework was successfully applied and evaluated for rotorcraft systems that encompass articulated, bearingless and hingless hub configurations. The results obtained from the computations show good agreement with measurements (flight test data as well as controlled experiments) where available. The predictions also showed improved accuracy over the existing comprehensive analysis technology that relied on lifting line based aerodynamics.

The studies demonstrate maturity of the CFD codes and the capability of the coupled fluid-structure simulations to accurately predict the airloads, structural bending moments, the overall performance and acoustics under a wide range of flight conditions. Overall, the CFD/CSD coupled framework is consistently shown to improve the state-of-the-art in simulations of rotorcraft aeromechanics.

- The articulated UH-60A rotor has been analyzed extensively using the coupled CFD-CSD simulation methodology. For the high speed flight condition (C8534), the analysis show good agreement with the measured flight test data for the time histories of the airloads. The phasing of the negative lift peak is resolved at all spanwise stations. Compared to the traditional lifting line analyses, the biggest improvement is observed in the prediction of the vibratory compontents of the rotor airloads.
- For the high thrust flight condition (C9017), the trends in the airloads time histories are captured reasonably well. The phasing of the moment stalls in the retreating side of the rotor disk show good agreement with flight test data. The magnitudes, however, were not captured accurately at all spanwise stations. The fully coupled analysis seems to predict the airloads time-history better than the CFD simulation using the prescribed deformation time histories.
- The predictions of the rotor acoustics show good qualitative agreement with measurements for the DNW rotor. The predictions from the off-surface acoustics methodology is shown to better predict the noise for the DNW rotor,

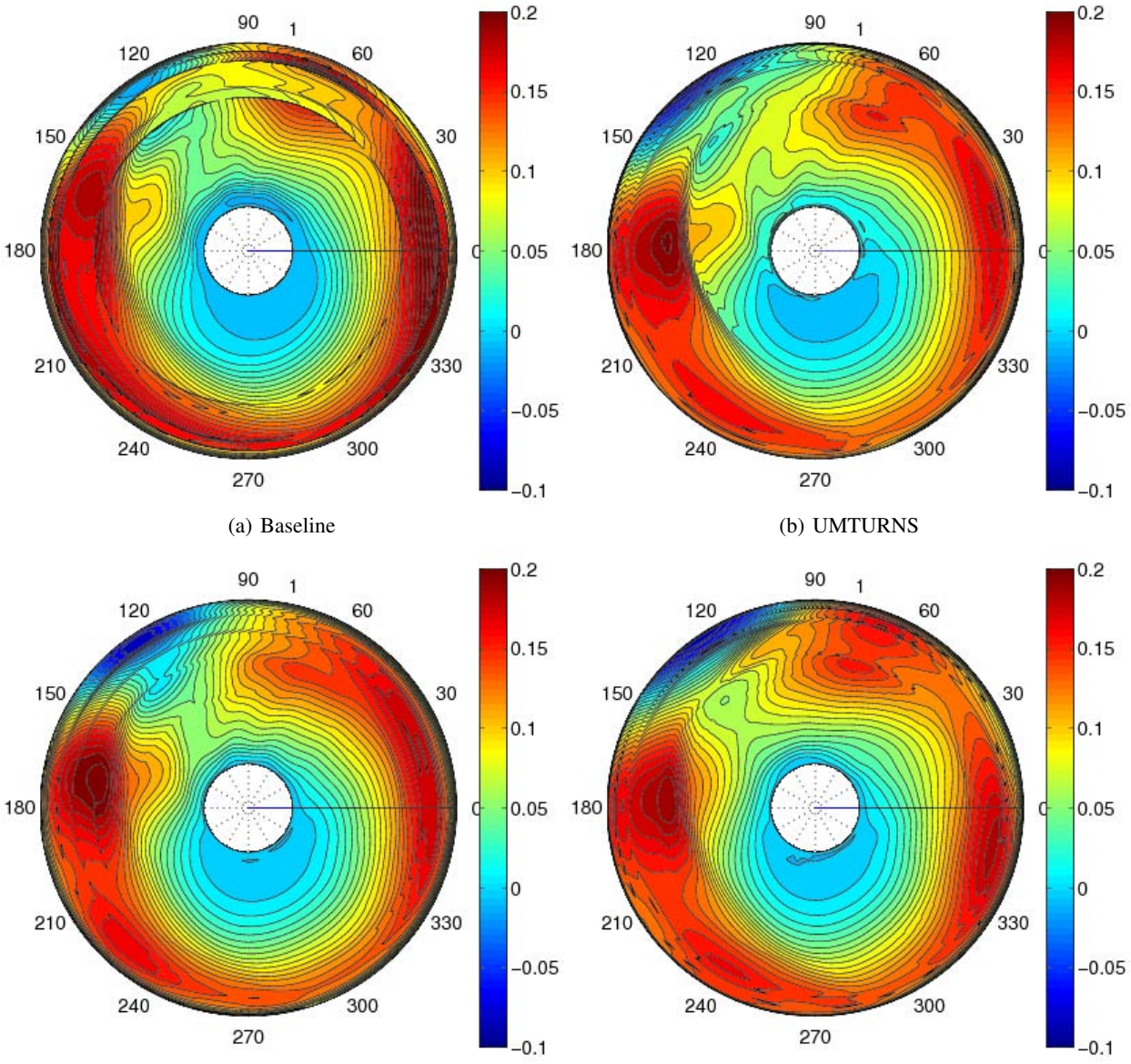

(a) Baseline

(b) UMTURNS

(c) SUmb

(d) OVERTURNS

Figure 28: Contour plots showing the distribution of the normal force (mean-removed) over the rotor disk for the SMART rotor case using four different aerodynamic analysis approaches: (a) baseline UMARC lifting-line analysis, (b) UMTURNS, (c) SUmb, (d) OVERTURNS.

indicating that the contribution from the quadrupole terms is significant at this flight condition and must be included in analysis.

- For the HART-II rotor, the predictions of the BVISPL show excellent agreement compared to measurements. However, the prediction of the low SPL is not as good. This is because the analysis fails to adequately resolve the lower harmonics of the normal lift time-history. Uncertainty of the pitch link stiffness is suspected to be the cause of this inability to predict the lower harmonics.

- For the bearingless MDART rotor, the coupled aeroelastic CFD-CSD analyses show an improvement in the structural flap bending and torsional moment peak-to-peak predictions over the traditional lifting line approach, when compared with the experiments from the MDART rotor. However, there are no significant improvements in the prediction of the chord bending moments. The prediction from the wake capturing methodology show slightly better agreement with the measurements in both the amplitude and phasing of the structural bending moments when compared to the wake coupling approach.

- Analysis of the spanwise and time variations of the blade aerodynamic forces for the SMART rotors with trailing edge flap actuation shows the presence of three-dimensional effects which are not captured by the traditional lifting-line methodology. This is seen as a discontinuous jump in the spanwise airloads across the trailing edge flap end sections in the UMARC lifting line results. The CFD-CSD solutions show a smoother transition across the edges of the trailing edge flap sections. The coupled solution captures the three-dimensional nature of the aerodynamic effects of the trailing edge flap.

Acknowledgements

This work is sponsored by DARPA under ARO Grant #43538GRDP, Helicopter Quieting Program (HQP). Opinions, interpretations, conclusions, and recommendations are those of the authors and are not necessarily endorsed by DARPA or the United States Government. Dr. Dan Newman was the project coordinator, and Dr. Tom Doligalski was the technical monitor. The authors are grateful to Dr. Anubhav Datta and Dr. Inderjit Chopra of the University of Maryland for providing the structural dynamics code (UMARC) and for their valuable insights issues related to structural modeling. Thanks are also due to Dr. Edwin van Der Weide and Dr. Frank Ham, the principal developers of SUmb, CHIMPS and CDP, for close interactions and advice on code integration. We would like to acknowledge the efforts of Dr. Xiaohua Wu for providing the initial implementations of the RANS models in CDP. We are also grateful to Dr. Juan Alonso and Dr. Sanjiva Lele for their role as research advisors and Dr. Parviz Moin and Dr. Frederic Schmitz for providing guidance and leadership to the program. Thanks are also due to our team members Dr. Karthikeyan Duraisamy and Dr. Gaurvav Gopalan for their contributions to the project. We extend our gratitude also to the UH-60A flight test team, HART-II test team, and the Boeing Company for the generously providing the experimental data.

References

[1] Guruswamy, G., "A New Modular Approach for Tightly Coupled Fluid/Structure Analysis," *AIAA Paper 2004-4547,* 10^{th} *AIAA/ISSMO Multidisciplinary Analysis and Optimization Conference*, Albany, NY, August 30–September 1 2004.

[2] Datta, A.and Sitaraman, J., Baeder, J., and Chopra, I., "Analysis Refinements for Prediction of Rotor Vibratory Loads in High-Speed Forward Flight," 60^{th} *Annual Forum of the American Helicopter Society International*, Alexandria, VA, June 2004.

[3] Sitaraman, J., Datta, A., Baeder, J., and Chopra, I., "Coupled CFD/CSD Prediction for Rotor Aerodynamic and Structural Dynamic Loads for Three Critical Flight Conditions," *Proceedings of the* 31^{st} *European Rotorcraft Forum*, Firenze, Italy, 2005.

[4] Sitaraman, J., Datta, A.and Baeder, J. D., and Chopra, I., "Fundamental Understanding and Prediction of Rotor Vibratory Loads in High-Speed Forward Flight," 29^{th} *European Rotorcraft Forum*, September 2003.

[5] Bhagwat, M. J., Ormiston, R. A., Saberi, H. A., and Xin, H., "Application of CFD/CSD Coupling for Analysis of Rotorcraft Airloads and Blade Loads in Maneuvering Flight," *Proceedings of the* 63rd *Annual Forum of the American Helicopter Society*, Virginia Beach, VA, May 1–3 2007.

[6] Datta, A., Nixon, M., and Chopra, I., "Review of Rotorcraft Loads Prediction With the Emergence of Rotorcraft CFD," 31*st European Rotorcraft Forum*, Florence, Italy, September 2005.

[7] Potsdam, M., Yeo, H., and Johnson, W., "Rotor Airloads Prediction Using Loose Aerodynamic/Structural Coupling," *AIAA Journal of Aircraft*, Vol. 43, No. 3, 2006, pp. 732–742.

[8] Silbaugh, B. and Baeder, J., "Coupled CFD/CSD Analysis of a Maneuvering Rotor Using Staggered & Time-Accurate Coupling Schemes," *AHS Specialist's Conference on Aeromechanics*, San Francisco, CA, January, 23–25 2008.

[9] Altmikus, A. R. M., Wagner, S., Beaumier, P., and Servera, G., "A Comparison: Weak versus Strong Modular Coupling for Trimmed Aeroelastic Rotor Simulation," *Proceedings of the* 58th *Annual Forum of the American Helicopter Society International*, Montréal, Canada, June 2002.

[10] Tung, C., Caradonna, F. X., and Johnson, W., "Conservative Full Potential Model for Unsteady Transonic Rotor Flows," *AIAA Journal*, Vol. 25, No. 2, 1987, pp. 193–198.

[11] Ahrem, R., "Multi-Disciplinary Simulations with Coupling Library MpCCI," *Proceedings of Applied Mathematics and Mechanics*, Vol. 1, pp. 39–42.

[12] Sankaran, S., Alonso, J. J., Liou, M., Liu, N., and Davis, R., "A multi-code-coupling interface for combustor/turbomachinery simulations," *AIAA Paper 2001-974, Aerospace Sciences Meeting and Exhibits*, Reno, NV, January 8–11 2001.

[13] Alonso, K., LeGresley, P., and Van Der Weide, E., "CHIMPS: A Framework for High-Fidelity Multi-Disciplinary Optimization," *AIAA Paper 2004-4480,* 10th *AIAA/ISSMO Multi-disciplinary Analysis and Optimization Conference*, Albany, NY, August 30–1 2004.

[14] Wissink, A., Sitaraman, J., Mavriplis, D., Pulliam, T., and Sankaran, V., "A Python-based Infrastructure for Overset CFD with Adaptive Cartesian Grids," *AIAA Paper 2008-0927,* 46th *AIAA Aerospace Sciences Meeting*, Reno, NV, January 2008.

[15] Bousman, W. G. and Kufeld, R. M., "UH-60A Airloads Catalog," Tech. Rep. TM 2005-212827, NASA, August 2005.

[16] Yu, Y. H., Liu, S. R., Landgrebe, A. J., Lorber, P. F., Pollack, M. J., Martin, R. M., and Jordan, D., "Aerodynamic and Acoustic Test of a United Technologies Model Scale Rotor at DNW," *American Helicopter Society* 46*th Annual Forum and Technology Display*, Washington D. C., May 1990.

[17] Lorber, P. F., "Aerodynamic Results of a Pressure-Instrumented Model Rotor Test at the DNW," *Journal of the American Helicopter Society*, Vol. 36, October 1991, pp. 66–76.

[18] Yu, Y. H., Tung, C., van der Wall, B., Pausder, H.-J., Burley, C., Brooks, T., Beaumier, P., Delrieux, Y., Mercker, E., and Pengel, K., "The HART-II Test: Rotor Wakes and Aeroacoustics with Higher-Harmonic Pitch Control (HHC) Inputs - The Joint German/ French/ Dutch/ US Project-," *American Helicopter Society* 58*th Annual Forum and Technology Display*, Montréal, Canada, June 11–13 2002.

[19] Nguyen, K., Lauzon, D., and Anand, V., "Computation of Loads on the McDonnell Douglas Advanced Bearingless Rotor," *American Helicopter Society* 50th *Annual Forum*, Washington D. C., May 11–13 1994.

[20] Nguyen, K., McNulty, M., Anand, V., and Lauzon, D., "Aeroelastic Stability of the McDonnell Douglas Advanced Bearingless Rotor in the $40-\times 80-$Foot Wind Tunnel," Tech. Rep. TM-108831, NASA, June, 1994.

[21] Chopra, I. and Bir, G., "University of Maryland Advanced Rotor Code: UMARC," *American Helicopter Society Aeromechanics Specialists Conference*, San Franscisco, CA, January 1994.

[22] Sitaraman, J., Baeder, J., and Chopra, I., "Validation of UH-60 Rotor Blade Aerodynamic Characteristics Using CFD," 59th *Annual Forum of the American Helicopter Society International*, Phoenix, AZ, May 2003.

[23] van der Weide, E., Kalitzin, G., Schluter, J., and Alonso, J. J., "Unsteady Turbomachinery Computations Using Massively Parallel Platforms," *AIAA Paper 2006-0421,* 44th *AIAA Aerospace Sciences Meeting and Exhibit*, Reno, NV, January 2006.

[24] Bagai, A. and Leishman, J. G., "Rotor Free-Wake Modeling using a Pseudoimplicit Relaxation Algorithm," *AIAA Journal of Aircraft*, Vol. 32, No. 6, Nov.–Dec. 1995, pp. 1276–1285.

[25] Gopalan, G., Sitaraman, J., Baeder, J., and Schmitz, F., "Assessment of Aerodynamic and Aeroacoustic Prediction Methodologies with Application to the HART II Model Rotor," *62nd American Helicopter Society International Forum and Technology Display*, Phoenix, AZ, May 2006.

[26] Duraisamy, K., Sitaraman, J., and Baeder, J., "High Resolution Wake Capturing Methodology for Accurate Simulation of Rotor Aerodynamics," 61th *Annual Forum of the American Helicopter Society*, Dallas, TX, 2005.

[27] Hahn, S., Duraisamy, K., Iaccarino, G., Nagarajan, S., Sitaraman, J., Wu, X., Alonso, J. J., Baeder, J. D., Lele, S. K., Moin, P., and Schmitz, F. H., "Coupled High-Fidelity URANS Simulation for Helicopter Applications," *Annual Research Briefs*, Center for Turbulence Research, Stanford University, 2006, pp. 263–274.

[28] Apte, S. V., Mahesh, K., Moin, P., and Oefelein, J. C., "Large-Eddy Simulation of Swirling Particle-Laden Flows in Coaxial-Jet Combustors," *International Journal of Multiphase Flow*, Vol. 29, No. 8, 2003, pp. 1311–1331.

[29] Saberi, H. A., Khoshlahjeh, M., Ormiston, R. A., and Rutowski, M., "Overview of RCAS and Application to Advanced Rotorcraft Problems," *Proceedings of the American Helicopter Society* 4th *Decennial Specialists' Conference on Aeromechanics*, San Francisco, CA, January 21–23 2004.

[30] Datta, A., Sitaraman, J., Chopra, I., and Baeder, J., "CFD/CSD Prediction of Rotor Vibratory Loads in High-Speed Flight," *AIAA Journal of Aircraft*, Vol. 43, No. 6, 2006, pp. 1698 – 1709.

[31] Weissinger, J., "The Lift Distribution of Swept-Back Wings," Tech. Rep. TM 1120, NACA, 1947.

[32] Leishman, J. G. and Beddoes, T. S., "A Semi-Empirical Model for Dynamic Stall," *Journal of the American Helicopter Society*, Vol. 34, No. 3, July 1989, pp. 3–17.

[33] Yoon, S. and Jameson, A., "Lower-Upper Symmetric-Gauss-Seidel Method for Euler and Navier-Stokes equations," *AIAA Journal*, Vol. 26, 1988.

[34] Pulliam, T., "Time Accuracy and the use of Implicit Methods," Tech. Rep. 1993-3360, American Institute of Aeronautics and Astronautics, 1993.

[35] Spalart, P. R. and Almaras, S. R., "A One Equation Turbulence Model for Aerodynamics Flow," Tech. Rep. 1992-0439, American Institute of Aeronautics and Astronautics, 1992.

[36] Sitaraman, J., Baeder, J., and Iyengar, V., "On the Field Velocity Approach and Geometric Conservation Law for Unsteady Flow Simulations," *AIAA Paper 2003-3835, 16th AIAA Computational Fluid Dynamics Conference*, 2003.

[37] Ffowcs Williams, J. E. and Hawkins, D. L., "Sound Generated by Turbulence and Surfances in Arbitrary Motion," *Philosophical Transactions of the Royal Society, Series A*, Vol. 264, 1969, pp. 321–342.

[38] Brentner, K. and Farassat, F., "Modeling Aerodynamically Generated Sound of Helicopter Rotors," *Progress in Aerospace Sciences*, Vol. 39, No. 2–3, Feb.–Apr. 2004, pp. 83–120.

[39] Brentner, K. S., "Prediction of Helicopter Rotor Discrete Frequency Noise," Tech. Rep. TM-87721, NASA, 1986.

[40] Bousman, W. G., "Putting the Aero Back into Aeroelasticity," 48th *Annual ARO Worshop on Aeroelasticity of Rotorcraft Systems*, Pennsylvania State University, University Park, PA, October 1999.

[41] Lim, J. W. and Strawn, R. C., "Computational Modeling of HART II Blade-Vortex Interaction Loading and Wake System," *Journal of Aircraft*, Vol. 45, No. 3, 2008, pp. 923–933.

[42] Ananthan, S. and Baeder, J., "Prediction and Validation of Loads on Bearingless Rotors Using a Coupled CFD-CSD Methodology," 64*th Annual Forum and Technology Display of the American Helicopter Society International*, Montréal, Cananda, April 29–May 1 2008.

QSAM-*PRIME*

(Quasi-Static Acoustic Mapping –

Plus Rate Induced Maneuvering Effects)

Gaurav Gopalan, Fredric H. Schmitz, Cal Sargent

University of Maryland

Special thanks to:

Ben Wel-Chong Sim

University of Santa Cruz

(US Army Aeroflightdynamics Laboratory)

Table of Contents

1. Introduction

The accurate prediction of helicopter noise radiation during nominal as well as specialized flight operations is essential for both community annoyance assessment for land use planning studies as well as for planning military operations that minimize acoustic detection and maximize troop safety. Nominal helicopter flight includes cruise in level flight, steady longitudinal descents at a constant flight path angle and steady bank turns. Moderately accelerating and decelerating flight segments are also part of the nominal helicopter flight operation envelope. Transitions into and out of these nominal flight states are often short compared to these nominal flight operations, but can be important in terms of control requirements and noise radiation. It may take only one unfortunate control input to cause additional noise radiation that results in the detection of the helicopter. These transition segments include changes in flight path angle, changes in accelerations and changes in bank angles, or any combinations of these maneuvers. More specialized or extreme maneuvers like quick stops, quick rolls or pull-ups or any combinations of these operations are also an integral part of a military helicopter pilot's operational envelope. A useful predictive acoustic tool must model the entire helicopter flight envelope accurately.

One approach to acoustic prediction for annoyance or detection studies as applied to steady state flight is the so-called direct acoustic mapping method. This involves the measurement of acoustic data during steady-state helicopter flight operations. The acoustic and flight data, along with related weather and terrain information, is then reduced to obtain a radiation sphere or map around the helicopter during a specified

steady state flight condition. These spheres are then stored in a database, which is invoked to predict the noise radiated during a specific helicopter operation within the envelope of the test matrix used to develop the spheres.

Such a direct acoustic mapping approach has been implemented in NASA Langley's Rotor Noise Model[1] (RNM) developed by Wyle Labs. The sphere development is conducted using a subroutine called the Acoustic Repropagation Technique (ART). The Rotor Noise Model (RNM) is essentially a basic sphere selection, basic sphere interpolation and an advanced state-of-the-art acoustic propagation model that predicts the noise radiated by a helicopter performing a specified steady state flight operation. The details of the algorithms and implementation of the current version of RNM and ART can be found in the users manual supplied by Wyle Labs.

The Rotor Noise Model has some very significant advantages over state-of-the-art first principles prediction methods. Because it relies on measured data the model, if accurately and correctly implemented, can potentially capture the actual physics of both noise generation and propagation.

Currently RNM develops acoustic hemispheres from ground-based acoustic data that was gathered during straight, steady-state flight. Noise estimation is limited to steady state longitudinal flight conditions only. Transitional flight states are not modeled. The effect of maneuvers and transients, turns, wind and other special flight operations and

atmospheric conditions, which are known to potentially have a significant impact on the radiated noise, are not accounted for.

The Quasi-Static Acoustic Mapping[2, 3] (Q-SAM) method is a principle by which the direct mapping approach can be extended to include some maneuvering flight conditions. Currently applied to main rotor Blade-Vortex Interaction (BVI) noise, this principle states that the noise radiated by a helicopter during a moderate maneuver is equivalent to that radiated by the same helicopter at a different steady state flight condition. This powerful source noise prediction principle has been successfully used to predict the BVI noise radiation characteristics of a slowly accelerating / decelerating (< 0.1 g) helicopter in straight-line constant flight path angle flight, and has been validated in specially conducted flight tests[4, 5]. It has also been extended to include the effect of steady wind[6, 7]. More recently the effect of steady banked turns, with and without steady winds, have also been incorporated[8].

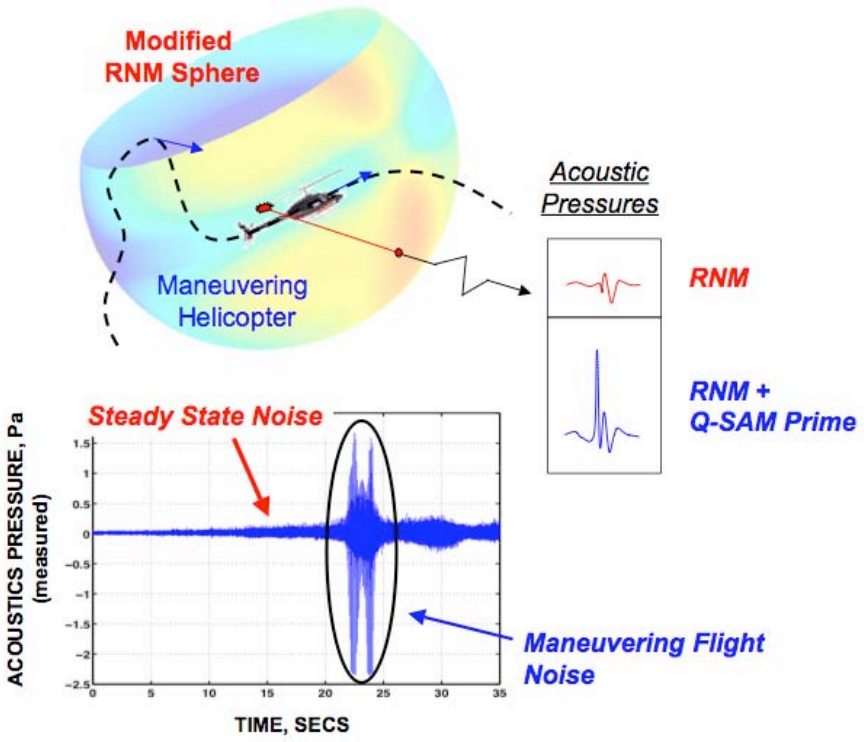

Figure 1: Motivation and Approach for the QSAM-PRIME Project.

Recent flight tests have demonstrated the importance of including the effect of transient maneuvers in the prediction process. In particular, a quick pull up maneuver on a heavily loaded two bladed helicopter resulted in unexpectedly high increases in noise levels directly ahead of the helicopter. This new observation reiterates the essential significance of including maneuvering and transient flight in acoustic prediction models for annoyance and detection studies.

The extension of RNM to include both Q-SAM as well as transient maneuver effects is essential to broadening its applicability and taking the next step towards developing an accurate physics-based tool for quiet helicopter flight planning.

Project Objectives

The objectives of the current project are threefold:

1. Develop and Implement a Methodology to Incorporate the **Acoustic Effects of Maneuvering and Turning Flight** into RNM (Q-SAM)

2. Incorporate **Empirical Acoustic Corrections** associated with Maneuvers based on Recent Flight Test Data (Q-SAM Prime)

3. Employ the Q-SAM Prime approach in RNM to model the radiated noise during a typical helicopter sortie/scenario and compare the acoustic results to the steady-state RNM modeling.

2. Technical Approach

The inputs provided for this project were:

1. MD-902 noise radiation semi-sphere database obtained using the ART / RNM process
2. Detailed information about the flight sortie/scenario to be modeled

The technical approach used is summarized below and represented schematically in Figure 2:

1. **Preprocess Trajectory** to incorporate a sequence of realistic Maneuvering segments
2. Use fundamental flight mechanics to determine **Helicopter Performance States** and **Governing Acoustic Parameters**
3. Use **Quasi-Static Acoustic Mapping** to select acoustic spheres for Moderate Maneuvers
4. Use **Empirical Acoustic Penalties** to modify RNM Radiation Spheres for Transient or Extreme Maneuvers

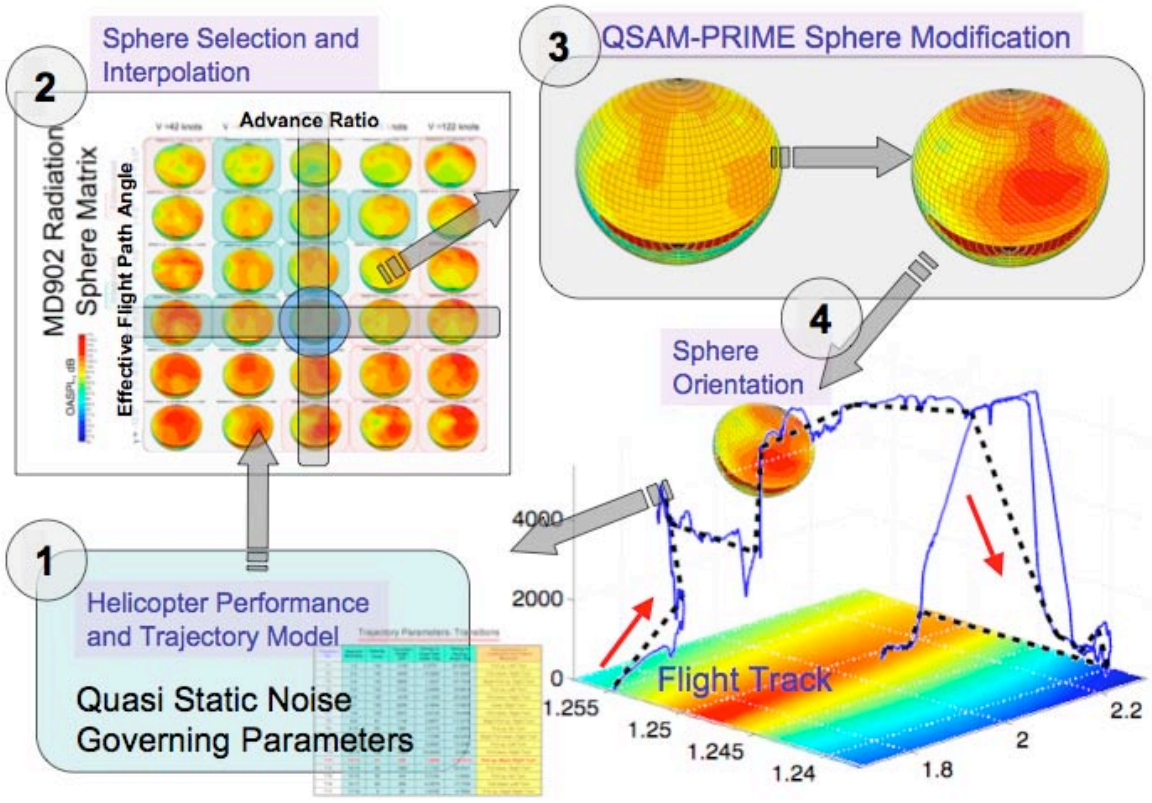

Figure 2: Schematic showing the implementation of QSAM-Prime in RNM.

The flight sortie consisted of a sequence of trajectory waypoints. At each waypoint the helicopter position, velocity and Euler angles (helicopter fuselage angle of attack in place of pitch attitude) were specified. From this information time histories of the velocity, flight path angle, heading angle and Euler angles was calculated by making the following assumptions:

1. The flight segment between two consecutive way-points is a straight line with a constant heading and flight path angle
2. The pilot accelerates or decelerates to the final velocity of the segment at a constant acceleration or deceleration of 0.1 g at the beginning of the segment.

When the target velocity for the segment is reached the helicopter flies at a constant velocity and flight path angle to the endpoint of the segment.

The flight sortie included some very significant changes in heading angle but realistic turns were not modeled explicitly. The next step in the trajectory preprocessing was to include realistic turning flight segments at constant velocity and flight path angle. At each inter-segment transition associated with a change in heading angle greater than 10° a coordinated 45° bank turn was assumed and modeled in the trajectory.

The trajectory now consisted of three different types of constant flight path angle segments:

1. Constant Velocity Longitudinal Flight
2. Steady Turns
3. Accelerating or Decelerating Flight

The flight trajectory was then refined to include realistic transitions between successive segments[9]. Transitions involved the following types of maneuvers:

1. Changes in acceleration along the flight path at a constant fight path angle and heading angle,
2. Changes in flight path angle at a constant flight velocity and heading angle
3. Changes in bank angle at a constant velocity and flight path angle.

4. A combined change in flight path angle and bank angle at a constant velocity at the end of turning flight maneuvers. This combination maneuver was modeled as a sequence of a Type 3 transition (change in bank angle) followed by a Type 2 transition (change in flight path angle).

These inter-segment transitions were achieved through transition maneuvers. For the transition of Type 1 (change in acceleration maneuver), a constant rate of change of acceleration or deceleration was assumed at a rate of 0.1 g per sec. This resulted in a pitch rate of 6° per sec. For transition of Type 2 (change in flight path angle maneuver), a maximum load factor limit of 1.5 was assumed. This defined a maximum rate of change of flight path angle at any flight velocity. Reduction in flight path angle is not currently penalized and a nominal minimum load factor of 0.5 was assumed. Transitions of Type 3 (change in bank angle) were assumed to occur at the beginning (roll-in) and end (roll-out) of steady turns. A constant roll rate of 22.5° per sec was assumed for both the roll-in and roll-out maneuvers. The change in heading that occurred during these transient roll maneuvers was subtracted out from the total change in heading occurring during the steady turn segment for physical consistency. Figure 3 shows a typical change in heading maneuver with three distinct phases 1) Roll in or increase in bank angle, 2) steady coordinated turn or constant bank angle maneuver and 3) Roll out or decrease in bank angle maneuver.

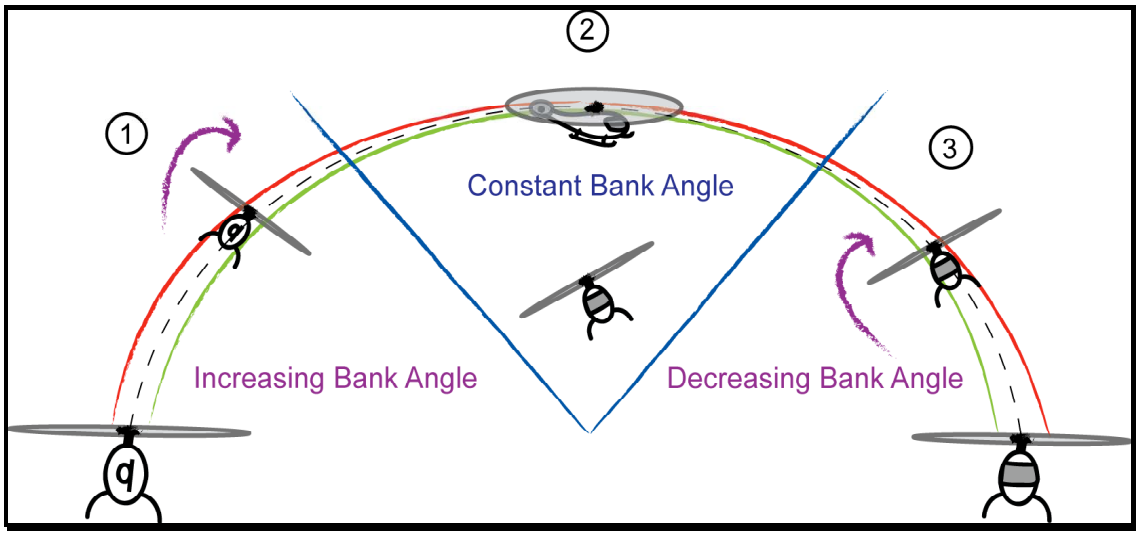

Figure 3: A generic change in heading maneuver showing the three distinct phases: 1) roll in maneuver, 2) steady turn maneuver and 3) roll out maneuver.

The trajectory development procedure of identifying all segment and inter-segment transitions was conducted for the entire trajectory using a MATLB based helicopter flight performance and trajectory preprocessor. Trajectory waypoint information was then recalculated at 1 second intervals along the entire trajectory. In portions of the trajectory where the helicopter underwent a quick transient maneuver, the timestepping was refined down to 0.5 or 0.2 seconds. Trajectory points lying within a steady state longitudinal segment (constant flight velocity and flight path angle) were discarded when inputting the trajectory into RNM, because they can be calculated internally within the code. A TIMESTEP size of 2 seconds was specified – which was used for these internal calculations in the RNM code along a steady state longitudinal flight segment.

A detailed treatment of the trajectory, including constant acceleration / deceleration segments as well as constant speed segments, inter - segment transitions including all the

change in flight path angle, change in acceleration and change in heading maneuvers have been described in the next section. These specifications are then used to select and develop the appropriate radiation semi-sphere using the sphere database and applied along the trajectory. The development of the acoustic sphere database is described in Appendix A. Sample spheres have been shown and some technical issues have been isolated. Once the trajectory had been preprocessed a sphere file name was assigned to each trajectory waypoint. The NCSPEC option was used in RNM to circumvent its internal sphere selection process and to mandate the use of the radiation sphere specified by the input file.

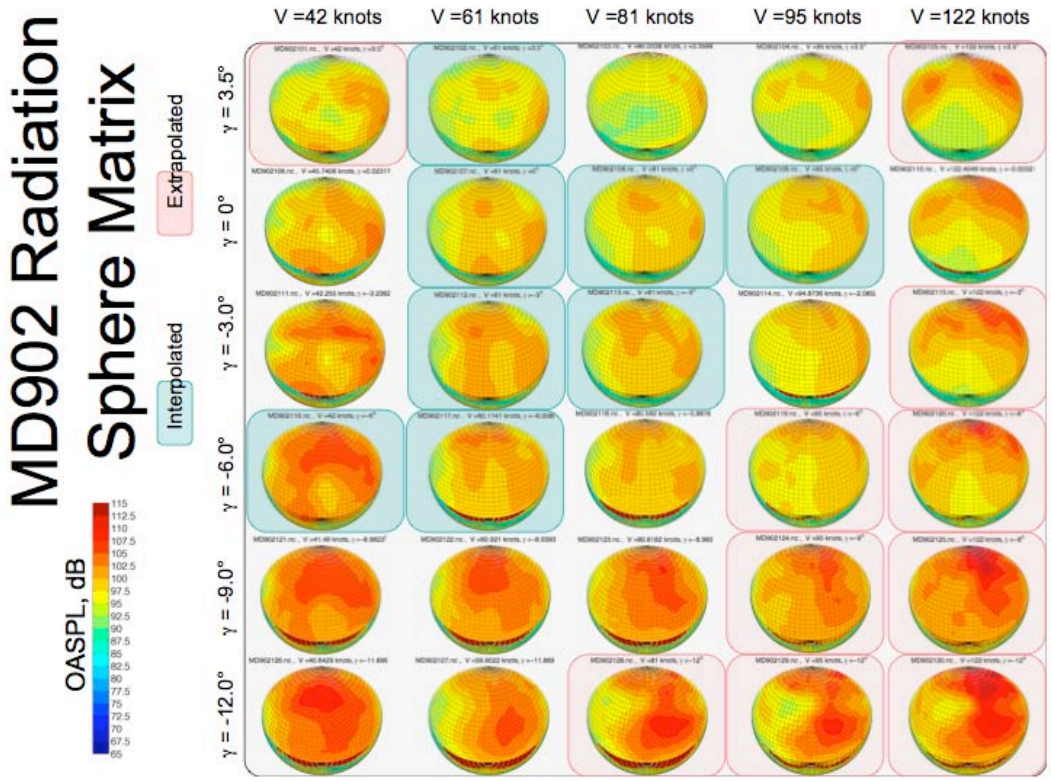

Figure 4: RNM Radiation spheres stored in a rectangular Velocity-Flight Path Angle grid.

The sphere selection was then conducted along the trajectory based on Q-SAM principles. Rather than using the input sphere database as is, it was first preprocessed to a rectangular Velocity versus Flight Path Angle grid using appropriate interpolation and extrapolation techniques (see Fig. 4 above).

The radiation sphere corresponding to each trajectory point was developed using a two step predictor-corrector type approach. A sphere was first selected from the database using Q-SAM principles. The effect of an acceleration or deceleration parallel to the flight path was modeled using the concept of effective flight path angle. Essentially, an acceleration or deceleration along the flight path is, in terms of main rotor performance, equivalent to a change in the quasi-static flight path angle of the helicopter at the same flight velocity. For instance an acceleration of 0.1 g along the flight path effectively increases the flight path angle by 5.7 deg in terms of the main rotor acoustic state. Deceleration has the opposite effect and is equivalent to an increase in descent angle. This modified flight path angle was calculated and used for the sphere selection process. Once an effective sphere was selected at each trajectory location, an empirical maneuver correction was applied to the sphere. This correction factor was applied as a uniform delta-dB over all narrow bands and over the entire radiation sphere, because of insufficient data / knowledge about the details of transient maneuvering flight noise radiation.

The empirical correction factors used to modified effective maneuvering flight acoustic spheres to represent the effect of transient maneuvers were determined using linear curve

fits to acoustic flight data. These factors are summarized in Table 1. The following factors were applied to the various maneuvering flight segments:

Change in Heading Angle:

1. Roll In Maneuver:
   - 22.5 deg per sec
   - Left Turn: ΔdB = 4 dB
   - Right Turn: ΔdB = 6 dB
2. Steady Coordinated Turn:
   - 45 deg Bank Angle
   - Left Turn: ΔdB = 3 dB
   - Right Turn: ΔdB = 3 dB
3. Roll Out Maneuver:
   - 22.5 deg per sec
   - Left Turn: ΔdB = 6 dB
   - Right Turn: ΔdB = 4 dB

Change in Acceleration:

4. Positive Pitch Rate Maneuver:
   - 11.4 deg per sec
   - ΔdB = 2.5 dB
5. Negative Pitch Rate Maneuver:
   - -11.4 deg per sec
   - ΔdB = 2.5 dB

Change in Flight Path Angle:

6. Collective Up Maneuver (Increase in Flight Path Angle):
   - Maximum Load Factor of 1.5
   - ΔdB = 6 dB per doubling of Thrust
7. Collective Down Maneuver (Decrease in Flight Path Angle):
   - Minimum Load Factor of 0.5
   - ΔdB = 0

	Metric	Pos. Pitch Rate (Up)	Pos. Roll Rate (Right)	Pos. Roll Rate (Left)	Collective Adjustment
Bell 206B	ΔOASPL (in 22.5 degrees)	6 dB	4dB	3 dB	1 dB/.5g
	ΔOASPL/deg./sec	.27 dB/deg./sec	.18 dB/deg./sec	.13 dB/deg./sec	
	Δ dBA (in 22.5 degrees)	13 dB	8 dB	0 dB	7 dBA/.5g
	dBA/deg./sec	.58 dBA/deg./sec	.36 dBA/deg./sec	.0 dBA/deg./sec	
Bell 407	Δ OASPL (in 22.5 degrees)	5 dB	6 dB	4 dB	
	OASPL/deg./sec	.22 dB/deg./sec	.27 dB/deg./sec	.18 dB/deg./sec	
	Δ dBA (in 22.5 degrees)	6.4 dB	6.2 dB	3 dB	
	dBA/deg./sec	.28 dBA/deg./sec	.28 dBA/deg./sec	.13 dBA/deg./sec	

Table 1: Empirical acoustic corrections based on curve fits to flight test data.

3. Results and Discussion

The mission profile provided consisted of ground based X, Y, Z coordinates, Velocity profile as well as the sequence of fuselage heading angle, fuselage angle of attack, and fuselage roll angle. The original trajectory provided has been plotted in Fig. 5 below. Also marked are some key control points along the trajectory, including the beginning and end locations as well as major changes in heading and flight path angle.

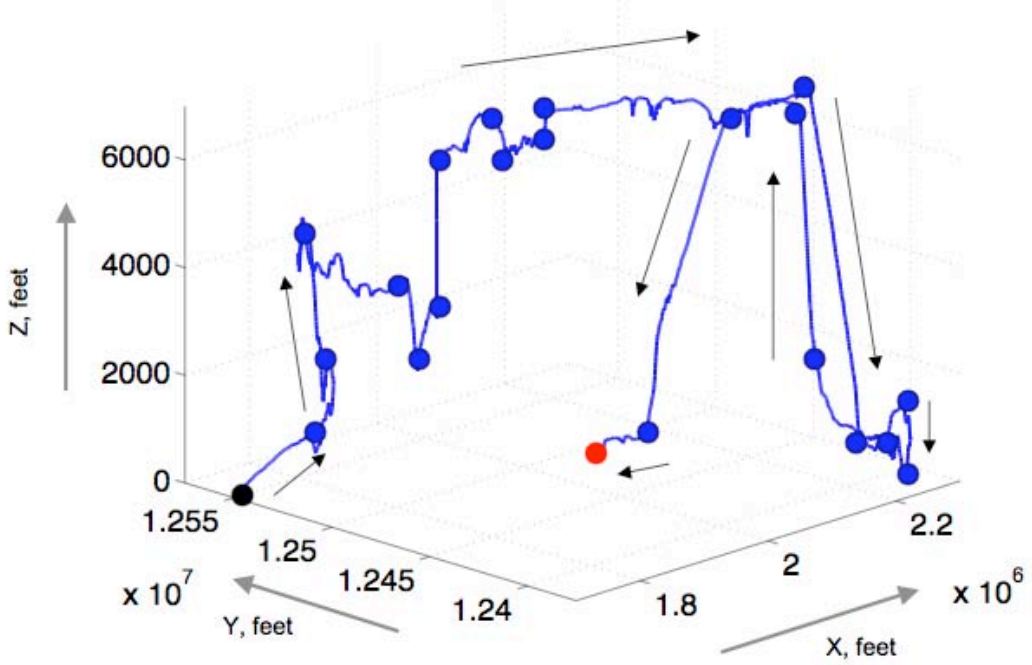

Figure 5: The ground referenced trajectory of the mission profile.

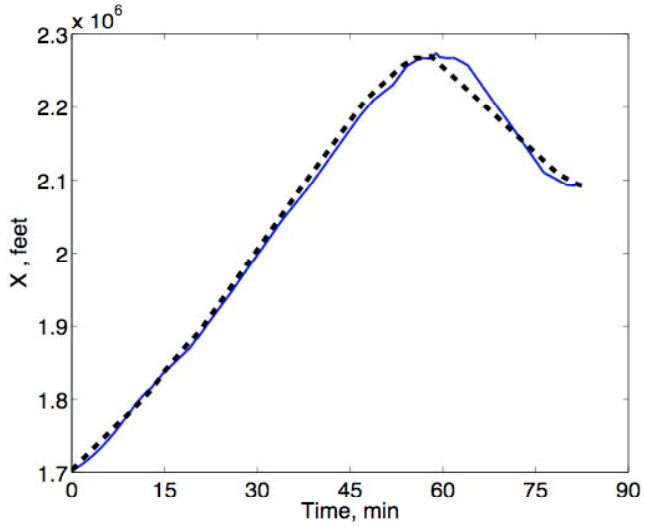

Figure 6: The ground referenced X-coordinate of the mission profile as a function of time. Original trajectory in solid blue and reduced trajectory in dashed black line.

The position and velocity were used together to obtain the time coordinate along the trajectory by assuming constant acceleration segments and invoking Newton's kinematic equations on motion. Figures 6, 7 and 8 show the ground based X, Y and Z coordinates of the trajectory as a function of the time in minutes. It was seen that the trajectory lasts for nearly 90 minutes according to this preliminary time calculation. The initial trajectory provided is shown in the blue solid line while a reduced simplified trajectory that was finally used for the project and also provided by NASA Langley is shown in dashed line. The original trajectory locations provided consisted of nearly 5000 location specifications and included very high frequency, unrealistic fluctuations or "wiggles" in the Z coordinate (see Fig. 8). These high frequency fluctations were smoothed out and a manual low pass filtering was used by NASA Langley to provide a reduced trajectory of points.

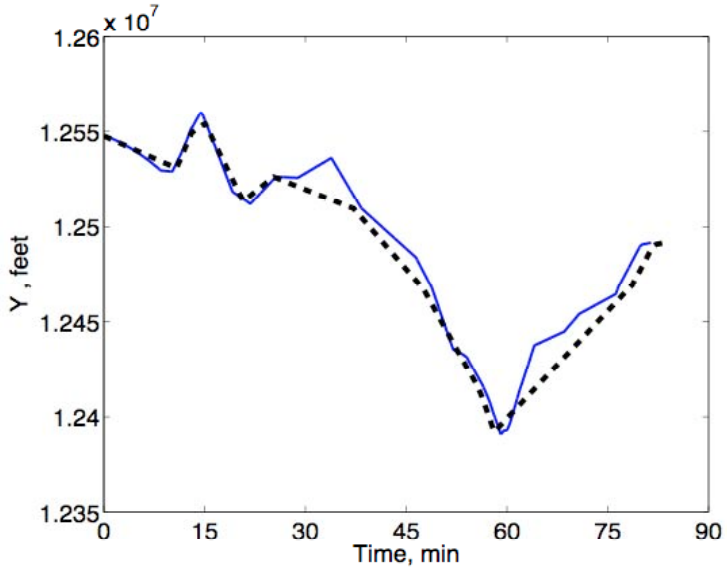

Figure 7: The ground referenced Y-coordinate of the mission profile as a function of time. Original trajectory in solid blue and reduced trajectory in dashed black line.

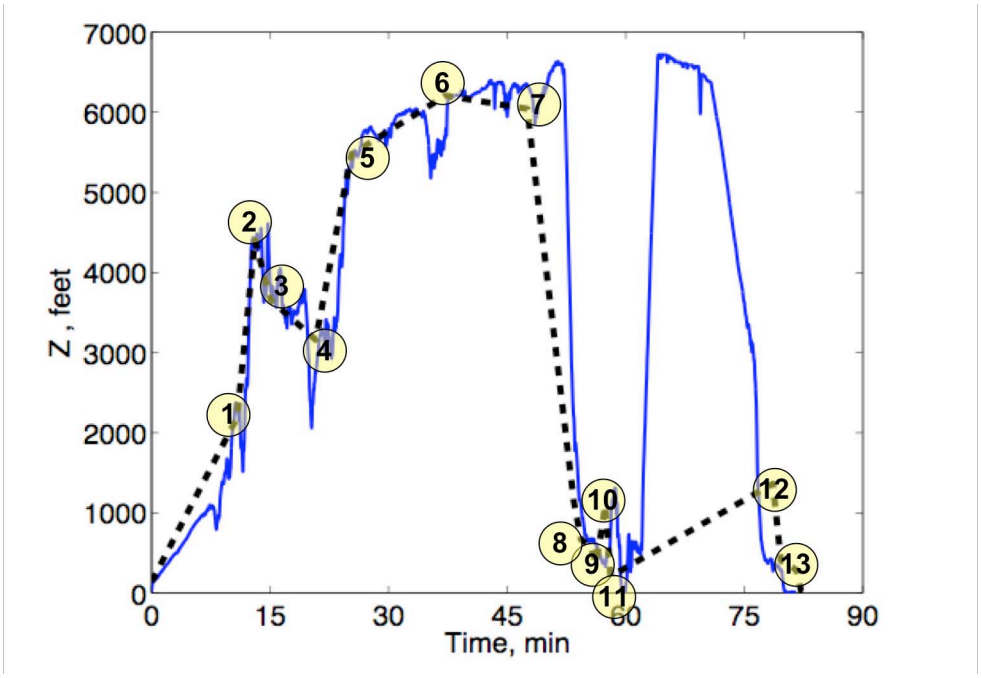

Figure 8: The ground referenced Z-coordinate of the mission profile as a function of time. Encircled numbers indicate locations with major changes of flight path angle. Original trajectory in solid blue and reduced trajectory in dashed black line.

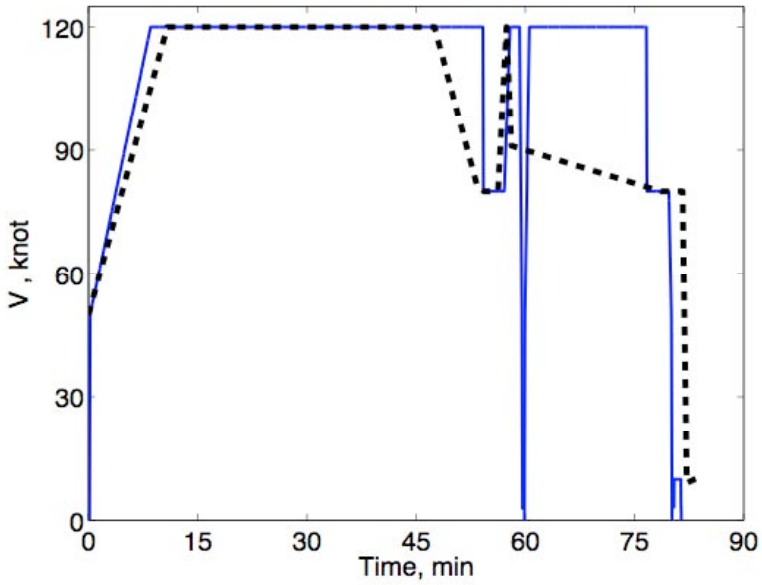

Figure 9: The flight velocity along the mission profile as a function of time. Original trajectory in solid blue and reduced trajectory in dashed black line.

The time history of the velocity profile along the trajectory is shown in Fig. 9. As before the original specification is shown in solid line and the reduced trajectory specification in dashed line. The original trajectory consisted of some step changes in velocity; these were considered unrealistic in practice and were modified in the reduced trajectory to somewhat more gradual changes. The velocity profile consists of an acceleration from 50 knots to 120 knots, then a constant speed of 120 knots for about 35 minutes. This is followed by a succession of deceleration and acceleration maneuvers and finally a deceleration to a landing. At around 60 minutes, there is a sharp hairpin turn in the trajectory and in corresponds to a landing and a turning back of the helicopter (as can be seen in Figs. 5 through 8). This feature was smoothed out in the velocity profile and was not considered critical to modeling the acoustics of the helicopter in flight.

The trajectory was initially assumed to consist of straight-line segments with a constant acceleration or deceleration along the flight path. The acceleration profile along the trajectory was calculated next based on the uniform acceleration assumption and has been shown in Fig. 10. Most of the acceleration / deceleration levels are very low, with a maximum deceleration of 0.1g towards the end of the trajectory.

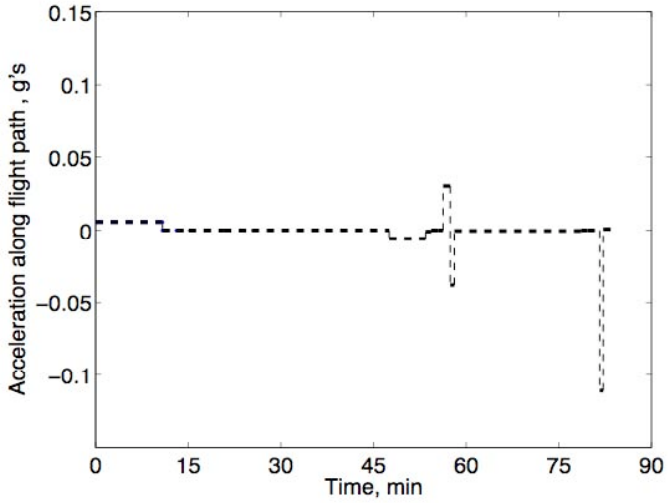

Figure 10: Acceleration time history along the mission profile for the reduced trajectory.

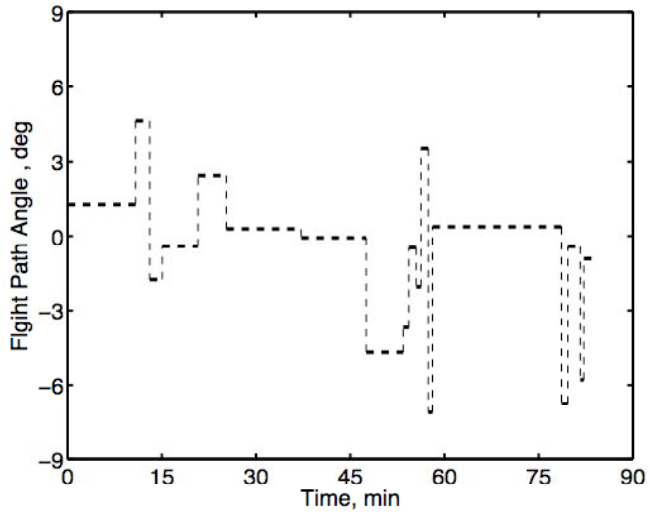

Figure 11: Flight path angle time history along the mission profile for the reduced trajectory.

The flight path angle profile was also calculated for the reduced trajectory for each segment and has been shown as a function of time in Fig. 11. A list of the 18 segments calculated based on the above mentioned segmentation method has been summarized in Table 2 below. The table specifies the flight path angle, acceleration along the flight path, heading angle, time period, initial velocity, segment length and change in height of the helicopter along each segment.

Segment No.	Flight Path Angle, Degrees	Acceleration Along Flight Path, g's	Heading Angle, Degrees	Time Period, Minutes	Initial Velocity, Knots	Segment Length, feet	Change in Height, feet
S1	1.2629	0.0057	-10.3713	10.8264	50	9319	2054
S2	4.6336	0	42.6921	2.2542	120	2739	2213
S3	-1.7585	0	11.4429	2.0031	120	2434	-747
S4	-0.4148	0	-36.2815	5.6715	120	6892	-499
S5	2.4118	0	13.5796	4.5290	120	5504	2316
S6	0.2893	0	-6.6761	11.8973	120	14458	730
S7	-0.0751	0	-19.5585	10.3543	120	12583	-165
S8	-4.6876	-0.0058	-39.0071	5.8877	120	5992	-4897
S9	-3.6899	-0.0010	-50.0846	0.9111	81	743	-478
S10	-0.4725	0	-50.3491	1.1825	80	958	-79
S11	-2.0491	0	-92.5893	0.7491	80	607	-217
S12	3.5344	0.0304	-79.3812	1.1581	80	1173	723
S13	-7.1119	-0.0380	-86.3709	0.6706	120	716	-887
S14	0.3727	-0.0005	154.2876	20.5416	91	17786	1157
S15	-6.7430	0	124.3444	1.0082	80	817	-959
S16	-0.4246	0	124.4293	1.9822	80	1606	-119
S17	-5.7925	-0.1109	142.1629	0.5629	80	254	-256
S18	-0.9199	0.0007	137.3973	1.2302	9	118	-19

Table 2: Initial segment divisions of the reduced trajectory.

It can be seen from the table that many of the accelerating / decelerating segments are characterized by extremely slow changes in velocity, but change in velocity itself is very significant. For instance the first segment consists of a very low acceleration level of 0.06 g over 11 minutes resulting in a change of flight velocity from 50 knots to 120 knots. This was considered unrealistic in practice where a pilot would prefer to speed up or slow

down to a target velocity and continue at a constant speed. Therefore segments undergoing a change in velocity were further divided into two segments with the same flight path angle. The first segment consisted to accelerating or decelerating at 0.1 g to the target velocity and the second segment consisted of a constant speed trajectory at the target velocity.

The trajectory was thus divided into constant acceleration / deceleration segments as well as constant speed segments all characterized by a constant flight path angle and heading angle. Changes in acceleration, flight path angle and / or heading angle occurred at segment boundaries through inter-segment transition maneuvers. The changes in flight path angle and heading angle occurring at the segment boundaries are summarized in Table 3 below.

Transition No.	Segment Boundary	Velocity, knots	Transition Height, feet	Change in Flight Path Angle, Deg	Change in Heading Angle, Deg	Characterization of Longitudinal and Lateral Maneuver
T1	1-2	120	2193	3.3707	53.0634	Pull up, Left Turn
T2	2-3	120	4406	-6.3922	-31.2491	Pull down, Right Turn
T3	3-4	120	3659	1.3437	-47.7244	Slight Pull up, Right Turn
T4	4-5	120	3160	2.8266	49.8610	Pull up, Left Turn
T5	5-6	120	5476	-2.1225	-20.2557	Pull down, Right Turn
T6	6-7	120	6206	-0.3644	-12.8823	Level, Right Turn
T7	7-8	120	6041	-4.6124	-19.4486	Pull down, Right Turn
T8	8-9	81	1144	0.9977	-11.0775	Slight Pull up, Right Turn
T9	9-10	80	666	3.2174	-0.2645	Pull up, No Turn
T10	10-11	80	587	-1.5766	-42.2402	Slight Pull down, Right Turn
T11	11-12	80	370	5.5835	13.2080	Pull up, Left Turn
T12	12-13	120	1093	-10.6463	-6.9896	Pull down, Right Turn
T13	**13-14**	**91**	**206**	**7.4846**	**-119.3415**	**Pull up, Major Right Turn**
T14	14-15	80	1363	-7.1157	-29.9431	Pull down, Right Turn
T15	15-16	80	404	6.3184	0.0849	Pull up, No Turn
T16	16-17	80	285	-5.3679	17.7335	Pull down, Left Turn
T17	17-18	9	29	4.8726	-4.7655	Pull up, Slight Right Turn

Table 3: Inter-segment transitions for the reduced trajectory.

The segment sequence, including transitions are specified in the list below (the segment and transition numbers in brackets correspond to the specification in Table 2 and 3):

1. Accelerate from 50 to 120 knots at 0.1 g (S1)
2. Constant Speed at 120 knots (S1)
3. Change heading by 53 deg to the left (T1)
4. Increase Flight Path Angle by 3.4 deg (T1)
5. Constant Speed at 120 knots (S2)
6. Change heading by 31 deg to the right (T2)
7. Reduce Flight Path Angle by 6.4 deg (T2)
8. Constant Speed at 120 knots (S3)
9. Change heading by 48 deg to the right (T3)
10. Increase Flight Path Angle by 1.3 deg (T3)
11. Constant Speed at 120 knots (S4)
12. Change heading by 50 deg to the right (T4)
13. Increase Flight Path Angle by 2.8 deg (T4)
14. Constant Speed at 120 knots (S5)
15. Change heading by 20 deg to the right (T5)
16. Reduce Flight Path Angle by 2.1 deg (T5)
17. Constant Speed at 120 knots (S6)
18. Change heading by 13 deg to the right (T6)
19. Constant Speed at 120 knots (S7)
20. Change heading by 19 deg to the right (T7)
21. Reduce Flight Path Angle by 4.6 deg (T7)
22. Decelerate from 120 to 80 knots at 0.1g (S8)
23. Constant Speed at 80 knots (S8)
24. Change heading by 11 deg to the right (T8)
25. Increase Flight Path Angle by 1.0 deg (T8)
26. Constant Speed at 80 knots (S9)

27. Increase Flight Path Angle by 3.2 deg (T9)
28. Constant Speed at 80 knots (S10)
29. Change heading by 42 deg to the right (T10)
30. Reduce Flight Path Angle by 1.6 deg (T10)
31. Constant Speed at 80 knots (S11)
32. Change heading by 13 deg to the left (T11)
33. Increase Flight Path Angle by 5.6 deg (T11)
34. Accelerate at 0.1g from 80 to 120 knots (S12)
35. Constant Speed at 120 knots (S12)
36. Change heading by 7 deg to the right (T12)
37. Reduce Flight Path Angle by 10.6 deg (T12)
38. Decelerate at 0.1g from 120 to 91 knots (S13)
39. Constant Speed at 91 knots (S13)
40. Change heading by 119 deg to the right (T13)
41. Increase Flight Path Angle by 7.5 deg (T13)
42. Decelerate from 91 to 80 knots at 0.1g (S14)
43. Constant Speed at 80 knots (S14)
44. Change heading by 30 deg to the right (T14)
45. Reduce Flight Path Angle by 7.1 deg (T14)
46. Constant Speed at 80 knots (S15)
47. Increase Flight Path Angle by 6.3 deg (T15)
48. Constant Speed at 80 knots (S16)
49. Change heading by 18 deg to the left (T16)
50. Reduce Flight Path Angle by 5.4 deg (T16)
51. Constant Speed at 80 knots (S17)
52. Decelerate from 80 to 10 knots at 0.2g (S17)
53. Change heading by 5 deg to the right (T17)
54. Increase Flight Path Angle by 4.9 deg (T17)
55. Constant Speed at 10 knots (S18)

A detailed deconstruction of the trajectory has been presented with special focus on the maneuvering flight segments and the inter-segment transitions in Appendix B. The final input file used to run RNM using the NCSPEC option is shown in Appendix C for reference.

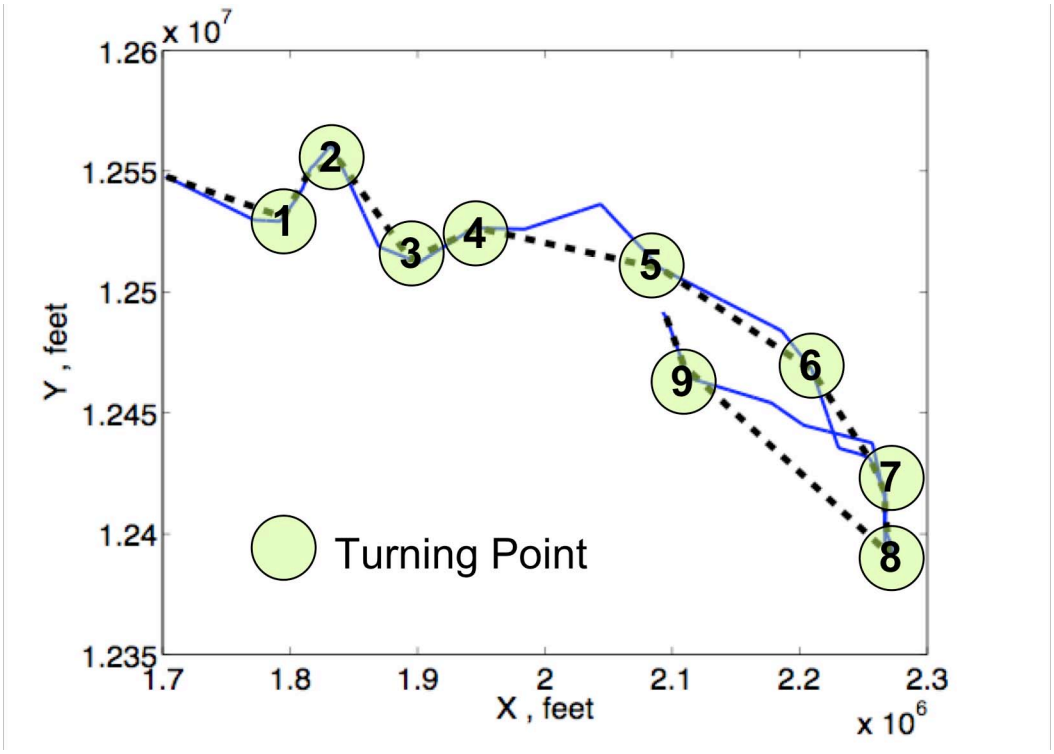

Figure 12: The ground referenced X,Y-coordinates of the mission indicating the major turning point locations. Original trajectory in solid blue and reduced trajectory in dashed black line.

Changes in heading, or turning points along the trajectory were initially specified as instantaneous in the original as well as the reduced trajectory. However they were modeled more realistically in QSAM as a turning flight maneuver consisting of three distinct phases, roll in, steady turn and roll out (as described in the previous section). The top view of the trajectory is shown in Fig. 12 with the major turning points encircled and numbered.

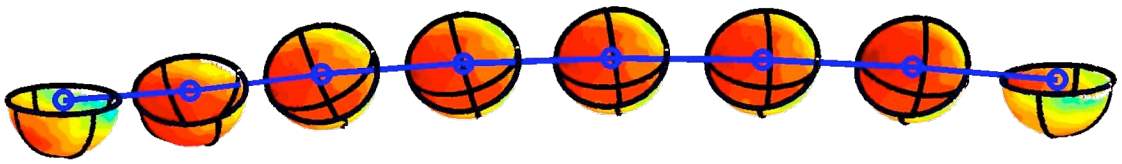

Figure 13: Modified radiation spheres applied along a sample turn.

For the first turn, 53° to the left at 120 knots in a slight climb (1.3°), the appropriate radiation sphere applied along the trajectory at 0.5 second intervals and at the correct orientation is shown above in Fig. 13.

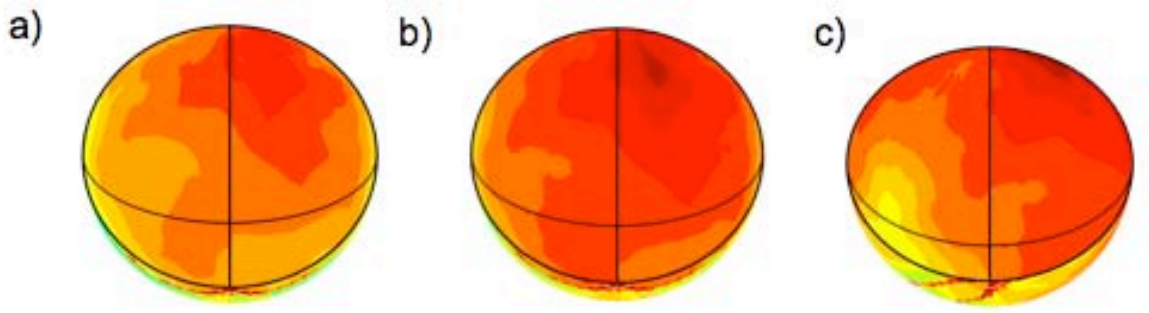

Figure 14: Radiation spheres corresponding to 120 knots in longitudinal flight (shown with respect to the main rotor shaft plane, a), in a 45 deg turn (shown with respect to the main rotor shaft plane , b) and in a 45 deg bank turn (shown with respect to the horizon, c).

Figure 14 shows the effect of turning flight on the radiation spheres for the MD902 helicopter. For the first turn in the trajectory under consideration (53° to the left at 120 knots in a slight climb), the radiation sphere with respect to the main rotor shaft plane corresponding to longitudinal flight at the same velocity and flight path angle is shown in Fig. 14a. The radiation pattern is characterized by a hot-spot in the advancing side of the

main rotor in the forward direction. Figure 14b shows the effect of the turn. With respect to the shaft plane the noise levels increases and the hot-spot intensifies. When seen with respect to the horizon plane, it is seen that during a left turn the hot-spot shift further in-plane. This has significant implications to detection of the helicopter. Thus the effect of turning to the left at 120 knots for the MD902 helicopter is seen to have the effect of increasing near-in-plane noise radiation directly ahead of the helicopter.

4. Summary and Conclusions

Conclusions

- Noise heard in the Cabin may not be what is important for Detection. Near in-plane noise generated near the advancing blade tip region often determines helicopter detection. These noise sources radiate near the plane of the rotor disk and are not heard in the helicopter cabin.
- Turning flight significantly alters the directivity and levels of radiated noise. The two most significant factors responsible for this are the banking of the tip path plane and an increase in rotor thrust. Increase in rotor thrust is typically associated with an increase in radiated helicopter noise. The banking of the tip path plane exposes the underside of the radiation sphere to near-in-plane observer. Also acoustic radiation characteristics above the rotor disk can become significant to the study of annoyance / detection during turning flight maneuvers.
- Transient maneuvers are usually associated with a significant increase of noise radiation but over a short period of time
- Extending RNM to include both Quasi-Static maneuvers and Transient maneuvers is critical to modeling realistic flight trajectories
- The technical approach used in this short-term project worked successfully. This approach of Quasi-Static acoustic prediction and Empirical correction for transient maneuver effects should be validated further and implemented in RNM.

Recommendations for Sphere Development

- Significant smearing in the lower harmonic acoustic energy is observed in the RNM spheres - this needs to be corrected
- The effect of ground reflections should account for moving unsteady directional sound source
- Main rotor noise and Tail rotor noise should be separated from overall acoustic radiation data and treated separately

Recommendations for Acoustic Mapping using RNM

- RNM should include a non-dimensional helicopter Rotor Performance Model (RPM) and a simple Source Noise Model (SNM) to enhance its mapping capabilities. Incorporating Q-SAM within RNM would be an important step forward in the development and applicability of RNM. This would replace the current trajectory refinement and sphere selection modules implemented in RNM.
- Flight testing in Controlled Maneuvering Flight conditions should be used as guidance for obtaining acoustic penalties to steady state or quasi steady data
- The source noise governing parameter list (currently Velocity and Flight Path Angle) for radiation sphere selection should be non-dimensionalized and extended to include the effects of
    - *Acceleration parallel to the flight path*
    - *Changes in Main Rotor Load factor*
    - *Main rotor tip path plane pitch and roll rate*

References

1. Page, J. A., Plotkin, K. J., Downing, J. M., James, M. and Ikelheimer, B., Chris Hobbs, "*Rotorcraft Noise Model - Technical Report and User Manual*", Wyle Report WR 05-02, Prepared for NASA Langley Research Center, Acoustics Branch, Hampton, VA, May 2005.

2. Gopalan, G., Schmitz, F. H., and Sim, B. W., "*Flight Path Management and Control Methodology to Reduce Helicopter Blade-Vortex (BVI) Noise,*" Conference Proceedings of the American Helicopter Society Vertical Lift Aircraft Design Conference, San Francisco, CA, January 2000.

3. Gopalan, G., "*Quasi-Static Acoustic Mapping of Helicopter Blade-Vortex Interaction Noise*", Doctoral Dissertation, University of Maryland, July 2004.

4. Sim, B. W., Beasman, T., Schmitz, F. H., Gopalan, G., "*In-Flight Blade-Vortex Interaction (BVI) Noise Measurements Using a Boom-Mounted Microphone Array*", Conference Proceedings of the American Helicopter Society Annual Forum, Baltimore, MD, June 2004.

5. Schmitz, F. H., Greenwood, E., Sickenberger, R., Gopalan, G., Sim, B. W., Connor, D., Moralez III, E. and Decker, W. A., "*Measurement and Characterization of Helicopter Noise in Steady-State and Maneuvering Flight*", Conference Proceedings

of the 63rd American Helicopter Society International Forum and Technology Display, Virginia Beach, VA, May 2007.

6. Gopalan, G. and Schmitz, F. H., "*Flight Path Control of Helicopter Blade-Vortex Interaction Noise in the Presence of Wind*", Presented at the 57th AHS International Forum and Technology Display, Phoenix, Washington DC, May 2001.

7. Schmitz, F. H., Gopalan, G. and Sim, B. W., "*Flight Trajectory Management to Reduce Helicopter Blade-Vortex Interaction (BVI) Noise with Head/Tailwind Effects*", Conference Proceedings of the 26th European Rotorcraft Forum, The Hague, The Netherlands, September 26-29, 2000.

8. Greenwood, E., Schmitz, F. H., Gopalan, G., Sim, B. W., "*Helicopter External Noise in Turning Flight: Theory and Experiment*", Conference Proceedings of the 63rd American Helicopter Society International Forum and Technology Display, Virginia Beach, VA, May 2007.

9. Gopalan, G. and Schmitz, F. H., "*A Sensitivity Analysis of the Quasi-Static Acoustic Mapping of Helicopter Blade-Vortex Interaction (BVI) Noise during Slowly Maneuvering Flight*", Conference Proceedings of the 9th AIAA/CEAS Aeroacoustics Conference, Hilton Head, South Carolina, May 2003.

Appendix A

RNM Acoustic Sphere Database Development from the MD902 Eglin Flight Test Data

This appendix describes the process that was used to develop the acoustic sphere database used in this project. The recent MD902 flight test data from Eglin was used as the basis for sphere development. All data reduction to develop the spheres from the flight track and microphone data was conducted by NASA Langley using RNM and ART. These spheres were used as input for the project.

The QSAM-PRIME project was only involved in sphere modifications based on maneuvering flight conditions as outlined in the report. The .nc NETCDF files were visualized, and manipulated using MATLAB code written for and during the execution of this project.

Initially a set of spheres was provided by NASA Langley based on a combination of ground based microphones and pole mounted microphones. A sample sphere from this set of spheres is shown in Figure A.1. The X-axis, as shown in the figure points towards the direction of flight, while the Z axis points upwards. This sphere coordinate system is the rotor shaft axis system.

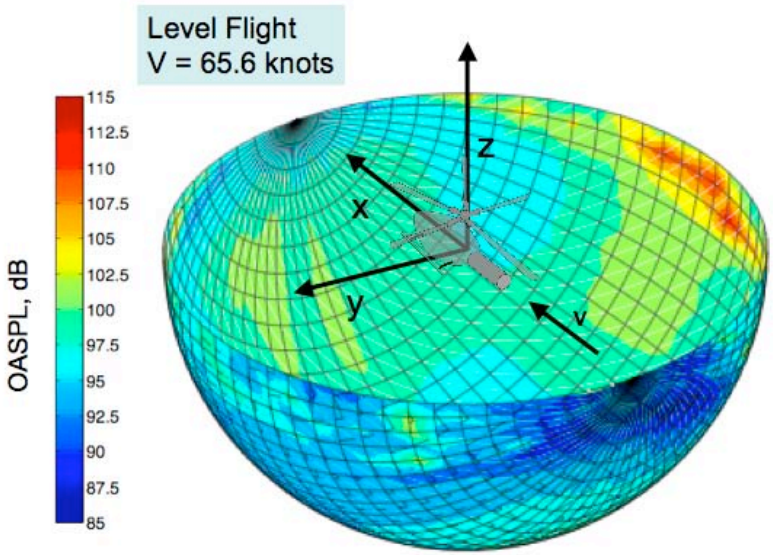

Figure A.1: RNM radiation sphere for the MD902 developed from pole-based Eglin data.

Figure A.1 shows an OASPL semi-sphere for the MD902 in level flight at a flight velocity of 65 knots. The semi-sphere shows high noise levels radiated to the right of the helicopter. This is uncharacteristic of known noise radiation trends for conventional helicopters, which tend to radiate noise directly ahead or below the rotor disk. When the flight velocity is increased in level flight, the radiated noise levels in general were seen to increase in level and to radiate more noise towards the front of the helicopter in the advancing side of the rotor, as seen in Fig. A.2. While the trend with increasing flight velocity was as expected, the noise radiation characteristics at lower flight velocities was not considered physically reasonable.

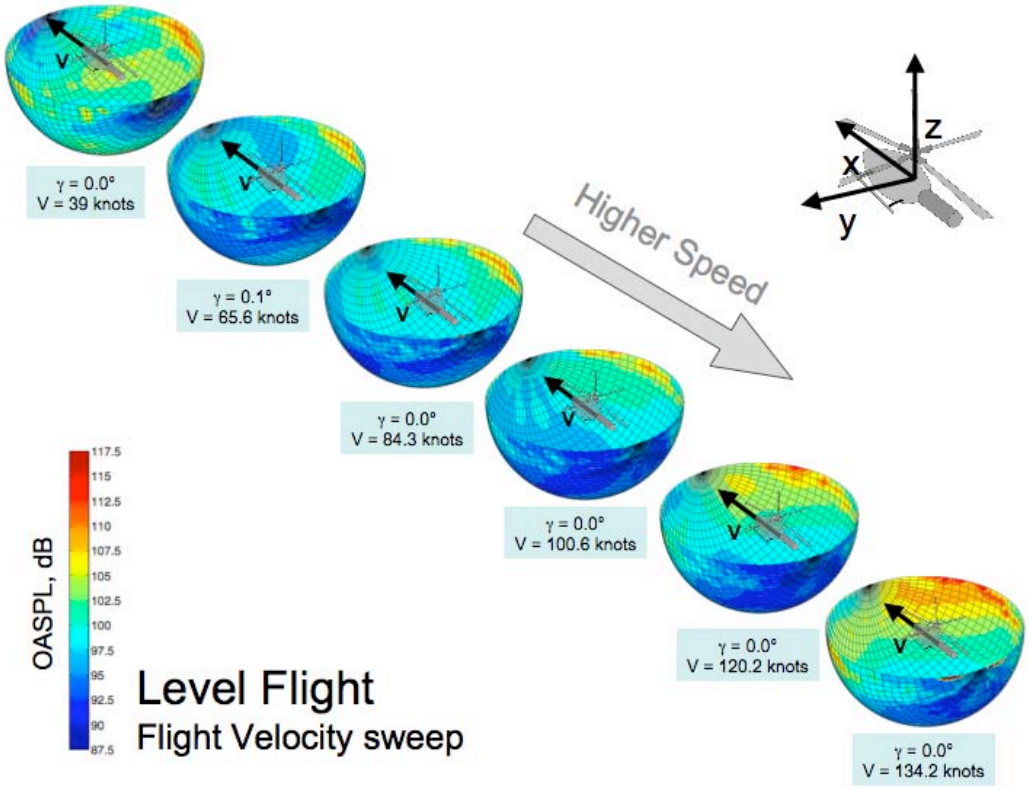

Figure A.2: RNM radiation spheres for the MD902 in level flight as a function of flight velocity developed from pole-based Eglin data.

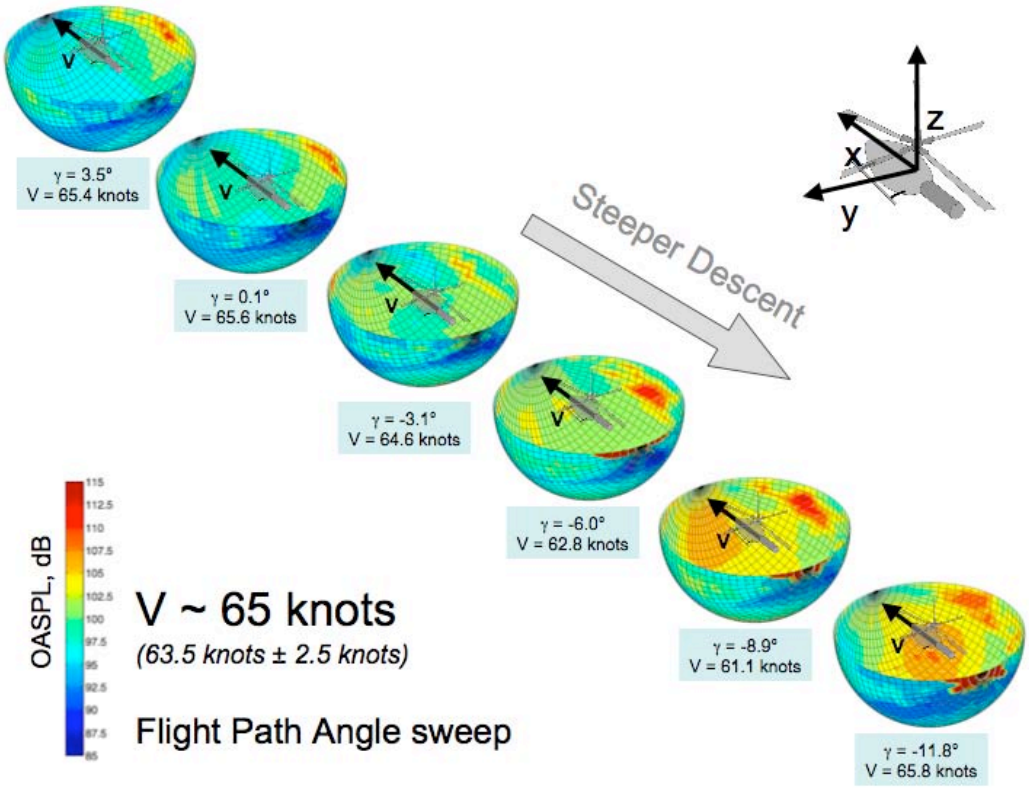

Figure A.3: RNM radiation spheres for the MD902 at a flight velocity of 65 knots as a function of flight path angle developed from pole-based Eglin data.

Figure A.3 shows the effect of changing flight path angle from +3.5° to -11.8°. Noise levels were observed to increase with steepening descent, peaking at a descent angle of about 8.9°. As the descent angle increased, the noise radiated out of place also increased alluding to an increase in the radiated loading and / or BVI noise. While this trend was considered reasonable, the high levels of OASPL radiated to the right of the helicopter was unexpected and unphysical. This feature in the initial set of spheres cast significant doubt on the noise trends. Further investigation alluded to the fact that the pole mounted microphones, which are very sensitive to ground reflections, may be the cause of this

feature in the data. The current data reduction process used by NASA Langley did not account for ground reflections.

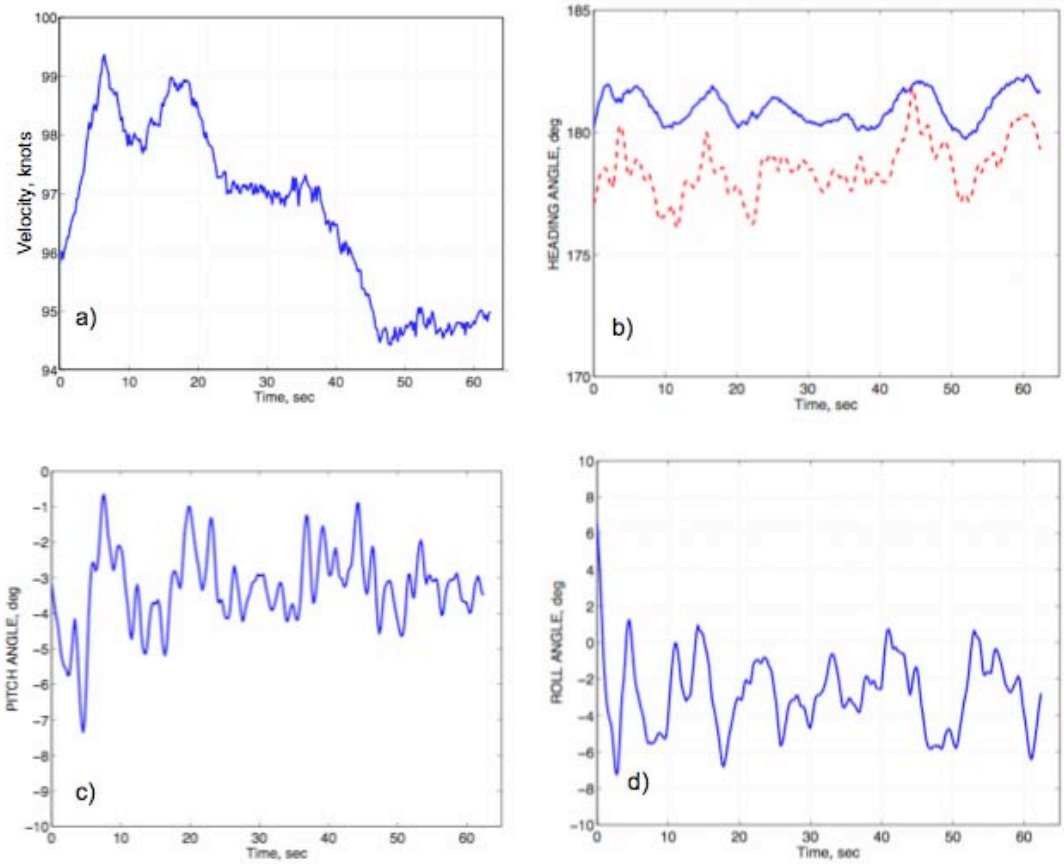

Figure A.4: Eglin flight track data for the MD902 in a level flight flyover at a flight velocity of 97 knots.

To explore this dataset more closely, a sample level flight case at 97 knots was selected. Figure A.4 shows the flight velocity, heading angle, helicopter pitch angle and helicopter roll angle time history for a one minute flyover segment, flown over a microphone array. While some high frequency fluctuations characteristic of flight test date were observed in the flight track data set, the flight conditions were seen to be have been held fairly well over the flight.

The acoustic pressure time history at the centerline microphone is shown in Fig. A.4. The time history was deemed to be characteristic of a flyover with the noise peaking as the helicopter approaches the microphone.

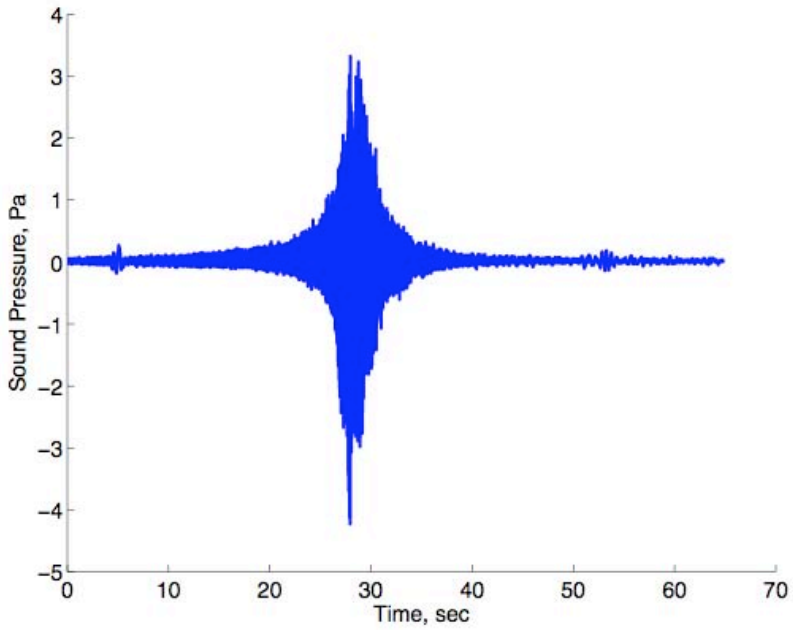

Figure A.4: Sound Pressure level time history at the centerline microphone from the Eglin flight data for the MD902 in a level flight flyover at a flight velocity of 97 knots.

A more detailed investigation of the spectral content of the acoustic data was conducted next. The data from Fig A.4 was divided into 0.5 second chunks and an FFT analysis was performed. Figure A.5 shows a sample FFT centered at a time of 0.5 sec. The vertical dashed lines represent the first four blade passage harmonics. The solid black line with inverted triangular symbols represents the FFT obtained from the RNM toolbox. This anaysis using a frequency bin width of 6.1 Hz.

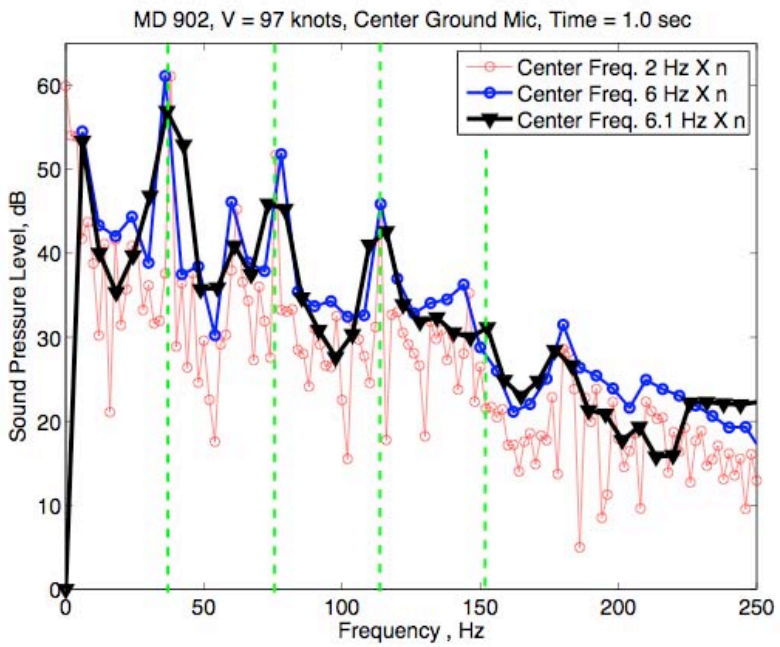

Figure A.5: Sound Pressure level frequency distribution analysis at the centerline microphone for the MD902 in level flight at a flight velocity of 97 knots at 1.0 second.

A spectral analysis independently conducted using MATLAB is shown with circular symbols with both a 6 Hz and 2 Hz frequency bin width. Compared to the MATLAB FFT, the FFT of the acoustic data from RNM showed smearing of the acoustic energy over 2 or 3 bins. The MATLAB FFT resulted in spectral energy that peaked at or near the harmonics of the blade passage frequency, which is characteristic of helicopter main rotor noise. Another feature that was observed was some sub-harmonic acoustic energy below the first rotor blade passage frequency and also between the first and second blade passage frequency as shown in Fig. A.5. This was considered to be unrepresentative of helicopter noise. The features observed in the above study were found to be repeated at a time of 5 sec (Fig. A.6) and 20 sec (Fig. A.7). In fact the spectral distribution at 5 sec was dominated by the acoustic energy at 6 Hz.

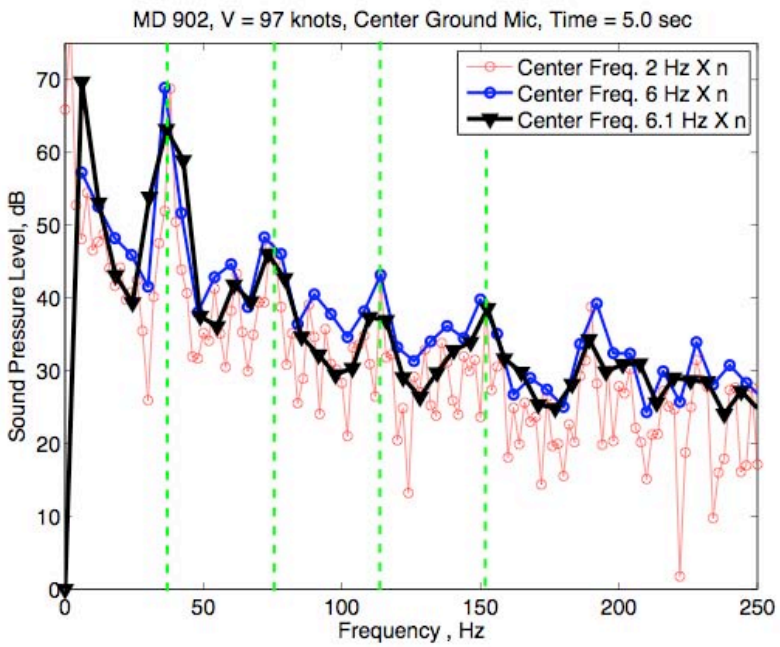

Figure A.6: Sound Pressure level frequency distribution analysis at the centerline microphone for the MD902 in level flight at a flight velocity of 97 knots at 5.0 seconds.

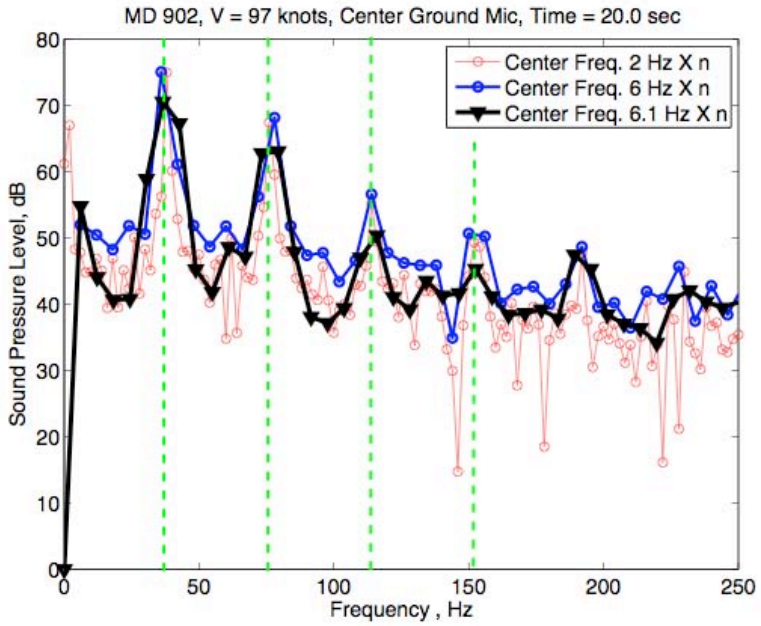

Figure A.7: Sound Pressure level frequency distribution analysis at the centerline microphone for the MD902 in level flight at a flight velocity of 97 knots at 20.0 seconds.

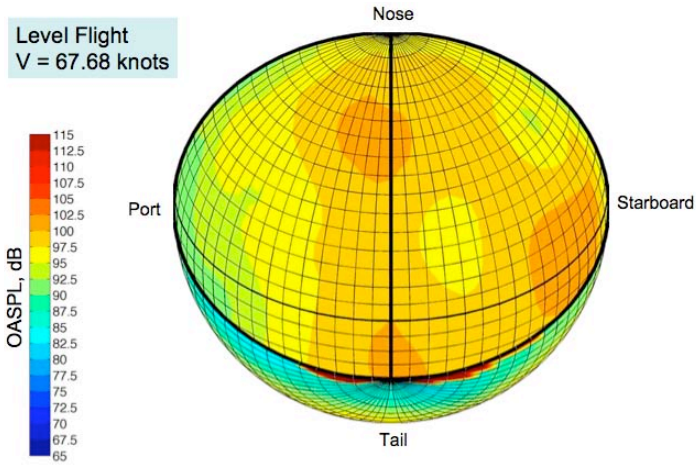

Figure A.8: A typical acoustic radiation semi-sphere for the MD902 based on ground based microphone data.

This first database of acoustic semi-spheres obtained using a combination of ground based and pole mounted microphones was considered unphysical and not representative of the acoustic characteristics of the MD902. This was mainly because of the hotspot location to the right of the helicopter. A second set of spheres was created using RNM and ART by NASA Langley but using only ground based microphones. This data would not have the problem of ground reflections that would have been present in the pole mounted microphones . Figure A.8 shows a noise radiation sphere developed from this new dataset for the MD902 in level flight at a flight velocity of 68 knots. Most of the acoustic energy is radiated directly ahead or to the right ad below the rotor. There is no hotspot observed to the right of the rotor disk. These considerations led the authors to believe that the new dataset was more physically representative of the acoustic radiation characteristics of the MD902.

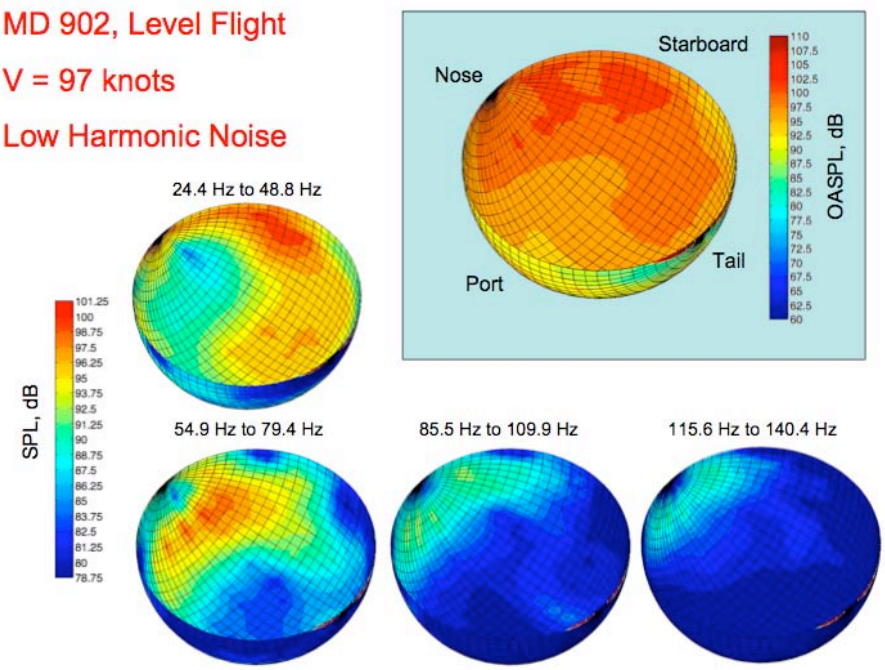

Figure A.9: Acoustic radiation semi-spheres for the MD902 in level flight at a velocity of 97 knots. OASPL as well as the SPL in the first four main rotor blade passage harmonics are shown based on ground microphones.

An investigation was then conducted into the spectral distribution of the acoustic energy in the new spheres. Figure A.9 shows the acoustic radiation semi-sphere for the MD902 in level flight at 97 knots (top right of the figure). The acoustic energy is mostly radiated to the advancing side (second quadrant) close to and slightly below the rotor disk, which is to be expected. The overall acoustic energy was then spectrally decomposed and the acoustic energy corresponding to the first four main rotor blade passage harmonics were plotted over the radiation sphere. The frequency bin width was taken to be 24.4 Hz. These four semi-spheres are also shown in Fig. A.9. Most of the acoustic energy is seen to be concentrated in the first two harmonics of main rotor blade passage. While the first harmonic energy is mostly radiated near the plane of the rotor disk towards the advancing

side of the rotor, the second harmonic energy is mostly radiated below the rotor disk but in the direction of flight.

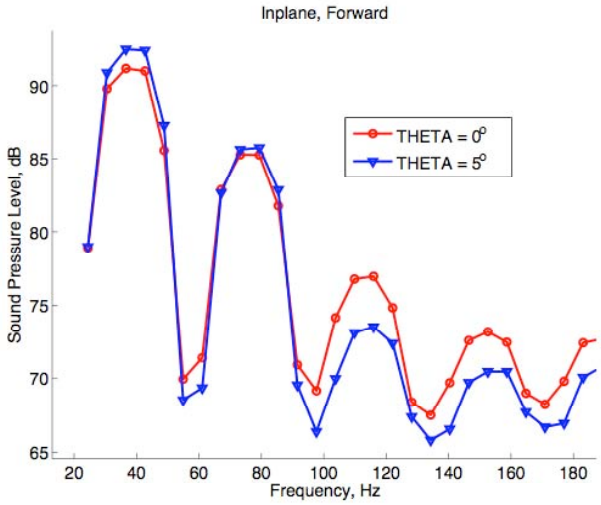

Figure A.10: Data smearing in the Sound Pressure level frequency distribution of near in-plane RNM semi-sphere acoustic data for the MD902 in level flight at a flight velocity of 97 knots.

The problem of spectral smearing observed in the previous set of spheres was however present in the new dataset of spheres as well. Figure A.10 shows the spectral distribution of the acoustic energy at two locations on the semi-sphere for the MD902 at a level flight condition of 97 knots. Both these location were selected to lie in the centerline (directly ahead, $\phi = 0°$), at elevation angles (θ) of 0° and 5°. These near in-plane observer locations showed significant acoustic energy spread about the blade passage harmonics. This problem is considered to be endemic to the RNM signal processing toolbox and needs to be investigated further. However in the interest of time this issue was not further resolved and the new set of spheres were used for the project.

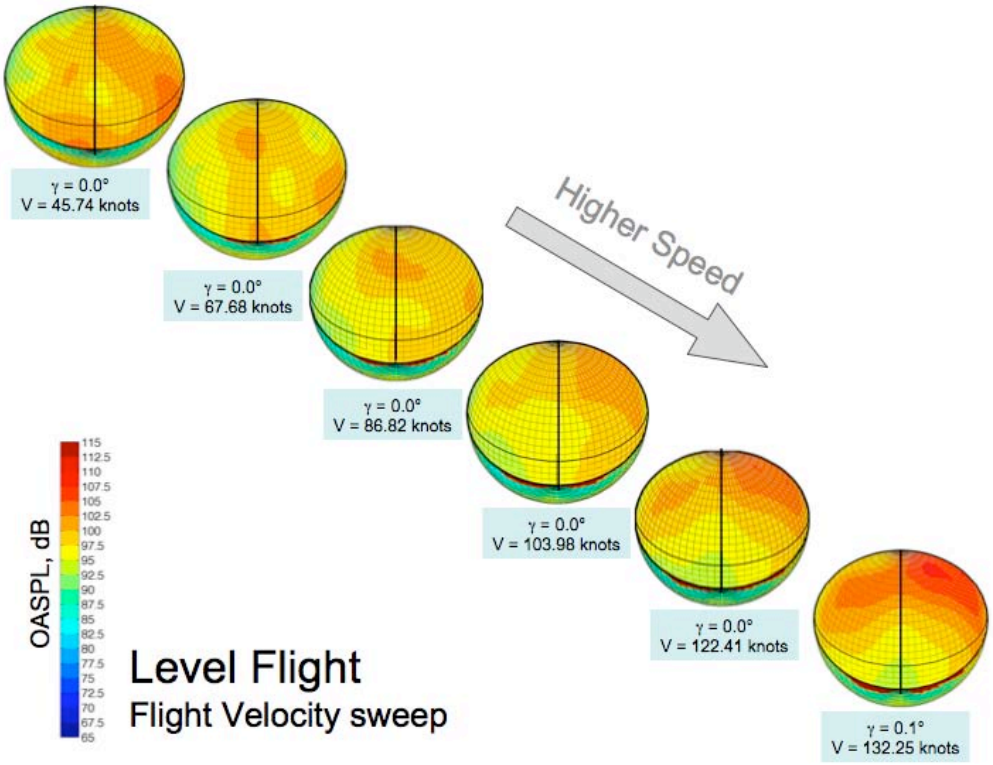

Figure A.11: RNM radiation spheres for the MD902 in level flight as a function of flight velocity developed from ground-based Eglin data.

A flight velocity sweep in level flight showed that the effect of increasing flight velocity was to increase the peak hotspot of the OASPL and to position it more in-plane in directly ahead of the rotor disk in the direction of flight, as can be seen in Fig. A.11. This new dataset was considered reasonable for the purpose of this project and an acoustic database was then developed from these semi-spheres for use by the QSAM-PRIME subroutine.

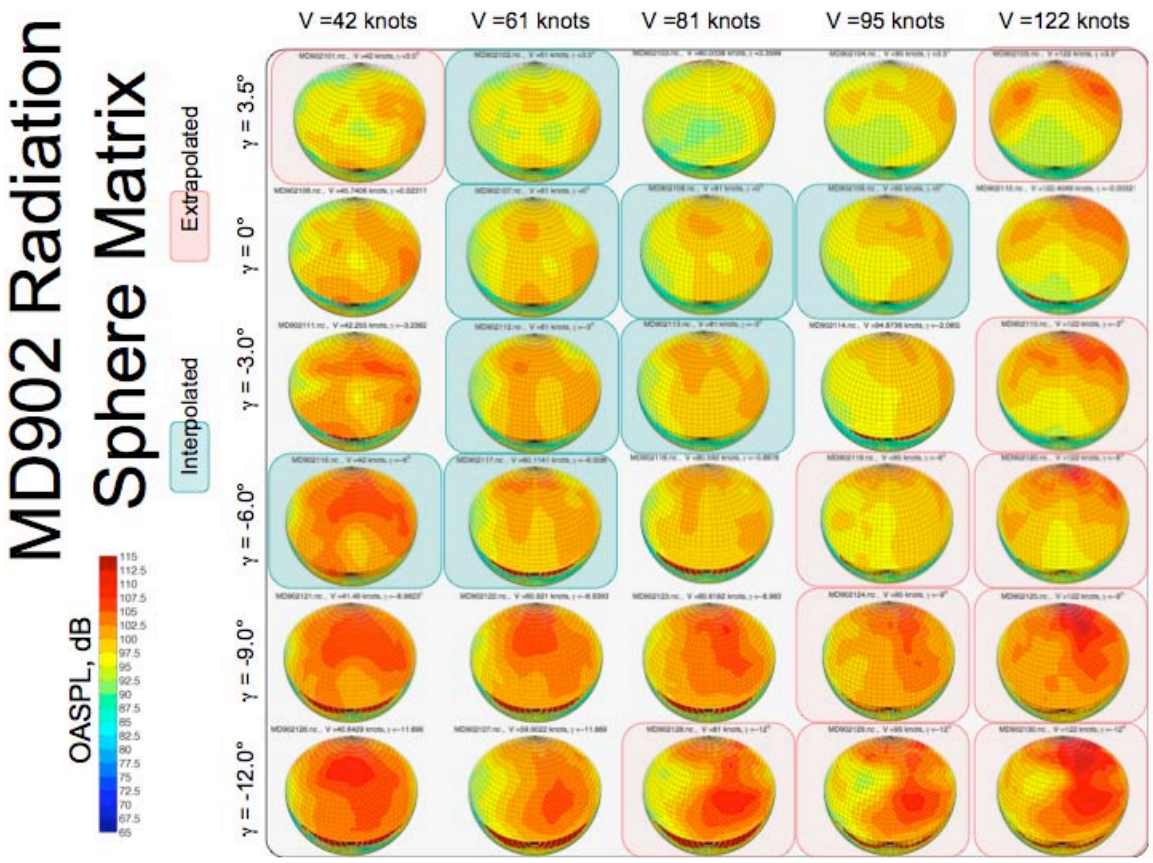

Figure A.12: RNM Radiation spheres stored in a rectangular Velocity-Flight Path Angle grid.

Based on the available semi-sphere flight conditions (velocity and flight path angle) a flight path angle range from +3.5° to -12° and a velocity range from 42 knots to 122 knots was selected as shown in Fig. A.12. A rectangular velocity versus flight path angle matrix was developed using both interpolation (cubic spline, on acoustic energy levels) and extrapolation (2-D linear, on acoustic energy levels). This matrix of 30 spheres was then used as input to the QSAM-PRIME subroutine and used to develop spheres for use by RNM.

Appendix B

Maneuver Details for the Reduced Trajectory

1. Accelerate from 50 to 120 knots at 0.1 g (S1)

I. ***Change in Acceleration Maneuver***

1) Effective Flight Path Angle = 1.3 deg + 3 deg
2) Load Factor = 1.0
3) Segment Velocity = 50 knots
4) Change in Acceleration over Maneuver = 0.1 g
5) **Change in Roll Angle Compared to Steady State = 0**
6) **Roll Rate = 0**
7) **Change in Pitch Angle Compared to Steady State = -3 deg**
8) **Pitch Rate = -12 deg per sec**
9) Time of Maneuver = 0.5 sec

II. ***Constant Acceleration Maneuver***

1) Effective Flight Path Angle = 1.3 deg + 6 deg
2) Load Factor = 1.0
3) Initial Velocity = 50 knots, Final Velocity = 120 knots
4) Acceleration = 0.1 g
5) **Change in Roll Angle Compared to Steady State = 0**
6) **Roll Rate = 0**
7) **Change in Pitch Angle Compared to Steady State = 6 deg**
8) **Pitch Rate = 0**
9) Time of Maneuver = 37.0 sec

III. ***Change in Acceleration Maneuver***

1) Effective Flight Path Angle = 1.3 deg + 3 deg
2) Load Factor = 1.0
3) Segment Velocity = 120 knots
4) Change in Acceleration over Maneuver = -0.1 g
5) **Change in Roll Angle Compared to Steady State = 0**

6) **Roll Rate = 0**

7) **Change in Pitch Angle Compared to Steady State = 3 deg**

8) **Pitch Rate = +12 deg per sec**

9) Time of Maneuver = 0.5 sec

2. Constant Speed at 120 knots (S1)

1) Effective Flight Path Angle = 1.3 deg
2) Load factor = 1.0
3) Velocity = 120 knots
4) **Change in Roll Angle Compared to Steady State = 0**
5) **Roll Rate = 0**
6) **Change in Pitch Angle Compared to Steady State = 0**
7) **Pitch Rate = 0**
8) Time of Segment = 431 sec

3. Change heading by 53 deg to the left (T1)

I. ***Change in Bank Angle Maneuver***

1) Effective Flight Path Angle = 1.3 deg
2) Load Factor = 1.0 to 1.4, linearly
3) Segment Velocity = 120 knots
4) **Change in Roll Angle Compared to Steady State = 0 deg to 45 deg, linearly**
5) **Roll Rate = 15 deg per sec**
6) **Change in Pitch Angle Compared to Steady State = 0 deg**
7) **Pitch Rate = 0 deg per sec**
8) **Change in Heading Angle = 12 deg**
9) Time of Maneuver = 3 sec

II. ***Constant Bank Angle Maneuver***

1) Effective Flight Path Angle = 1.3 deg
2) Load Factor = 1.4
3) Segment Velocity = 120 knots

4) **Change in Roll Angle Compared to Steady State = 45 deg**
5) **Roll Rate = 0**
6) **Change in Pitch Angle Compared to Steady State = 0**
7) **Pitch Rate = 6 deg per sec**
8) **Change in Heading Angle = 29 deg**
9) Time of Maneuver = 3 sec

III. ***Change in Bank Angle Maneuver***

1) Effective Flight Path Angle = 1.3 deg
2) Load Factor = 1.4 to 1.0, linearly
3) Segment Velocity = 120 knots
4) **Change in Roll Angle Compared to Steady State = 45 deg to 0 deg, linearly**
5) **Roll Rate = -15 deg per sec**
6) **Change in Pitch Angle Compared to Steady State = 0 deg**
7) **Pitch Rate = 0 deg per sec**
8) **Change in Heading Angle = 12 deg**
9) Time of Maneuver = 3 sec

4. Increase Flight Path Angle by 3.4 deg (T1)

1) Effective Flight Path Angle = 1.3 deg + 1.7 deg
2) Load Factor = 1.4
3) Segment Velocity = 120 knots
4) **Change in Roll Angle Compared to Steady State = 0 deg**
5) **Roll Rate = 0**
6) **Change in Pitch Angle Compared to Steady State = 0 deg**
7) **Pitch Rate = 0 deg per sec**
8) Time of Maneuver = 1 sec
9) Final Flight Path Angle = 4.6 deg

5. Constant Speed at 120 knots (S2)

1) Effective Flight Path Angle = 4.6 deg
2) Load factor = 1.0
3) Velocity = 120 knots
4) **Change in Roll Angle Compared to Steady State = 0**
5) **Roll Rate = 0**
6) **Change in Pitch Angle Compared to Steady State = 0**
7) **Pitch Rate = 0**
8) Time of Segment = 128.5 sec

6. Change heading by 31 deg to the right (T2)

I. ***Change in Bank Angle Maneuver***

1) Effective Flight Path Angle = 4.6 deg
2) Load Factor = 1.0 to 1.4 linearly
3) Segment Velocity = 120 knots
4) **Change in Roll Angle Compared to Steady State = 0 deg to 45 deg, linearly**
5) **Roll Rate = 15 deg per sec**
6) **Change in Pitch Angle Compared to Steady State = 0 deg**
7) **Pitch Rate = 0 deg per sec**
8) **Change in Heading Angle = 12 deg**
9) Time of Maneuver = 3 sec

II. ***Constant Bank Angle Maneuver***

1) Effective Flight Path Angle = 4.6 deg
2) Load Factor = 1.4
3) Segment Velocity = 120 knots
4) **Change in Roll Angle Compared to Steady State = 45 deg**
5) **Roll Rate = 0**
6) **Change in Pitch Angle Compared to Steady State = 0**
7) **Pitch Rate = 6 deg per sec**
8) **Change in Heading Angle = 7 deg**
9) Time of Maneuver = 1 sec

III. ***Change in Bank Angle Maneuver***

1) Effective Flight Path Angle = 4.6 deg
2) Load Factor = 1.4 to 1.0 linearly
3) Segment Velocity = 120 knots
4) **Change in Roll Angle Compared to Steady State = 45 deg to 0 deg, linearly**
5) **Roll Rate = -15 deg per sec**
6) **Change in Pitch Angle Compared to Steady State = 0 deg**
7) **Pitch Rate = 0 deg per sec**
8) **Change in Heading Angle = 12 deg**
9) Time of Maneuver = 3 sec

7. Reduce Flight Path Angle by 6.4 deg (T2)

1) Effective Flight Path Angle = 4.6 deg - 3.2 deg
2) Load Factor = 0.65
3) Segment Velocity = 120 knots
4) **Change in Roll Angle Compared to Steady State = 0 deg**
5) **Roll Rate = 0**
6) **Change in Pitch Angle Compared to Steady State = 0 deg**
7) **Pitch Rate = 0 deg per sec**
8) Time of Maneuver = 2 sec
9) Final Flight Path Angle = -1.8 deg

8. Constant Speed at 120 knots (S3)

1) Effective Flight Path Angle = -1.8 deg
2) Load factor = 1.0
3) Velocity = 120 knots
4) **Change in Roll Angle Compared to Steady State = 0**
5) **Roll Rate = 0**
6) **Change in Pitch Angle Compared to Steady State = 0**
7) **Pitch Rate = 0**

8) Time of Segment = 120.5 sec

9. Change heading by 48 deg to the right (T3)

I. ***Change in Bank Angle Maneuver***

1) Effective Flight Path Angle = -1.8 deg
2) Load Factor = 1.0 to 1.4, linearly
3) Segment Velocity = 120 knots
4) **Change in Roll Angle Compared to Steady State = 0 deg to 45 deg, linearly**
5) **Roll Rate = 15 deg per sec**
6) **Change in Pitch Angle Compared to Steady State = 0 deg**
7) **Pitch Rate = 0 deg per sec**
8) **Change in Heading Angle = 12 deg**
9) Time of Maneuver = 3 sec

II. ***Constant Bank Angle Maneuver***

1) Effective Flight Path Angle = -1.8 deg
2) Load Factor = 1.4
3) Segment Velocity = 120 knots
4) **Change in Roll Angle Compared to Steady State = 45 deg**
5) **Roll Rate = 0**
6) **Change in Pitch Angle Compared to Steady State = 0**
7) **Pitch Rate = 6 deg per sec**
8) **Change in Heading Angle = 24 deg**
9) Time of Maneuver = 3 sec

III. ***Change in Bank Angle Maneuver***

1) Effective Flight Path Angle = -1.8 deg
2) Load Factor = 1.4 to 1.0, linearly
3) Segment Velocity = 120 knots
4) **Change in Roll Angle Compared to Steady State = 45 deg to 0 deg, linearly**
5) **Roll Rate = -15 deg per sec**

6) **Change in Pitch Angle Compared to Steady State = 0 deg**
7) **Pitch Rate = 0 deg per sec**
8) **Change in Heading Angle = 12 deg**
9) Time of Maneuver = 3 sec

10. Increase Flight Path Angle by 1.3 deg (T3)

1) Effective Flight Path Angle = -1.8 deg + 0.7 deg
2) Load Factor = 1.3
3) Segment Velocity = 120 knots
4) **Change in Roll Angle Compared to Steady State = 0 deg**
5) **Roll Rate = 0**
6) **Change in Pitch Angle Compared to Steady State = 0 deg**
7) **Pitch Rate = 0 deg per sec**
8) Time of Maneuver = 0.5 sec
9) Final Flight Path Angle = -0.4 deg

11. Constant Speed at 120 knots (S4)

1) Effective Flight Path Angle = -0.4 deg
2) Load factor = 1.0
3) Velocity = 120 knots
4) **Change in Roll Angle Compared to Steady State = 0**
5) **Roll Rate = 0**
6) **Change in Pitch Angle Compared to Steady State = 0**
7) **Pitch Rate = 0**
8) Time of Segment = 340.5 sec

12. Change heading by 50 deg to the right (T4)

I. ***Change in Bank Angle Maneuver***

1) Effective Flight Path Angle = -0.4 deg
2) Load Factor = 1.0 to 1.4, linearly
3) Segment Velocity = 120 knots

4) **Change in Roll Angle Compared to Steady State = 0 deg to 45 deg, linearly**
5) **Roll Rate = 15 deg per sec**
6) **Change in Pitch Angle Compared to Steady State = 0 deg**
7) **Pitch Rate = 0 deg per sec**
8) **Change in Heading Angle = 12 deg**
9) Time of Maneuver = 3 sec

II. ***Constant Bank Angle Maneuver***

1) Effective Flight Path Angle = -0.4 deg
2) Load Factor = 1.4
3) Segment Velocity = 120 knots
4) **Change in Roll Angle Compared to Steady State = 45 deg**
5) **Roll Rate = 0**
6) **Change in Pitch Angle Compared to Steady State = 0**
7) **Pitch Rate = 6 deg per sec**
8) **Change in Heading Angle = 16 deg**
9) Time of Maneuver = 3 sec

III. ***Change in Bank Angle Maneuver***

1) Effective Flight Path Angle = -0.4 deg
2) Load Factor = 1.4 to 1.0, linearly
3) Segment Velocity = 120 knots
4) **Change in Roll Angle Compared to Steady State = 45 deg to 0 deg, linearly**
5) **Roll Rate = -15 deg per sec**
6) **Change in Pitch Angle Compared to Steady State = 0 deg**
7) **Pitch Rate = 0 deg per sec**
8) **Change in Heading Angle = 12 deg**
9) Time of Maneuver = 3 sec

13. Increase Flight Path Angle by 2.8 deg (T4)

1) Effective Flight Path Angle = -0.4 deg + 1.4 deg
2) Load Factor = 1.3
3) Segment Velocity = 120 knots
4) **Change in Roll Angle Compared to Steady State = 0 deg**
5) **Roll Rate = 0**
6) **Change in Pitch Angle Compared to Steady State = 0 deg**
7) **Pitch Rate = 0 deg per sec**
8) Time of Maneuver = 1 sec
9) Final Flight Path Angle = 2.4 deg

14. Constant Speed at 120 knots (S5)

1) Effective Flight Path Angle = 2.4 deg
2) Load factor = 1.0
3) Velocity = 120 knots
4) **Change in Roll Angle Compared to Steady State = 0**
5) **Roll Rate = 0**
6) **Change in Pitch Angle Compared to Steady State = 0**
7) **Pitch Rate = 0**
8) Time of Segment = 271.5 sec

15. Change heading by 20 deg to the right (T5)

I. ***Change in Bank Angle Maneuver***

1) Effective Flight Path Angle = 2.4 deg
2) Load Factor = 1.0 to 1.4, linearly
3) Segment Velocity = 120 knots
4) **Change in Roll Angle Compared to Steady State = 0 deg to 45 deg, linearly**
5) **Roll Rate = 15 deg per sec**
6) **Change in Pitch Angle Compared to Steady State = 0 deg**
7) **Pitch Rate = 0 deg per sec**
8) **Change in Heading =**

9) Time of Maneuver = 2.75 sec

II. ***Change in Bank Angle Maneuver***

1) Effective Flight Path Angle = 2.4 deg
2) Load Factor = 1.4 to 1.0, linearly
3) Segment Velocity = 120 knots
4) **Change in Roll Angle Compared to Steady State = 45 deg to 0 deg, linearly**
5) **Roll Rate = -15 deg per sec**
6) **Change in Pitch Angle Compared to Steady State = 0 deg**
7) **Pitch Rate = 0 deg per sec**
8) **Change in Heading =**
9) Time of Maneuver = 2.75 sec

16. Decrease Flight Path Angle by 2.1 deg (T5)

1) Effective Flight Path Angle = 2.4 deg - 1.0 deg
2) Load Factor = 0.87
3) Segment Velocity = 120 knots
4) **Change in Roll Angle Compared to Steady State = 0 deg**
5) **Roll Rate = 0**
6) **Change in Pitch Angle Compared to Steady State = 0 deg**
7) **Pitch Rate = 0 deg per sec**
8) Time of Maneuver = 1 sec
9) Final Flight Path Angle = 0.3 deg

17. Constant Speed at 120 knots (S6)

1) Effective Flight Path Angle = 0.3 deg
2) Load factor = 1.0
3) Velocity = 120 knots
4) **Change in Roll Angle Compared to Steady State = 0**
5) **Roll Rate = 0**
6) **Change in Pitch Angle Compared to Steady State = 0**

7) **Pitch Rate = 0**

8) Time of Segment = 714 sec

18. Change heading by 13 deg to the right (T6)

I. ***Change in Bank Angle Maneuver***

1) Effective Flight Path Angle = 0.3 deg
2) Load Factor = 1.0 to 1.3, linearly
3) Segment Velocity = 120 knots
4) **Change in Roll Angle Compared to Steady State = 0 deg to 45 deg, linearly**
5) **Roll Rate = 15 deg per sec**
6) **Change in Pitch Angle Compared to Steady State = 0 deg**
7) **Pitch Rate = 0 deg per sec**
8) **Change in Heading = 6.5 deg**
9) Time of Maneuver = 2.25 sec

II. ***Change in Bank Angle Maneuver***

1) Effective Flight Path Angle = 0.3 deg
2) Load Factor = 1.3 to 1.0, linearly
3) Segment Velocity = 120 knots
4) **Change in Roll Angle Compared to Steady State = 45 deg to 0 deg, linearly**
5) **Roll Rate = -15 deg per sec**
6) **Change in Pitch Angle Compared to Steady State = 0 deg**
7) **Pitch Rate = 0 deg per sec**
8) **Change in Heading = 6.5 deg**
9) Time of Maneuver = 2.25 sec

19. Constant Speed at 120 knots (S7)

1) Effective Flight Path Angle = 0.0 deg
2) Load factor = 1.0
3) Velocity = 120 knots

4) **Change in Roll Angle Compared to Steady State = 0**
5) **Roll Rate = 0**
6) **Change in Pitch Angle Compared to Steady State = 0**
7) **Pitch Rate = 0**
8) Time of Segment = 621.5 sec

20. Change heading by 19 deg to the right (T7)

I. ***Change in Bank Angle Maneuver***

1) Effective Flight Path Angle = 0.3 deg
2) Load Factor = 1.0 to 1.4, linearly
3) Segment Velocity = 120 knots
4) **Change in Roll Angle Compared to Steady State = 0 deg to 45 deg, linearly**
5) **Roll Rate = 15 deg per sec**
6) **Change in Pitch Angle Compared to Steady State = 0 deg**
7) **Pitch Rate = 0 deg per sec**
8) **Change in Heading = 9.5 deg**
9) Time of Maneuver = 2.75 sec

II. ***Change in Bank Angle Maneuver***

1) Effective Flight Path Angle = 0.3 deg
2) Load Factor = 1.4 to 1.0, linearly
3) Segment Velocity = 120 knots
4) **Change in Roll Angle Compared to Steady State = 45 deg to 0 deg, linearly**
5) **Roll Rate = -15 deg per sec**
6) **Change in Pitch Angle Compared to Steady State = 0 deg**
7) **Pitch Rate = 0 deg per sec**
8) **Change in Heading = 9.5 deg**
9) Time of Maneuver = 2.75 sec

21. Decrease Flight Path Angle by 4.6 deg (T7)

1) Effective Flight Path Angle = 0 deg - 2.3 deg
2) Load Factor = 0.5
3) Segment Velocity = 120 knots
4) **Change in Roll Angle Compared to Steady State = 0 deg**
5) **Roll Rate = 0**
6) **Change in Pitch Angle Compared to Steady State = 0 deg**
7) **Pitch Rate = 0 deg per sec**
8) Time of Maneuver = 1 sec
9) Final Flight Path Angle = -4.7 deg

22. Decelerate from 120 to 80 knots at 0.1 g (S8)

I. ***Change in Acceleration Maneuver***

1) Effective Flight Path Angle = -4.7 deg - 3 deg
2) Load Factor = 1.0
3) Segment Velocity = 120 knots
4) Change in Acceleration over Maneuver = 0.1 g
5) **Change in Roll Angle Compared to Steady State = 0**
6) **Roll Rate = 0**
7) **Change in Pitch Angle Compared to Steady State = -3 deg**
8) **Pitch Rate = 12 deg per sec**
9) Time of Maneuver = 0.5 sec

II. ***Constant Acceleration Maneuver***

1) Effective Flight Path Angle = -4.7 deg - 6 deg
2) Load Factor = 1.0
3) Initial Velocity = 120 knots, Final Velocity = 80 knots
4) Deceleration = 0.1 g
5) **Change in Roll Angle Compared to Steady State = 0**
6) **Roll Rate = 0**
7) **Change in Pitch Angle Compared to Steady State = 6 deg**
8) **Pitch Rate = 0**

9) Time of Maneuver = 21.0 sec

III. ***Change in Acceleration Maneuver***

1) Effective Flight Path Angle = -4.7 deg - 3 deg
2) Load Factor = 1.0
3) Segment Velocity = 80 knots
4) Change in Acceleration over Maneuver = -0.1 g
5) **Change in Roll Angle Compared to Steady State = 0**
6) **Roll Rate = 0**
7) **Change in Pitch Angle Compared to Steady State = 3 deg**
8) **Pitch Rate = -12 deg per sec**
9) Time of Maneuver = 0.5 sec

23. Constant Speed at 80 knots (S8)

1) Effective Flight Path Angle = -4.7 deg
2) Load factor = 1.0
3) Velocity = 80 knots
4) **Change in Roll Angle Compared to Steady State = 0**
5) **Roll Rate = 0**
6) **Change in Pitch Angle Compared to Steady State = 0**
7) **Pitch Rate = 0**
8) Time of Segment = 331 sec

24. Change heading by 11 deg to the right (T8)

I. ***Change in Bank Angle Maneuver***

1) Effective Flight Path Angle = -4.7 deg
2) Load Factor = 1.0 to 1.23, linearly
3) Segment Velocity = 80 knots
4) **Change in Roll Angle Compared to Steady State = 0 deg to 25 deg, linearly**
5) **Roll Rate = 15 deg per sec**
6) **Change in Pitch Angle Compared to Steady State = 0 deg**

7) **Pitch Rate = 0 deg per sec**

8) **Change in Heading = 5.5 deg**

9) Time of Maneuver = 1.75 sec

II. ***Change in Bank Angle Maneuver***

1) Effective Flight Path Angle = -4.7 deg

2) Load Factor = 1.23 to 1.0, linearly

3) Segment Velocity = 80 knots

4) **Change in Roll Angle Compared to Steady State = 45 deg to 0 deg, linearly**

5) **Roll Rate = -15 deg per sec**

6) **Change in Pitch Angle Compared to Steady State = 0 deg**

7) **Pitch Rate = 0 deg per sec**

8) **Change in Heading = 5.5 deg**

9) Time of Maneuver = 1.75 sec

23. Constant Speed at 80 knots (S8)

1) Effective Flight Path Angle = -4.7 deg

2) Load factor = 1.0

3) Velocity = 80 knots

4) **Change in Roll Angle Compared to Steady State = 0**

5) **Roll Rate = 0**

6) **Change in Pitch Angle Compared to Steady State = 0**

7) **Pitch Rate = 0**

8) Time of Segment = 331 sec

24. Change heading by 11 deg to the right (T8)

I. ***Change in Bank Angle Maneuver***

1) Effective Flight Path Angle = -4.7 deg

2) Load Factor = 1.0 to 1.23, linearly

3) Segment Velocity = 80 knots

4) **Change in Roll Angle Compared to Steady State = 0 deg to 25 deg,**

linearly

5) **Roll Rate = 15 deg per sec**
6) **Change in Pitch Angle Compared to Steady State = 0 deg**
7) **Pitch Rate = 0 deg per sec**
8) **Change in Heading = 5.5 deg**
9) Time of Maneuver = 1.75 sec

II. ***Change in Bank Angle Maneuver***

1) Effective Flight Path Angle = -4.7 deg
2) Load Factor = 1.23 to 1.0, linearly
3) Segment Velocity = 80 knots
4) **Change in Roll Angle Compared to Steady State = 45 deg to 0 deg, linearly**
5) **Roll Rate = -15 deg per sec**
6) **Change in Pitch Angle Compared to Steady State = 0 deg**
7) **Pitch Rate = 0 deg per sec**
8) **Change in Heading = 5.5 deg**
9) Time of Maneuver = 1.75 sec

25. Increase Flight Path Angle by 1 deg (T8)

1) Effective Flight Path Angle = -4.7 deg + 0.5 deg
2) Load Factor = 1.15
3) Segment Velocity = 80 knots
4) **Change in Roll Angle Compared to Steady State = 0 deg**
5) **Roll Rate = 0**
6) **Change in Pitch Angle Compared to Steady State = 0 deg**
7) **Pitch Rate = 0 deg per sec**
8) Time of Maneuver = 0.5 sec
9) Final Flight Path Angle = -3.7 deg

26. Constant Speed at 80 knots (S9)

1) Effective Flight Path Angle = -3.7 deg
2) Load factor = 1.0
3) Velocity = 80 knots
4) **Change in Roll Angle Compared to Steady State = 0**
5) **Roll Rate = 0**
6) **Change in Pitch Angle Compared to Steady State = 0**
7) **Pitch Rate = 0**
8) Time of Segment = 55 sec

27. Increase Flight Path Angle by 3.2 deg (T9)

1) Effective Flight Path Angle = -3.7 deg + 1.6 deg
2) Load Factor = 1.5
3) Segment Velocity = 80 knots
4) **Change in Roll Angle Compared to Steady State = 0 deg**
5) **Roll Rate = 0**
6) **Change in Pitch Angle Compared to Steady State = 0 deg**
7) **Pitch Rate = 0 deg per sec**
8) Time of Maneuver = 0.5 sec
9) Final Flight Path Angle = -0.5 deg

28. Constant Speed at 80 knots (S10)

1) Effective Flight Path Angle = -0.5 deg
2) Load factor = 1.0
3) Velocity = 80 knots
4) **Change in Roll Angle Compared to Steady State = 0**
5) **Roll Rate = 0**
6) **Change in Pitch Angle Compared to Steady State = 0**
7) **Pitch Rate = 0**
8) Time of Segment = 71 sec

29. Change heading by 42 deg to the right (T10)

I. ***Change in Bank Angle Maneuver***

1) Effective Flight Path Angle = -0.5 deg
2) Load Factor = 1.0 to 1.4, linearly
3) Segment Velocity = 80 knots
4) **Change in Roll Angle Compared to Steady State = 0 deg to 45 deg, linearly**
5) **Roll Rate = 15 deg per sec**
6) **Change in Pitch Angle Compared to Steady State = 0 deg**
7) **Pitch Rate = 0 deg per sec**
8) **Change in Heading Angle = 18 deg**
9) Time of Maneuver = 3 sec

II. ***Constant Bank Angle Maneuver***

1) Effective Flight Path Angle = -0.5 deg
2) Load Factor = 1.4
3) Segment Velocity = 80 knots
4) **Change in Roll Angle Compared to Steady State = 45 deg**
5) **Roll Rate = 0**
6) **Change in Pitch Angle Compared to Steady State = 0**
7) **Pitch Rate = 10 deg per sec**
8) **Change in Heading Angle = 6 deg**
9) Time of Maneuver = 2.5 sec

III. ***Change in Bank Angle Maneuver***

1) Effective Flight Path Angle = -0.5 deg
2) Load Factor = 1.4 to 1.0, linearly
3) Segment Velocity = 80 knots
4) **Change in Roll Angle Compared to Steady State = 45 deg to 0 deg, linearly**
5) **Roll Rate = -15 deg per sec**
6) **Change in Pitch Angle Compared to Steady State = 0 deg**
7) **Pitch Rate = 0 deg per sec**
8) **Change in Heading Angle = 18 deg**

9) Time of Maneuver = 3 sec

30. Decrease Flight Path Angle by 1.6 deg (T10)

1) Effective Flight Path Angle = -0.5 deg - 0.8 deg
2) Load Factor = 0.87
3) Segment Velocity = 80 knots
4) **Change in Roll Angle Compared to Steady State = 0 deg**
5) **Roll Rate = 0**
6) **Change in Pitch Angle Compared to Steady State = 0 deg**
7) **Pitch Rate = 0 deg per sec**
8) Time of Maneuver = 0.5 sec
9) Final Flight Path Angle = -2.1deg

31. Constant Speed at 80 knots (S11)

1) Effective Flight Path Angle = -2 deg
2) Load factor = 1.0
3) Velocity = 80 knots
4) **Change in Roll Angle Compared to Steady State = 0**
5) **Roll Rate = 0**
6) **Change in Pitch Angle Compared to Steady State = 0**
7) **Pitch Rate = 0**
8) Time of Segment = 45 sec

32. Change heading by 13 deg to the left (T11)

I. ***Change in Bank Angle Maneuver***

1) Effective Flight Path Angle = -2.0 deg
2) Load Factor = 1.0 to 1.3, linearly
3) Segment Velocity = 80 knots
4) **Change in Roll Angle Compared to Steady State = 0 deg to 30 deg, linearly**
5) **Roll Rate = 15 deg per sec**

6) **Change in Pitch Angle Compared to Steady State = 0 deg**
7) **Pitch Rate = 0 deg per sec**
8) **Change in Heading = 6.5 deg**
9) Time of Maneuver = 2.0 sec

II. ***Change in Bank Angle Maneuver***

1) Effective Flight Path Angle = -2.0 deg
2) Load Factor = 1.3 to 1.0, linearly
3) Segment Velocity = 80 knots
4) **Change in Roll Angle Compared to Steady State = 30 deg to 0 deg, linearly**
5) **Roll Rate = -15 deg per sec**
6) **Change in Pitch Angle Compared to Steady State = 0 deg**
7) **Pitch Rate = 0 deg per sec**
8) **Change in Heading = 6.5 deg**
9) Time of Maneuver = 2.0 sec

33. Increase Flight Path Angle by 5.6 deg (T11)

1) Effective Flight Path Angle = -2.0 deg + 2.8 deg
2) Load Factor = 1.4
3) Segment Velocity = 80 knots
4) **Change in Roll Angle Compared to Steady State = 0 deg**
5) **Roll Rate = 0**
6) **Change in Pitch Angle Compared to Steady State = 0 deg**
7) **Pitch Rate = 0 deg per sec**
8) Time of Maneuver = 1.0 sec
9) Final Flight Path Angle = 3.5 deg

34. Accelerate from 80 to 120 knots at 0.1 g (S12)

I. ***Change in Acceleration Maneuver***

1) Effective Flight Path Angle = 3.5 deg + 3 deg
2) Load Factor = 1.0

3) Segment Velocity = 80 knots

4) Change in Acceleration over Maneuver = 0.1 g

5) Change in Roll Angle Compared to Steady State = 0

6) Roll Rate = 0

7) Change in Pitch Angle Compared to Steady State = -3 deg

8) Pitch Rate = -12 deg per sec

9) Time of Maneuver = 0.5 sec

II. ***Constant Acceleration Maneuver***

1) Effective Flight Path Angle = 3.5 deg + 6 deg

2) Load Factor = 1.0

3) Initial Velocity = 80 knots, Final Velocity = 120 knots

4) Acceleration = 0.1 g

5) Change in Roll Angle Compared to Steady State = 0

6) Roll Rate = 0

7) Change in Pitch Angle Compared to Steady State = 6 deg

8) Pitch Rate = 0

9) Time of Maneuver = 21.0 sec

III. ***Change in Acceleration Maneuver***

1) Effective Flight Path Angle = 3.5 deg + 3 deg

2) Load Factor = 1.0

3) Segment Velocity = 120 knots

4) Change in Acceleration over Maneuver = -0.1 g

5) Change in Roll Angle Compared to Steady State = 0

6) Roll Rate = 0

7) Change in Pitch Angle Compared to Steady State = 3 deg

8) Pitch Rate = +12 deg per sec

9) Time of Maneuver = 0.5 sec

35. Constant Speed at 120 knots (S12)

1) Effective Flight Path Angle = 3.5 deg

2) Load factor = 1.0

3) Velocity = 120 knots

4) Change in Roll Angle Compared to Steady State = 0

5) Roll Rate = 0

6) Change in Pitch Angle Compared to Steady State = 0

7) Pitch Rate = 0

8) Time of Segment = 47.5 sec

36. Change heading by 7 deg to the right (T12)

I. ***Change in Bank Angle Maneuver***

1) Effective Flight Path Angle = 3.5 deg

2) Load Factor = 1.0 to 1.23, linearly

3) Segment Velocity = 120 knots

4) Change in Roll Angle Compared to Steady State = 0 deg to 25 deg, linearly

5) Roll Rate = 15 deg per sec

6) Change in Pitch Angle Compared to Steady State = 0 deg

7) Pitch Rate = 0 deg per sec

8) Change in Heading = 3.5 deg

9) Time of Maneuver = 1.75 sec

II. ***Change in Bank Angle Maneuver***

1) Effective Flight Path Angle = 3.5 deg

2) Load Factor = 1.23 to 1.0, linearly

3) Segment Velocity = 120 knots

4) Change in Roll Angle Compared to Steady State = 25 deg to 0 deg, linearly

5) Roll Rate = -15 deg per sec

6) Change in Pitch Angle Compared to Steady State = 0 deg

7) Pitch Rate = 0 deg per sec

8) Change in Heading = 3.5 deg

9) Time of Maneuver = 1.75 sec

37. Decrease Flight Path Angle by 10.6 deg (T12)

1) Effective Flight Path Angle = 3.5 deg - 5.3 deg
2) Load Factor = 0.6
3) Segment Velocity = 120 knots
4) **Change in Roll Angle Compared to Steady State = 0 deg**
5) **Roll Rate = 0**
6) **Change in Pitch Angle Compared to Steady State = 0 deg**
7) **Pitch Rate = 0 deg per sec**
8) Time of Maneuver = 3 sec
9) Final Flight Path Angle = -7.1 deg

38. Decelerate from 120 to 91 knots at 0.1 g (S13)

I. ***Change in Acceleration Maneuver***

1) Effective Flight Path Angle = -7.1 deg - 3 deg
2) Load Factor = 1.0
3) Segment Velocity = 120 knots
4) Change in Acceleration over Maneuver = 0.1 g
5) **Change in Roll Angle Compared to Steady State = 0**
6) **Roll Rate = 0**
7) **Change in Pitch Angle Compared to Steady State = -3 deg**
8) **Pitch Rate = 12 deg per sec**
9) Time of Maneuver = 0.5 sec

II. ***Constant Acceleration Maneuver***

1) Effective Flight Path Angle = -7.1 deg - 6 deg
2) Load Factor = 1.0
3) Initial Velocity = 120 knots, Final Velocity = 91 knots
4) Deceleration = 0.1 g
5) **Change in Roll Angle Compared to Steady State = 0**
6) **Roll Rate = 0**
7) **Change in Pitch Angle Compared to Steady State = 6 deg**
8) **Pitch Rate = 0**
9) Time of Maneuver =15.0 sec

III. ***Change in Acceleration Maneuver***

1) Effective Flight Path Angle = -7.1 deg - 3 deg
2) Load Factor = 1.0
3) Segment Velocity = 91 knots
4) Change in Acceleration over Maneuver = -0.1 g
5) **Change in Roll Angle Compared to Steady State = 0**
6) **Roll Rate = 0**
7) **Change in Pitch Angle Compared to Steady State = 3 deg**
8) **Pitch Rate = -12 deg per sec**
9) Time of Maneuver = 0.5 sec

39. Constant Speed at 91 knots (S13)

1) Effective Flight Path Angle = -7.1 deg
2) Load factor = 1.0
3) Velocity = 91 knots
4) **Change in Roll Angle Compared to Steady State = 0**
5) **Roll Rate = 0**
6) **Change in Pitch Angle Compared to Steady State = 0**
7) **Pitch Rate = 0**
8) Time of Segment = 24 sec

40. Change heading by 119 deg to the right (T13)

I. ***Change in Bank Angle Maneuver***

1) Effective Flight Path Angle = -7.1 deg
2) Load Factor = 1.0 to 1.4, linearly
3) Segment Velocity = 91 knots
4) **Change in Roll Angle Compared to Steady State = 0 deg to 45 deg, linearly**
5) **Roll Rate = 15 deg per sec**
6) **Change in Pitch Angle Compared to Steady State = 0 deg**
7) **Pitch Rate = 0 deg per sec**

8) **Change in Heading Angle = 16 deg**

9) Time of Maneuver = 3 sec

II. ***Constant Bank Angle Maneuver***

1) Effective Flight Path Angle = -7.1 deg
2) Load Factor = 1.4
3) Segment Velocity = 91 knots
4) **Change in Roll Angle Compared to Steady State = 45 deg**
5) **Roll Rate = 0**
6) **Change in Pitch Angle Compared to Steady State = 0**
7) **Pitch Rate = 10 deg per sec**
8) **Change in Heading Angle = 87 deg**
9) Time of Maneuver =7.5 sec

III. ***Change in Bank Angle Maneuver***

1) Effective Flight Path Angle = -7.1 deg
2) Load Factor = 1.4 to 1.0, linearly
3) Segment Velocity = 91 knots
4) **Change in Roll Angle Compared to Steady State = 45 deg to 0 deg, linearly**
5) **Roll Rate = -15 deg per sec**
6) **Change in Pitch Angle Compared to Steady State = 0 deg**
7) **Pitch Rate = 0 deg per sec**
8) **Change in Heading Angle = 16 deg**
9) Time of Maneuver = 3 sec

41. Increase Flight Path Angle by 7.5 deg (T13)

1) Effective Flight Path Angle = -7.5 deg + 3.75 deg
2) Load Factor = 1.3
3) Segment Velocity = 91 knots
4) **Change in Roll Angle Compared to Steady State = 0 deg**
5) **Roll Rate = 0**
6) **Change in Pitch Angle Compared to Steady State = 0 deg**

7) **Pitch Rate = 0 deg per sec**
8) Time of Maneuver = 2 sec
9) Final Flight Path angle = 0.4 deg

42. Decelerate from 91 to 80 knots at 0.1 g (S14)

I. ***Change in Acceleration Maneuver***

1) Effective Flight Path Angle = 0.4 deg - 3 deg
2) Load Factor = 1.0
3) Segment Velocity = 91 knots
4) Change in Acceleration over Maneuver = 0.1 g
5) **Change in Roll Angle Compared to Steady State = 0**
6) **Roll Rate = 0**
7) **Change in Pitch Angle Compared to Steady State = -3 deg**
8) **Pitch Rate = 12 deg per sec**
9) Time of Maneuver = 0.5 sec

II. ***Constant Acceleration Maneuver***

1) Effective Flight Path Angle = 0.4 deg - 6 deg
2) Load Factor = 1.0
3) Initial Velocity = 91 knots, Final Velocity = 80 knots
4) Deceleration = 0.1 g
5) **Change in Roll Angle Compared to Steady State = 0**
6) **Roll Rate = 0**
7) **Change in Pitch Angle Compared to Steady State = 6 deg**
8) **Pitch Rate = 0**
9) Time of Maneuver = 5.0 sec

III. ***Change in Acceleration Maneuver***

1) Effective Flight Path Angle = 0.4 deg - 3 deg
2) Load Factor = 1.0
3) Segment Velocity = 80 knots
4) Change in Acceleration over Maneuver = -0.1 g
5) **Change in Roll Angle Compared to Steady State = 0**

6) **Roll Rate = 0**

7) **Change in Pitch Angle Compared to Steady State = 3 deg**

8) **Pitch Rate = -12 deg per sec**

9) Time of Maneuver = 0.5 sec

43. Constant Speed at 80 knots (S14)

1) Effective Flight Path Angle = 0.4 deg

2) Load factor = 1.0

3) Velocity = 80 knots

4) **Change in Roll Angle Compared to Steady State = 0**

5) **Roll Rate = 0**

6) **Change in Pitch Angle Compared to Steady State = 0**

7) **Pitch Rate = 0**

8) Time of Segment = 1226.5 sec

44. Change heading by 30 deg to the right (T14)

I. ***Change in Bank Angle Maneuver***

1) Effective Flight Path Angle = 0.4 deg

2) Load Factor = 1.0 to 1.4, linearly

3) Segment Velocity = 80 knots

4) **Change in Roll Angle Compared to Steady State = 0 deg to 45 deg, linearly**

5) **Roll Rate = 15 deg per sec**

6) **Change in Pitch Angle Compared to Steady State = 0 deg**

7) **Pitch Rate = 0 deg per sec**

8) **Change in Heading = 15 deg**

9) Time of Maneuver = 2.75 sec

II. ***Change in Bank Angle Maneuver***

1) Effective Flight Path Angle = 0.4 deg

2) Load Factor = 1.4 to 1.0, linearly

3) Segment Velocity = 80 knots

4) **Change in Roll Angle Compared to Steady State = 45 deg to 0 deg, linearly**
5) **Roll Rate = -15 deg per sec**
6) **Change in Pitch Angle Compared to Steady State = 0 deg**
7) **Pitch Rate = 0 deg per sec**
8) **Change in Heading = 15 deg**
9) Time of Maneuver = 2.75 sec

45. Decrease Flight Path Angle by 7.1 deg (T14)

1) Effective Flight Path Angle = 0.4 deg - 3.6 deg
2) Load Factor = 0.65
3) Segment Velocity = 80 knots
4) **Change in Roll Angle Compared to Steady State = 0 deg**
5) **Roll Rate = 0**
6) **Change in Pitch Angle Compared to Steady State = 0 deg**
7) **Pitch Rate = 0 deg per sec**
8) Time of Maneuver = 1.5 sec
9) Final Flight Path angle = 6.7 deg

46. Constant Speed at 80 knots (S15)

1) Effective Flight Path Angle = 6.7 deg
2) Load factor = 1.0
3) Velocity = 80 knots
4) **Change in Roll Angle Compared to Steady State = 0**
5) **Roll Rate = 0**
6) **Change in Pitch Angle Compared to Steady State = 0**
7) **Pitch Rate = 0**
8) Time of Segment = 60.5 sec

48. Constant Speed at 80 knots (S16)

1) Effective Flight Path Angle = -0.4 deg
2) Load factor = 1.0
3) Velocity = 80 knots
4) **Change in Roll Angle Compared to Steady State = 0**
5) **Roll Rate = 0**
6) **Change in Pitch Angle Compared to Steady State = 0**
7) **Pitch Rate = 0**
8) Time of Segment =119 sec

49. Change heading by 18 deg to the left (T16)

I. ***Change in Bank Angle Maneuver***

1) Effective Flight Path Angle = -0.4 deg
2) Load Factor = 1.0 to 1.3, linearly
3) Segment Velocity = 80 knots
4) **Change in Roll Angle Compared to Steady State = 0 deg to 34 deg, linearly**
5) **Roll Rate = 15 deg per sec**
6) **Change in Pitch Angle Compared to Steady State = 0 deg**
7) **Pitch Rate = 0 deg per sec**
8) **Change in Heading = 9 deg**
9) Time of Maneuver = 2.25 sec

II. ***Change in Bank Angle Maneuver***

1) Effective Flight Path Angle = -0.4 deg
2) Load Factor = 1.3 to 1.0, linearly
3) Segment Velocity = 80 knots
4) **Change in Roll Angle Compared to Steady State = 34 deg to 0 deg, linearly**
5) **Roll Rate = -15 deg per sec**
6) **Change in Pitch Angle Compared to Steady State = 0 deg**
7) **Pitch Rate = 0 deg per sec**
8) **Change in Heading = 9 deg**

9) Time of Maneuver = 2.25 sec

50. Decrease Flight Path Angle by 5.4 deg (T16)

1) Effective Flight Path Angle = -0.4 deg - 2.7 deg
2) Load Factor = 0.6
3) Segment Velocity = 80 knots
4) **Change in Roll Angle Compared to Steady State = 0 deg**
5) **Roll Rate = 0**
6) **Change in Pitch Angle Compared to Steady State = 0 deg**
7) **Pitch Rate = 0 deg per sec**
8) Time of Maneuver = 1 sec
9) Final flight Path angle = -5.8 deg

51. Constant Speed at 80 knots (S17)

1) Effective Flight Path Angle = -5.8 deg
2) Load factor = 1.0
3) Velocity = 80 knots
4) **Change in Roll Angle Compared to Steady State = 0**
5) **Roll Rate = 0**
6) **Change in Pitch Angle Compared to Steady State = 0**
7) **Pitch Rate = 0**
8) Time of Segment = 30 sec

Appendix C

RNM Input File with QSAM-PRIME Sphere Specification

This appendix presents a sample input file generated by the QSAM-PRIME code. This file is then used as input in RNM in conjunction with the new spheres developed by QSAM-PRIME. The columns in the input file sown below are: **X** (the ground based X coordinate), **Y** (the ground based Y coordinate in feet), **Z** (the ground based Z coordinate, in feet), **TA** (turn angle, *this utility is not tested and is currently not used*), **TR** (turn radius, *this utility is not tested and is currently not used*), **V** (flight velocity in knots), **HEAD** (heading angle in degrees), **AOA** (angle of attack in degrees), **PHI** (roll angle in degrees), **NAC** (nacelle angle in degrees) and **FILE** (.nc file name).

X	Y	Z	TA	TR	V	HEAD	AOA	PHI	NAC	FILE
1703072.0	12547651.0	139.0	0.0	0.0	50.0	100.4	-7.3	0.0	90.0	MP902001.nc
1703155.0	12547635.8	140.9	0.0	0.0	50.0	100.4	-7.3	0.0	90.0	MP902002.nc
1703239.6	12547620.3	142.8	0.0	0.0	51.9	100.4	-13.0	0.0	90.0	MP902003.nc
1703327.3	12547604.3	144.7	0.0	0.0	53.8	100.4	-13.0	0.0	90.0	MP902004.nc
1703418.2	12547587.6	146.8	0.0	0.0	55.7	100.4	-13.0	0.0	90.0	MP902005.nc
1703512.3	12547570.4	148.9	0.0	0.0	57.6	100.4	-13.0	0.0	90.0	MP902006.nc
1703609.5	12547552.6	151.0	0.0	0.0	59.5	100.4	-13.0	0.0	90.0	MP902007.nc
1703709.9	12547534.2	153.3	0.0	0.0	61.4	100.4	-13.1	0.0	90.0	MP902008.nc
1703813.5	12547515.3	155.6	0.0	0.0	63.4	100.4	-13.2	0.0	90.0	MP902009.nc
1703920.3	12547495.8	158.0	0.0	0.0	65.3	100.4	-13.3	0.0	90.0	MP902010.nc
1704030.2	12547475.6	160.5	0.0	0.0	67.2	100.4	-13.4	0.0	90.0	MP902011.nc
1704143.2	12547454.9	163.0	0.0	0.0	69.1	100.4	-13.4	0.0	90.0	MP902012.nc
1704259.5	12547433.7	165.6	0.0	0.0	71.0	100.4	-13.5	0.0	90.0	MP902013.nc
1704378.9	12547411.8	168.3	0.0	0.0	72.9	100.4	-13.6	0.0	90.0	MP902014.nc
1704501.5	12547389.4	171.0	0.0	0.0	74.8	100.4	-13.7	0.0	90.0	MP902015.nc
1704627.2	12547366.4	173.9	0.0	0.0	76.7	100.4	-13.8	0.0	90.0	MP902016.nc
1704756.1	12547342.8	176.7	0.0	0.0	78.6	100.4	-13.9	0.0	90.0	MP902017.nc
1704888.2	12547318.6	179.7	0.0	0.0	80.5	100.4	-14.0	0.0	90.0	MP902018.nc
1705023.4	12547293.9	182.7	0.0	0.0	82.4	100.4	-14.2	0.0	90.0	MP902019.nc
1705161.8	12547268.5	185.8	0.0	0.0	84.3	100.4	-14.4	0.0	90.0	MP902020.nc
1705303.4	12547242.6	189.0	0.0	0.0	86.2	100.4	-14.6	0.0	90.0	MP902021.nc

X	Y	Z	TA	TR	V	HEAD	AOA	PHI	NAC	FILE
1705448.1	12547216.1	192.3	0.0	0.0	88.2	100.4	-14.8	0.0	90.0	MP902022.nc
1705596.1	12547189.1	195.6	0.0	0.0	90.1	100.4	-15.0	0.0	90.0	MP902023.nc
1705747.1	12547161.4	199.0	0.0	0.0	92.0	100.4	-15.2	0.0	90.0	MP902024.nc
1705901.4	12547133.2	202.4	0.0	0.0	93.9	100.4	-15.4	0.0	90.0	MP902025.nc
1706058.8	12547104.4	205.9	0.0	0.0	95.8	100.4	-15.6	0.0	90.0	MP902026.nc
1706219.3	12547075.0	209.5	0.0	0.0	97.7	100.4	-15.8	0.0	90.0	MP902027.nc
1706383.1	12547045.0	213.2	0.0	0.0	99.6	100.4	-16.0	0.0	90.0	MP902028.nc
1706550.0	12547014.5	216.9	0.0	0.0	101.5	100.4	-16.1	0.0	90.0	MP902029.nc
1706720.1	12546983.3	220.8	0.0	0.0	103.4	100.4	-16.2	0.0	90.0	MP902030.nc
1706893.3	12546951.6	224.6	0.0	0.0	105.3	100.4	-16.3	0.0	90.0	MP902031.nc
1707069.7	12546919.3	228.6	0.0	0.0	107.2	100.4	-16.4	0.0	90.0	MP902032.nc
1707249.3	12546886.5	232.6	0.0	0.0	109.1	100.4	-16.4	0.0	90.0	MP902033.nc
1707432.0	12546853.0	236.7	0.0	0.0	111.0	100.4	-16.5	0.0	90.0	MP902034.nc
1707617.9	12546819.0	240.9	0.0	0.0	113.0	100.4	-16.6	0.0	90.0	MP902035.nc
1707807.0	12546784.4	245.1	0.0	0.0	114.9	100.4	-16.7	0.0	90.0	MP902036.nc
1707999.3	12546749.2	249.4	0.0	0.0	116.8	100.4	-16.8	0.0	90.0	MP902037.nc
1708194.7	12546713.5	253.8	0.0	0.0	118.7	100.4	-16.9	0.0	90.0	MP902038.nc
1708592.4	12546640.7	262.7	0.0	0.0	120.0	100.4	-11.3	0.0	90.0	MP902039.nc
1794089.7	12530993.2	2178.9	0.0	0.0	120.0	100.4	-11.3	0.0	90.0	MP902040.nc
1794291.0	12530972.6	2182.3	0.0	0.0	120.0	95.8	-11.3	22.5	90.0	MP902041.nc
1794493.0	12530983.9	2186.7	0.0	0.0	120.0	86.8	-11.3	45.0	90.0	MP902042.nc
1794690.7	12531026.9	2191.2	0.0	0.0	120.0	77.7	-11.3	45.0	90.0	MP902043.nc
1794879.2	12531100.5	2195.6	0.0	0.0	120.0	68.7	-11.3	45.0	90.0	MP902044.nc
1795053.7	12531202.8	2200.1	0.0	0.0	120.0	59.6	-11.3	45.0	90.0	MP902045.nc
1795210.0	12531331.4	2204.6	0.0	0.0	120.0	50.6	-11.3	22.5	90.0	MP902046.nc
1795358.4	12531468.3	2220.9	0.0	0.0	120.0	47.3	-14.6	0.0	90.0	MP902047.nc
1814526.2	12549150.5	4377.1	0.0	0.0	120.0	47.3	-14.6	0.0	90.0	MP902048.nc
1814685.3	12549275.4	4348.0	0.0	0.0	120.0	51.9	-14.6	-22.5	90.0	MP902049.nc
1814862.3	12549373.6	4364.3	0.0	0.0	120.0	61.0	-14.6	-45.0	90.0	MP902050.nc
1815052.5	12549442.5	4380.7	0.0	0.0	120.0	70.1	-14.6	-45.0	90.0	MP902051.nc
1815251.2	12549480.4	4397.1	0.0	0.0	120.0	79.2	-14.6	-22.5	90.0	MP902052.nc
1815449.6	12549520.6	4390.8	0.0	0.0	120.0	78.6	-8.2	0.0	90.0	MP902053.nc
1838079.7	12554106.6	3676.4	0.0	0.0	120.0	78.6	-8.2	0.0	90.0	MP902054.nc
1838280.6	12554131.0	3676.1	0.0	0.0	120.0	83.1	-8.2	-22.5	90.0	MP902055.nc
1838482.8	12554123.4	3669.9	0.0	0.0	120.0	92.1	-8.2	-45.0	90.0	MP902056.nc
1838681.2	12554084.0	3663.6	0.0	0.0	120.0	101.2	-8.2	-45.0	90.0	MP902057.nc
1838871.0	12554013.9	3657.4	0.0	0.0	120.0	110.3	-8.2	-45.0	90.0	MP902058.nc
1839047.4	12553914.8	3651.2	0.0	0.0	120.0	119.3	-8.2	-45.0	90.0	MP902059.nc
1839206.0	12553789.2	3645.0	0.0	0.0	120.0	128.4	-8.2	-22.5	90.0	MP902060.nc
1839369.3	12553669.3	3643.5	0.0	0.0	120.0	126.3	-9.6	0.0	90.0	MP902061.nc
1893711.7	12513788.6	3164.3	0.0	0.0	120.0	126.3	-9.6	0.0	90.0	MP902062.nc
1893883.7	12513682.1	3155.2	0.0	0.0	120.0	121.8	-9.6	22.5	90.0	MP902063.nc
1894070.4	12513604.0	3153.8	0.0	0.0	120.0	112.7	-9.6	45.0	90.0	MP902064.nc
1894267.0	12513556.3	3152.3	0.0	0.0	120.0	103.6	-9.6	45.0	90.0	MP902065.nc
1894468.7	12513540.1	3150.8	0.0	0.0	120.0	94.6	-9.6	45.0	90.0	MP902066.nc
1894670.4	12513555.8	3149.4	0.0	0.0	120.0	85.5	-9.6	45.0	90.0	MP902067.nc
1894867.1	12513603.1	3147.9	0.0	0.0	120.0	76.5	-9.6	22.5	90.0	MP902068.nc
1895063.8	12513650.6	3156.4	0.0	0.0	120.0	76.4	-12.4	0.0	90.0	MP902069.nc
1947420.8	12526293.3	5466.4	0.0	0.0	120.0	76.4	-12.4	0.0	90.0	MP902070.nc
1947620.6	12526325.1	5432.0	0.0	0.0	120.0	81.0	-12.4	-22.5	90.0	MP902071.nc
1947822.9	12526325.1	5440.6	0.0	0.0	120.0	90.0	-12.4	-45.0	90.0	MP902072.nc
1948022.7	12526293.1	5449.1	0.0	0.0	120.0	99.1	-12.4	-22.5	90.0	MP902073.nc
1948223.9	12526269.5	5450.1	0.0	0.0	120.0	96.7	-10.3	0.0	90.0	MP902074.nc
2091048.4	12509551.8	6176.2	0.0	0.0	120.0	96.7	-10.3	0.0	90.0	MP902075.nc

X	Y	Z	TA	TR	V	HEAD	AOA	PHI	NAC	FILE
2091239.2	12509484.0	6175.9	0.0	0.0	120.0	109.6	-9.9	0.0	90.0	MP902076.nc
2209599.0	12467489.5	6041.3	0.0	0.0	120.0	109.6	-9.9	0.0	90.0	MP902077.nc
2209783.7	12467407.0	6011.0	0.0	0.0	120.0	114.1	-9.9	-22.5	90.0	MP902078.nc
2209953.1	12467296.4	6010.7	0.0	0.0	120.0	123.1	-9.9	-45.0	90.0	MP902079.nc
2210103.0	12467160.5	6010.4	0.0	0.0	120.0	132.2	-9.9	-22.5	90.0	MP902080.nc
2210259.9	12467033.4	5993.9	0.0	0.0	120.0	129.0	-5.3	0.0	90.0	MP902081.nc
2210415.5	12466907.4	5977.5	0.0	0.0	118.1	129.0	0.5	0.0	90.0	MP902082.nc
2210568.6	12466783.4	5961.3	0.0	0.0	116.2	129.0	0.6	0.0	90.0	MP902083.nc
2210719.2	12466661.4	5945.4	0.0	0.0	114.3	129.0	0.7	0.0	90.0	MP902084.nc
2210867.4	12466541.4	5929.8	0.0	0.0	112.4	129.0	0.8	0.0	90.0	MP902085.nc
2211013.0	12466423.4	5914.4	0.0	0.0	110.5	129.0	0.9	0.0	90.0	MP902086.nc
2211156.2	12466307.5	5899.3	0.0	0.0	108.6	129.0	1.0	0.0	90.0	MP902087.nc
2211296.8	12466193.6	5884.5	0.0	0.0	106.6	129.0	1.1	0.0	90.0	MP902088.nc
2211435.0	12466081.6	5869.9	0.0	0.0	104.7	129.0	1.2	0.0	90.0	MP902089.nc
2211570.6	12465971.8	5855.6	0.0	0.0	102.8	129.0	1.3	0.0	90.0	MP902090.nc
2211703.8	12465863.9	5841.5	0.0	0.0	100.9	129.0	1.4	0.0	90.0	MP902091.nc
2211834.5	12465758.1	5827.7	0.0	0.0	99.0	129.0	1.5	0.0	90.0	MP902092.nc
2211962.6	12465654.2	5814.2	0.0	0.0	97.1	129.0	1.7	0.0	90.0	MP902093.nc
2212088.3	12465552.4	5801.0	0.0	0.0	95.2	129.0	1.9	0.0	90.0	MP902094.nc
2212211.5	12465452.6	5788.0	0.0	0.0	93.3	129.0	2.1	0.0	90.0	MP902095.nc
2212332.2	12465354.9	5775.2	0.0	0.0	91.4	129.0	2.3	0.0	90.0	MP902096.nc
2212450.4	12465259.1	5762.7	0.0	0.0	89.5	129.0	2.5	0.0	90.0	MP902097.nc
2212566.1	12465165.4	5750.5	0.0	0.0	87.6	129.0	2.7	0.0	90.0	MP902098.nc
2212679.4	12465073.7	5738.6	0.0	0.0	85.7	129.0	2.9	0.0	90.0	MP902099.nc
2212790.1	12464984.0	5726.9	0.0	0.0	83.8	129.0	3.0	0.0	90.0	MP902100.nc
2212898.3	12464896.4	5715.5	0.0	0.0	81.8	129.0	3.2	0.0	90.0	MP902101.nc
2213109.9	12464724.9	5693.2	0.0	0.0	81.0	129.0	-2.4	0.0	90.0	MP902102.nc
2256097.1	12429905.8	1157.1	0.0	0.0	81.0	129.0	-2.4	0.0	90.0	MP902103.nc
2256184.6	12429801.2	1148.3	0.0	0.0	81.0	140.1	-3.4	0.0	90.0	MP902104.nc
2256357.6	12429594.4	1130.9	0.0	0.0	80.0	140.1	-3.3	0.0	90.0	MP902105.nc
2260853.5	12424220.3	679.1	0.0	0.0	80.0	140.1	-3.3	0.0	90.0	MP902106.nc
2260939.6	12424116.3	678.0	0.0	0.0	80.0	140.3	-6.5	0.0	90.0	MP902107.nc
2266942.6	12416934.4	588.8	0.0	0.0	80.0	140.3	-6.5	0.0	90.0	MP902108.nc
2267015.7	12416821.3	600.0	0.0	0.0	80.0	147.1	-6.5	-22.5	90.0	MP902109.nc
2267060.2	12416694.1	598.9	0.0	0.0	80.0	160.7	-6.5	-45.0	90.0	MP902110.nc
2267073.5	12416560.1	597.8	0.0	0.0	80.0	174.3	-6.5	-45.0	90.0	MP902111.nc
2267055.1	12416426.6	596.7	0.0	0.0	80.0	187.9	-6.5	-22.5	90.0	MP902112.nc
2267049.0	12416291.8	591.9	0.0	0.0	80.0	182.6	-5.0	0.0	90.0	MP902113.nc
2266805.1	12410899.8	398.8	0.0	0.0	80.0	182.6	-5.0	0.0	90.0	MP902114.nc
2266830.0	12410767.4	407.1	0.0	0.0	80.0	169.4	-10.5	0.0	90.0	MP902115.nc
2266855.1	12410633.3	415.5	0.0	0.0	81.9	169.4	-16.5	0.0	90.0	MP902116.nc
2266880.8	12410496.1	424.1	0.0	0.0	83.8	169.4	-16.6	0.0	90.0	MP902117.nc
2266907.1	12410355.8	432.9	0.0	0.0	85.7	169.4	-16.8	0.0	90.0	MP902118.nc
2266934.0	12410212.2	442.0	0.0	0.0	87.6	169.4	-17.0	0.0	90.0	MP902119.nc
2266961.5	12410065.6	451.2	0.0	0.0	89.5	169.4	-17.2	0.0	90.0	MP902120.nc
2266989.6	12409915.7	460.6	0.0	0.0	91.4	169.4	-17.4	0.0	90.0	MP902121.nc
2267018.3	12409762.7	470.2	0.0	0.0	93.4	169.4	-17.6	0.0	90.0	MP902122.nc
2267047.6	12409606.6	480.0	0.0	0.0	95.3	169.4	-17.8	0.0	90.0	MP902123.nc
2267077.5	12409447.3	490.0	0.0	0.0	97.2	169.4	-18.0	0.0	90.0	MP902124.nc
2267107.9	12409284.8	500.2	0.0	0.0	99.1	169.4	-18.2	0.0	90.0	MP902125.nc
2267139.0	12409119.2	510.7	0.0	0.0	101.0	169.4	-18.3	0.0	90.0	MP902126.nc
2267170.6	12408950.4	521.3	0.0	0.0	102.9	169.4	-18.4	0.0	90.0	MP902127.nc
2267202.9	12408778.5	532.1	0.0	0.0	104.8	169.4	-18.5	0.0	90.0	MP902128.nc
2267235.7	12408603.4	543.1	0.0	0.0	106.7	169.4	-18.6	0.0	90.0	MP902129.nc

X	Y	Z	TA	TR	V	HEAD	AOA	PHI	NAC	FILE
2267269.1	12408425.1	554.3	0.0	0.0	108.6	169.4	-18.7	0.0	90.0	MP902130.nc
2267303.1	12408243.7	565.7	0.0	0.0	110.5	169.4	-18.8	0.0	90.0	MP902131.nc
2267337.7	12408059.1	577.3	0.0	0.0	112.4	169.4	-18.9	0.0	90.0	MP902132.nc
2267372.9	12407871.3	589.1	0.0	0.0	114.3	169.4	-19.0	0.0	90.0	MP902133.nc
2267408.7	12407680.4	601.1	0.0	0.0	116.2	169.4	-19.1	0.0	90.0	MP902134.nc
2267445.1	12407486.4	613.3	0.0	0.0	118.2	169.4	-19.2	0.0	90.0	MP902135.nc
2267519.3	12407090.5	638.1	0.0	0.0	120.0	169.4	-13.5	0.0	90.0	MP902136.nc
2268972.1	12399341.6	1125.1	0.0	0.0	120.0	169.4	-13.5	0.0	90.0	MP902137.nc
2268984.8	12399141.0	1100.0	0.0	0.0	120.0	176.4	-2.9	0.0	90.0	MP902138.nc
2268997.5	12398942.0	1075.1	0.0	0.0	118.1	176.4	2.9	0.0	90.0	MP902139.nc
2269009.9	12398746.2	1050.7	0.0	0.0	116.2	176.4	3.0	0.0	90.0	MP902140.nc
2269022.1	12398553.6	1026.6	0.0	0.0	114.3	176.4	3.1	0.0	90.0	MP902141.nc
2269034.1	12398364.2	1002.9	0.0	0.0	112.4	176.4	3.2	0.0	90.0	MP902142.nc
2269045.9	12398178.0	979.6	0.0	0.0	110.5	176.4	3.3	0.0	90.0	MP902143.nc
2269057.5	12397994.9	956.7	0.0	0.0	108.6	176.4	3.4	0.0	90.0	MP902144.nc
2269068.9	12397815.1	934.3	0.0	0.0	106.6	176.4	3.5	0.0	90.0	MP902145.nc
2269080.1	12397638.4	912.2	0.0	0.0	104.7	176.4	3.6	0.0	90.0	MP902146.nc
2269091.1	12397465.0	890.5	0.0	0.0	102.8	176.4	3.7	0.0	90.0	MP902147.nc
2269101.9	12397294.7	869.2	0.0	0.0	100.9	176.4	3.8	0.0	90.0	MP902148.nc
2269112.5	12397127.6	848.3	0.0	0.0	99.0	176.4	3.9	0.0	90.0	MP902149.nc
2269122.9	12396963.7	827.8	0.0	0.0	97.1	176.4	4.1	0.0	90.0	MP902150.nc
2269133.1	12396803.0	807.7	0.0	0.0	95.2	176.4	4.3	0.0	90.0	MP902151.nc
2269143.1	12396645.4	788.0	0.0	0.0	93.3	176.4	4.5	0.0	90.0	MP902152.nc
2269152.9	12396491.1	768.7	0.0	0.0	91.4	176.4	4.7	0.0	90.0	MP902153.nc
2269172.1	12396187.8	730.8	0.0	0.0	91.0	176.4	-1.0	0.0	90.0	MP902154.nc
2269337.5	12393344.3	360.8	0.0	0.0	91.0	176.4	-1.0	0.0	90.0	MP902155.nc
2269331.0	12393191.1	369.5	0.0	0.0	91.0	182.4	-1.0	-22.5	90.0	MP902156.nc
2269292.4	12393042.7	350.5	0.0	0.0	91.0	194.6	-1.0	-45.0	90.0	MP902157.nc
2269223.6	12392905.7	331.5	0.0	0.0	91.0	206.7	-1.0	-45.0	90.0	MP902158.nc
2269127.5	12392786.3	312.5	0.0	0.0	91.0	218.8	-1.0	-45.0	90.0	MP902159.nc
2269008.5	12392689.6	293.5	0.0	0.0	91.0	230.9	-1.0	-45.0	90.0	MP902160.nc
2268871.9	12392620.1	274.5	0.0	0.0	91.0	243.0	-1.0	-45.0	90.0	MP902161.nc
2268723.7	12392580.9	255.4	0.0	0.0	91.0	255.2	-1.0	-45.0	90.0	MP902162.nc
2268570.5	12392573.7	236.4	0.0	0.0	91.0	267.3	-1.0	-45.0	90.0	MP902163.nc
2268419.3	12392598.8	217.4	0.0	0.0	91.0	279.4	-1.0	-45.0	90.0	MP902164.nc
2268276.7	12392655.1	198.4	0.0	0.0	91.0	291.5	-1.0	-22.5	90.0	MP902165.nc
2268138.3	12392721.7	199.4	0.0	0.0	91.0	295.7	-8.5	0.0	90.0	MP902166.nc
2268001.4	12392787.6	200.4	0.0	0.0	89.1	295.7	-2.6	0.0	90.0	MP902167.nc
2267867.4	12392852.2	201.3	0.0	0.0	87.2	295.7	-2.4	0.0	90.0	MP902168.nc
2267736.2	12392915.3	202.3	0.0	0.0	85.3	295.7	-2.2	0.0	90.0	MP902169.nc
2267608.0	12392977.0	203.2	0.0	0.0	83.4	295.7	-2.0	0.0	90.0	MP902170.nc
2267482.7	12393037.4	204.1	0.0	0.0	81.5	295.7	-1.8	0.0	90.0	MP902171.nc
2267238.6	12393154.9	205.9	0.0	0.0	80.0	295.7	-7.4	0.0	90.0	MP902172.nc
2109309.3	12469202.9	1362.0	0.0	0.0	80.0	295.7	-7.4	0.0	90.0	MP902173.nc
2109195.7	12469275.3	1346.9	0.0	0.0	80.0	302.5	-7.4	-22.5	90.0	MP902174.nc
2109102.2	12469372.3	1347.8	0.0	0.0	80.0	316.1	-7.4	-45.0	90.0	MP902175.nc
2109034.2	12469488.6	1348.6	0.0	0.0	80.0	329.7	-7.4	-22.5	90.0	MP902176.nc
2108958.5	12469599.3	1332.8	0.0	0.0	80.0	325.7	-0.3	0.0	90.0	MP902177.nc
2104646.5	12475910.0	429.1	0.0	0.0	80.0	325.7	-0.3	0.0	90.0	MP902178.nc
2104570.2	12476021.3	428.1	0.0	0.0	80.0	325.6	-6.6	0.0	90.0	MP902179.nc
2095567.2	12489137.7	285.7	0.0	0.0	80.0	325.6	-6.6	0.0	90.0	MP902180.nc
2095478.5	12489239.0	310.0	0.0	0.0	80.0	318.8	-6.6	22.5	90.0	MP902181.nc
2095368.4	12489316.7	309.0	0.0	0.0	80.0	305.2	-6.6	22.5	90.0	MP902182.nc
2095262.3	12489399.1	295.4	0.0	0.0	80.0	307.8	-1.2	0.0	90.0	MP902183.nc

X	Y	Z	TA	TR	V	HEAD	AOA	PHI	NAC	FILE
2095157.5	12489480.5	281.9	0.0	0.0	78.1	307.8	4.6	0.0	90.0	MP902184.nc
2095055.2	12489560.0	268.8	0.0	0.0	76.2	307.8	4.7	0.0	90.0	MP902185.nc
2094955.4	12489637.4	256.0	0.0	0.0	74.3	307.8	4.8	0.0	90.0	MP902186.nc
2094858.2	12489713.0	243.5	0.0	0.0	72.4	307.8	4.9	0.0	90.0	MP902187.nc
2094763.5	12489786.5	231.3	0.0	0.0	70.5	307.8	5.0	0.0	90.0	MP902188.nc
2094671.3	12489858.1	219.5	0.0	0.0	68.6	307.8	5.1	0.0	90.0	MP902189.nc
2094581.7	12489927.8	208.0	0.0	0.0	66.6	307.8	5.2	0.0	90.0	MP902190.nc
2094494.5	12489995.4	196.8	0.0	0.0	64.7	307.8	5.3	0.0	90.0	MP902191.nc
2094410.0	12490061.1	185.9	0.0	0.0	62.8	307.8	5.4	0.0	90.0	MP902192.nc
2094327.9	12490124.9	175.4	0.0	0.0	60.9	307.8	5.5	0.0	90.0	MP902193.nc
2094248.4	12490186.6	165.2	0.0	0.0	59.0	307.8	5.5	0.0	90.0	MP902194.nc
2094171.4	12490246.4	155.3	0.0	0.0	57.1	307.8	5.5	0.0	90.0	MP902195.nc
2094096.9	12490304.3	145.7	0.0	0.0	55.2	307.8	5.5	0.0	90.0	MP902196.nc
2094025.0	12490360.2	136.5	0.0	0.0	53.3	307.8	5.5	0.0	90.0	MP902197.nc
2093955.6	12490414.1	127.6	0.0	0.0	51.4	307.8	5.5	0.0	90.0	MP902198.nc
2093888.7	12490466.0	119.0	0.0	0.0	49.5	307.8	5.5	0.0	90.0	MP902199.nc
2093824.3	12490516.0	110.7	0.0	0.0	47.6	307.8	5.5	0.0	90.0	MP902200.nc
2093762.5	12490564.0	102.8	0.0	0.0	45.7	307.8	5.5	0.0	90.0	MP902201.nc